Optimization of the Tempering Heat Treatment Cycle of Large Size Forgings

by

Sajad MIRZAEI

MANUSCRIPT-BASED THESIS PRESENTED TO ÉCOLE DE TECHNOLOGIE SUPÉRIEURE IN PARTIAL FULFILLEMENT FOR THE DEGREE OF DOCTOR OF PHILOSOPHY
Ph.D.

MONTREAL, SEPTEMBER 3, 2025

ÉCOLE DE TECHNOLOGIE SUPÉRIEURE
UNIVERSITÉ DU QUÉBEC

BOARD OF EXAMINERS

THIS THESIS HAS BEEN EVALUATED

BY THE FOLLOWING BOARD OF EXAMINERS

Mr. Mohammad Jahazi, Thesis Supervisor
Department of Mechanical Engineering at École de technologie supérieure

Mr. Farzad Bazdidi-Tehrani, Thesis Co-supervisor
School of Mechanical Engineering at Iran university of science and technology

Mr. Simon Joncas, President of the Board of Examiners
Department of Systems Engineering at École de technologie supérieure

Mr. Henri Champliaud, Member of the Jury
Department of Mechanical Engineering at École de technologie supérieure

Mr. Louis Gosselin, External Evaluator
Department of Mechanical Engineering at Université Laval

THIS THESIS WAS PRENSENTED AND DEFENDED

IN THE PRESENCE OF A BOARD OF EXAMINERS AND PUBLIC

ON AUGUST 27, 2025

AT ÉCOLE DE TECHNOLOGIE SUPÉRIEURE

ACKNOWLEDGMENT

I would like to express my deepest gratitude to my supervisor, Prof. Mohammad Jahazi, whose continuous support, insightful guidance, and expertise have been invaluable throughout my Ph.D. journey. His patience, encouragement, and constructive feedback have played a crucial role in shaping my research and academic growth. I am also sincerely grateful to my co-supervisor, Prof. Farzad Bazdidi-Tehrani from Iran University of Science and Technology (IUST), for his expertise, mentorship, and invaluable discussions on numerical simulations and computational approaches. His support extended beyond my time at IUST, and I truly appreciate his dedication to my academic development.

I would also like to acknowledge Nima Bohlooli Arkhazloo, a former Ph.D. student at ÉTS and currently a Senior Application Engineer at ANSYS, for his significant contributions and technical support during various phases of my research.

Special thanks go to our industrial partner, Sorel Forge (Finkl Steel), particularly the R & D, Metallurgy, and Engineering Departments, for their extensive support in facilitating large-scale experimental tests and providing critical data for my research. In particular, I am grateful to Jean-Benoit Morin, Dominique Tremblay, Luc Giguère, and Philippe Tremblay for their collaboration, technical assistance, and generous time investment in making this project a success.

I also extend my heartfelt appreciation to my colleagues and friends at CM2P, whose collaboration, insightful discussions, and encouragement have greatly enriched my doctoral experience. Their support has been invaluable, and I am grateful for the stimulating research environment they provided.

I would like to extend my sincere gratitude to the Digital Research Alliance of Canada for providing the high-performance computing resources that made my computationally intensive

simulations feasible. Their support in granting access to advanced computing clusters has been instrumental in accelerating the progress of this research.

Finally, my deepest and most heartfelt gratitude goes to my wife, mother, and father, whose unwavering love, sacrifices, and encouragement have been the foundation of my strength throughout this journey. Their endless support, patience, and belief in me have been my greatest motivation in times of challenge and doubt. To my wife, your love, understanding, and constant reassurance have made every hardship bearable, and I am forever grateful to have you by my side. To my mother and father, your boundless love and sacrifices have shaped the person I am today; this achievement is as much yours as it is mine. I dedicate this work to you with profound love and appreciation.

Optimisation du Cycle de Traitement Thermique de Revenue des Pièces Forgées de Grande Taille

Sajad MIIRZAEI

RÉSUMÉ

Le traitement thermique des grandes pièces forgées en acier joue un rôle essentiel dans l'obtention des propriétés mécaniques requises pour diverses applications industrielles, notamment dans les secteurs de l'aérospatiale, de l'automobile et des machines lourdes. Le revenu, une étape clé du traitement thermique, influence considérablement les performances des matériaux en modifiant leur microstructure afin d'améliorer leur résilience, leur dureté et leur résistance à l'usure. Cependant, garantir une répartition uniforme de la température au sein des fours industriels électriques de grande taille constitue un défi majeur en raison des interactions thermiques complexes, des gradients de température importants et des inefficacités énergétiques. Les approches empiriques traditionnelles visant à optimiser le processus de traitement thermique s'avèrent souvent insuffisantes, car elles ne prennent pas en compte l'interaction complexe entre la conception du four, les configurations de chargement et les paramètres de traitement. Ces dernières années, la dynamique des fluides numérique (CFD) et l'apprentissage automatique (ML) se sont imposés comme des outils puissants pour l'analyse et l'optimisation des processus industriels de traitement thermique. Malgré leur potentiel, la recherche existante s'est principalement concentrée sur des systèmes de petite échelle ou des fours à gaz, laissant les fours électriques industriels sous-explorés. Afin de combler ces lacunes, cette étude intègre des mesures expérimentales, des simulations CFD, une optimisation multi-objectifs et une modélisation prédictive basée sur l'apprentissage automatique afin d'améliorer l'uniformité des températures, de réduire les temps de traitement et d'optimiser l'efficacité énergétique des fours industriels électriques de traitement thermique. En évaluant de manière systématique les configurations d'empilement, l'agencement des éléments chauffants et les stratégies de chargement prédictives, cette recherche propose un cadre méthodologique complet pour améliorer le contrôle du processus et garantir des propriétés mécaniques homogènes dans les composants en acier de grande taille.

Un modèle CFD tridimensionnel transitoire a été développé pour simuler les caractéristiques thermiques et aérodynamiques d'un four industriel électrique à sole mobile de 112 m^3. Ce four, situé chez Finkl Steel (Sorel, Québec), est équipé de plusieurs éléments chauffants électriques et de ventilateurs axiaux pour assurer une convection forcée, et son comportement thermique a été analysé sous différentes configurations de chargement. La géométrie CAO du four et des pièces forgées dans divers scénarios a été conçue à l'aide de CATIA V5 afin de garantir une représentation fidèle des conditions industrielles. Pour valider le modèle, des mesures de température ont été effectuées sur des blocs de forge industriels à l'aide de thermocouples embarqués stratégiquement placés sur des positions critiques de surface. Ces mesures ont

permis de capturer les gradients thermiques en temps réel et de les comparer directement aux résultats de simulation. ANSYS® (versions 2022 et 2023) a été utilisé pour les simulations CFD et le maillage, tandis que JMatPro ® a permis de déterminer les propriétés mécaniques dépendantes de la température du matériau forgé, garantissant ainsi des entrées thermophysiques précises pour les simulations numériques. L'analyse CFD a révélé des non-uniformités de température significatives, atteignant 300 K dans les configurations d'empilement conventionnelles, notamment dans les arrangements multi-blocs où des obstructions du flux d'air et un échange radiatif insuffisant ont entraîné des zones de surchauffe et de sous-chauffe localisées. L'intégration des simulations CFD aux données industrielles en temps réel a servi de base à l'optimisation des stratégies de chargement du four et de la disposition des éléments chauffants. Pour la visualisation et le post-traitement des résultats de simulation, Tecplot 360 EX a été employé pour analyser efficacement les champs de température et les caractéristiques de l'écoulement.

Des techniques d'optimisation multi-objectifs ont été mises en œuvre afin d'affiner les paramètres de fonctionnement du four, en se concentrant sur la réduction des écarts de température tout en maintenant l'efficacité du processus. Un algorithme génétique (GA) et une approche d'optimisation basée sur la méthode Pareto ont été appliqués afin d'examiner l'impact de l'agencement des éléments chauffants sur l'uniformité thermique globale. MATLAB 2021 a été utilisé pour implémenter les routines d'optimisation, permettant une exécution efficace des algorithmes génétiques et des recherches de Pareto. L'approche de modélisation par substitution, utilisant une régression polynomiale, a permis une évaluation rapide de différentes configurations de conception sans nécessiter une exécution complète des simulations CFD à chaque itération. Les résultats ont démontré que des dispositions optimisées des éléments chauffants pouvaient réduire les variations de température de surface de 8 %, tandis que des configurations de chargement améliorées permettaient de diminuer les écarts de température cœur-surface de 35 %. Ces résultats soulignent l'importance des améliorations systématiques de la conception des fours pour garantir un chauffage homogène des pièces forgées en acier de grande dimension.

Afin d'améliorer davantage l'efficacité opérationnelle, un modèle prédictif basé sur l'apprentissage automatique a été développé en exploitant un ensemble de données industrielles de plus de 1 100 cycles de revenu. Python 3.1 a été utilisé pour développer et entraîner ce modèle, en appliquant des techniques avancées de prétraitement des données, y compris l'ingénierie des caractéristiques, les transformations et l'ajustement des hyperparamètres. L'outil d'analyse de régression XGBoost a été utilisé afin de prédire les cycles de chargement optimaux en fonction de variables opérationnelles clés, notamment les dimensions des pièces forgées, leur composition matérielle et l'historique thermique du four. En analysant les données de processus historiques, le modèle a fourni des recommandations en temps réel pour les configurations de chargement, réduisant ainsi significativement la dépendance aux heuristiques empiriques et à la planification manuelle. Le modèle d'apprentissage automatique a atteint un coefficient de détermination R^2 compris entre 0,78 et 0,89, démontrant son efficacité dans la prédiction précise des paramètres optimaux de chargement, tout en réduisant la consommation d'énergie et le temps de traitement. L'intégration de l'analyse prédictive basée sur l'IA dans les opérations du four renforce

l’adaptabilité, permettant aux opérateurs d’optimiser le débit de production sans nécessiter d’ajustements par essais et erreurs.

Les résultats de cette recherche soulignent le potentiel de la combinaison des validations expérimentales, de la modélisation CFD haute-fidélité, de l'optimisation multi-objectifs et de l'apprentissage automatique pour améliorer l’efficacité des fours industriels électriques de traitement thermique. Le cadre CFD validé constitue un outil puissant d’analyse de scénarios, permettant une évaluation précise de différentes configurations de four et stratégies de chargement. Parallèlement, le modèle d’apprentissage automatique améliore la prise de décision en temps réel en fournissant des informations rapides et basées sur les données pour optimiser les opérations du four. L'intégration de ces méthodologies établit une approche globale et évolutive visant à optimiser les processus de traitement thermique, en offrant une solution efficace et adaptée aux applications industrielles.

Les perspectives de recherche futures incluent l’extension des modèles d’apprentissage automatique pour prédire les propriétés mécaniques finales en fonction de l’historique thermique, le perfectionnement des modèles de turbulence et de radiation en CFD afin d'améliorer la précision des simulations, ainsi que l'exploration de techniques d'optimisation adaptative en temps réel pour ajuster dynamiquement les conditions de fonctionnement du four. En exploitant la synergie entre la modélisation physique et l’analyse de données, cette recherche contribue à l’avancement des stratégies de contrôle prédictif et prescriptif dans le domaine du traitement thermique métallurgique, favorisant une production industrielle à la fois écoénergétique et de haute qualité.

Mots-clés: Traitement thermique, Grandes pièces forgées en acier, Fours électriques, Éléments chauffants, Chargement du four, Simulation CFD, Apprentissage automatique, Optimisation multi-objectifs, Algorithme génétique, Modélisation par substitution, Uniformité thermique

Optimization of the Tempering Heat Treatment Cycle of Large Size Forgings

Sajad MIRZAEI

ABSTRACT

The heat treatment of large steel forgings plays a crucial role in achieving the desired mechanical properties essential for various industrial applications, including aerospace, automotive, and heavy machinery. The tempering process, a key stage in heat treatment, significantly influences material performance by modifying microstructures to enhance toughness, hardness, and wear resistance. However, maintaining uniform temperature distribution within large-scale industrial electric furnaces remains a critical challenge due to complex thermal interactions, large temperature gradients, and energy inefficiencies. Traditional empirical approaches for optimizing the heat treatment process are often inadequate, as they fail to account for the intricate interplay between furnace design, loading configurations, and process parameters. In recent years, computational fluid dynamics (CFD) and machine learning (ML) have emerged as powerful tools for analyzing and optimizing industrial heat treatment processes. Despite their potential, existing research primarily focuses on small-scale systems or gas-fired furnaces, leaving industrial-scale electric furnaces underexplored. Addressing these gaps, this study integrates experimental measurements, CFD simulations, multi-objective optimization, and ML-based predictive modeling to enhance temperature uniformity, reduce processing times, and improve energy efficiency in industrial electric heat treatment furnaces. By systematically evaluating stacking patterns, heating element layouts, and predictive loading strategies, this research provides a comprehensive framework for improving process control and achieving consistent mechanical properties in large steel components.

A transient three-dimensional CFD model was developed to simulate the thermal and flow characteristics within a 112 m^3 car-bottom industrial electric furnace. The furnace, located at Finkl Steel (Sorel, Quebec), was equipped with multiple electrical heating elements and axial fans to ensure forced convection, and its thermal behavior was analyzed under various loading configurations. The CAD geometry of the furnace and forging blocks in different scenarios were designed using CATIA V5 to ensure high-fidelity representation of industrial conditions. To validate the model, experimental temperature measurements were obtained from industrial forging blocks using embedded thermocouples strategically placed at critical surface positions. These measurements captured real-time thermal gradients, allowing direct comparison with simulation results. ANSYS® (versions 2022 and 2023) was employed for CFD simulations and meshing, while JMatPro® was employed to determine the temperature-dependent mechanical properties of the forging material, ensuring accurate thermophysical inputs for CFD simulations. The CFD analysis revealed significant temperature non-uniformities of up to 300 K in conventional stacking patterns, particularly in multi-block arrangements where airflow obstructions and inadequate radiative exchange contributed to localized overheating

and underheating. The integration of CFD simulations with real-time industrial data provided the foundation for optimizing furnace loading strategies and heating element placements. For visualization and post-processing of simulation results, Tecplot 360 EX was utilized to interpret temperature fields and flow characteristics effectively.

Multi-objective optimization techniques were employed to refine the furnace operating parameters, focusing on minimizing temperature differentials while maintaining processing efficiency. A genetic algorithm (GA) and Pareto-based optimization framework were implemented to explore the impact of heating element layout on overall temperature uniformity. MATLAB 2021 was used to implement the optimization routines, enabling efficient execution of genetic algorithms and Pareto searches. The surrogate modeling approach, using polynomial regression, enabled rapid evaluation of various design configurations without requiring full CFD simulations for each iteration. Results demonstrated that optimized heating element layouts could reduce surface temperature variations by 8%, while improved stacking configurations reduced core-to-surface temperature differentials by 35%. These findings emphasize the importance of systematic furnace design improvements in achieving uniform heating across large-scale steel forgings.

To further enhance operational efficiency, a machine learning predictive model was developed using an extensive dataset of over 1,100 industrial tempering logs. Python 3.1 was employed to develop and train a predictive model, utilizing robust preprocessing techniques, including feature engineering, transformation methods, and hyperparameter tuning. The XGBoost regressor was trained to predict optimal loading cycles based on key operational variables, including forging dimensions, material composition, and furnace thermal history. By analyzing historical process data, the model provided real-time recommendations for loading configurations, significantly reducing reliance on empirical heuristics and manual scheduling. The ML model achieved an R^2 of 0.78–0.89, demonstrating its effectiveness in accurately predicting optimal loading parameters while reducing energy consumption and processing time. The integration of ML-based predictive analytics into furnace operations enhances adaptability, allowing operators to optimize throughput without requiring extensive trial-and-error adjustments.

The findings of this research underscore the potential of combining experimental validation, high-fidelity CFD modeling, multi-objective optimization, and data-driven machine learning to improve the efficiency of industrial electric heat treatment furnaces. The validated CFD framework serves as a powerful tool for scenario analysis, enabling precise evaluations of different furnace configurations and loading strategies. Meanwhile, the ML model enhances real-time decision-making by providing rapid, data-driven insights into optimal furnace operations. The integration of these methodologies establishes a holistic approach to improving heat treatment processes, offering a scalable and computationally efficient solution for industrial applications.

Future research directions include extending machine learning frameworks to predict final mechanical properties based on thermal history, further refining CFD turbulence and radiation models to improve simulation accuracy, and exploring real-time adaptive optimization

techniques for dynamically adjusting furnace operating conditions. By leveraging the synergy between physics-based modeling and data-driven analytics, this research contributes to the advancement of predictive and prescriptive control strategies in metallurgical heat treatment, facilitating energy-efficient, high-quality production in industrial settings.

Keywords: Heat treatment, Large steel forgings, Electric furnaces, Heating element, Furnace loading, CFD simulation, Machine learning, Multi-objective optimization, Genetic algorithm, Surrogate modeling, Temperature uniformity

TABLE OF CONTENTS

Page

LIST OF TABLES

Page

LIST OF FIGURES

Page

LIST OF ABREVIATIONS

3D	Three Dimensional
AFWE	All Four Walls Equipped
AWICE	All Walls Including Ceiling Equipped
CFD	Computational Fluid Dynamics
Config	Configuration
DO	Discrete Ordinates Model
DSK	Double Skid
DSKC	Double Skid + Central Spacer Skid
DTRM	Discrete Transfer Radiation Model
GA	Genetic Algorithm
HT	Heat Treatment
IQR	Interquartile Range
LB	Lower Block
MAAPE	Mean Arctangent Absolute Percentage Error
ML	Machine Learning
MSE	Mean Square Error
norm	Normalized Value
OCE	Only Ceiling Equipped
OHE	One-Hot Encoding
PDP	Partial Dependence Plot
PID	Proportional–Integral–Derivative
PS	Pareto Search
Q&T	Quench and Temper
Q-Q	Quantile-Quantile
RANS	Reynolds-Averaged Navier–Stokes Equations
RMSE	Root Mean Squared Error
R-sq	Root Square
RTE	Radiative Transfer Equation

S2S	Surface to Surface
SHAP	Shapley Additive Explanations
std	standard Deviation
TC	Thermocouple
TSWE	Two Side Walls Equipped
UB	Upper Block
VEF	Vertical Electric Furnace
wt%	Weight Percent
XGBRegressor	Xtreme Gradient Boosting Regressor

LIST OF SYMBOLS

Latin symbols

a	Absorption coefficient (m^{-1})
C_p	Specific heat (J kg^{-1} K^{-1})
e	Error term
$F_i(x)$	Objective function
g	Gravity (m s^{-2})
h	Enthalpy (J kg^{-1})
Hz	Frequency (Hz)
i	Function index
I	Radiative intensity
k	Turbulence kinetic energy (m^2 s^{-2})
K	Thermal conductivity (W m^{-1} K^{-1})
n	Degree of polynomial
N	Number of decision variables
p	Pressure (Pa)
P	Power (kW)
P_k	Turbulent kinetic energy production
$\vec{r}$	Position vector
$\vec{s}$	Direction vector
S	Heat sources (J m^{-3} s^{-1})
t	Time (s)
t_T	Total time
T	Temperature (°C)
UDF	User-defined function
V	Voltage (v)
x	Independent variable
x*	Reference point
X, Y, Z	Direction of coordinate axes

XXX

y	Dependent variable
Greek symbols	
τ	Stress tensor
μ_t	Turbulence eddy viscosity
ω	Angular velocity vector (rad s^{-1})
v	Velocity vector (m s^{-1})
ρ	Density (kg m^{-3})
β	Constant coefficients
ε	Turbulence dissipation rate (m^2 s^{-3})
σ	Stefan-Boltzmann constant

INTRODUCTION

Motivation for the Study

In the steel manufacturing industry, the heat treatment process plays a vital role in achieving the desired mechanical properties of low-alloy steel components. These properties, such as hardness, toughness, and resistance to wear, are critical for applications in the energy, transportation, and heavy machinery sectors (Bhadeshia & Honeycombe, 2017). The tempering process, a key stage of heat treatment, enables essential microstructural transformations and stress relief, directly impacting product quality (Dossett & Totten, 2013; Totten, 2006). However, achieving uniform mechanical properties in large-size forgings, which can reach up to 32 metric tons, is a persistent challenge due to the scale of the products and the inherent complexity of heat transfer within industrial furnaces (Bohlooli Arkhazloo, 2020).

Temperature and time are pivotal factors in determining the success of the heat treatment process (Liščić & Filetin, 1987). Non-uniform temperature distribution during the heating and holding phases can result in undesirable microstructural variations, leading to suboptimal mechanical properties or even part rejection. Similarly, prolonged or inadequate holding times can adversely affect the metallurgical transformations required for tempering, thus impacting product reliability and production efficiency (Charles, Deskevich, Varkey, Voigt, & Wollenburg, 2004; Totten, 2006). These challenges become even more pronounced in large-scale components, where internal and surface temperature gradients can vary significantly throughout the process (Gur & Pan, 2008).

Historically, gas-fired furnaces have dominated the heat treatment industry, but tightening environmental regulations and the rising demand for energy efficiency have encouraged a shift toward electric furnaces (International Energy Agency, 2024). While electric furnaces hold great promise for reducing carbon footprints and ensuring precise control of heating cycles, they present unique design and operational challenges. Factors such as the layout of heating elements, airflow circulation, heat transfer modes, and the timing of heating and holding

periods significantly affect temperature uniformity and energy efficiency. Addressing these challenges requires advanced analysis and optimization tools, as traditional empirical methods often fail to deliver the necessary accuracy for large-scale industrial processes.

Problem Definition

Despite advancements in furnace design and heat treatment practices, significant knowledge gaps remain in understanding and optimizing thermal interactions within large-scale electric furnaces. Non-uniform temperature distributions during the tempering process can lead to inconsistent mechanical properties, increasing the likelihood of product rejection and resource waste (Bohlooli Arkhazloo, 2020). The interaction between loading patterns, heating element configurations, furnace thermal cycles, and airflow dynamics further complicates the optimization process.

A major issue is the interdependence of time and temperature during the tempering cycle, where insufficient heating time may leave microstructures underdeveloped, while prolonged heating can degrade material properties or waste energy (Canale, Yao, Gu, & Totten, 2008). Additionally, accurately predicting transient temperature profiles during long-duration processes (such as tempering) remains a significant challenge. These issues demand a precise understanding of the conjugate heat transfer mechanisms within the furnace and their impact on steel components.

Existing research predominantly focuses on gas-fired furnaces or laboratory-scale electric furnaces with chamber volumes below 0.05 m^3, leaving industrial-scale electric furnaces, which have chamber volumes exceeding 112 m^3, largely underexplored. Additionally, while cutting-edge computational tools such as CFD (Computational Fluid Dynamics) are indispensable in mechanical engineering for their exceptional accuracy in analyzing complex thermal and fluid interactions, they remain computationally intensive for long-duration processes such as tempering, which can last up to 44 hours. This limitation becomes particularly critical in fast-paced industrial settings, where rapid decision-making is required. Machine learning (ML) offers a complementary approach by leveraging data-driven insights

to enhance optimization efforts, bridging the gap between detailed simulation capabilities and the need for efficient industrial application.

Objectives of the Research

This research aims to address the aforementioned challenges through a multi-faceted approach that combines experimental analysis, numerical simulations, and machine learning techniques. The main objectives of this study are:

1. Optimize loading patterns and stacking configurations to enhance temperature uniformity in large-size steel forgings.
2. Improve furnace design by analyzing the influence of heating element layouts and airflow circulation on heat transfer dynamics.
3. Develop and validate predictive tools, including CFD models and ML-based algorithms, for optimizing the tempering process with minimal computational cost.
4. Propose practical recommendations for improving energy efficiency and product quality in industrial electric heat treatment furnaces.

Thesis Organization

This dissertation is structured into seven chapters, each addressing a specific component of the research framework, from foundational principles to experimental studies and computational modeling, culminating in key findings and future directions.

Chapter 1 provides a comprehensive overview of heat treatment processes in large-scale industrial electric furnaces. It introduces the critical challenge of achieving temperature uniformity in large steel forgings and discusses the limitations of conventional empirical approaches in optimizing heat treatment processes. The chapter also reviews recent advances in computational fluid dynamics (CFD) and machine learning (ML) applications in industrial heat treatment and identifies the existing research gaps that this study aims to address.

Chapter 2 outlines the methodological framework of this research, detailing the experimental setup, numerical simulations, and machine learning approaches employed. The governing

equations, boundary conditions, and turbulence and radiation modeling techniques used in CFD simulations are presented. The methodology for validating numerical models against experimental data is discussed, along with the optimization frameworks applied for improving furnace efficiency. This chapter also describes the preprocessing techniques and training methodologies used for developing the ML-based predictive model.

Chapters 3 to 5 present the three studies conducted during this research, each focusing on a key aspect of furnace performance and process optimization. Chapter 3 investigates the influence of spacers and skid sizes on heat treatment efficiency in an industrial electric furnace. The chapter analyzes the thermal behavior of large steel forgings under different support configurations and examines their impact on temperature uniformity. The CFD results, validated against experimental measurements, reveal optimal skid and spacer dimensions for reducing temperature non-uniformities.

Chapter 4 focuses on the influence of heating element layouts on temperature uniformity within large-scale electric heat treatment furnaces. It explores various heating element configurations using CFD simulations and multi-objective optimization techniques to identify the optimal arrangement for achieving uniform heating. The findings highlight the significance of strategic heating element placement in minimizing thermal gradients and improving energy efficiency.

Chapter 5 presents the development and implementation of a machine learning predictive model for optimizing the furnace loading cycle. A dataset of 1,162 industrial tempering logs is used to train an XGBoost-based regression model, which predicts batch-level parameters—total weight, forging count, and total length—based on geometric and process features, guiding efficient loading decisions. The predictive model enhances operational efficiency by reducing reliance on empirical heuristics, enhancing throughput while supporting more efficient use of heating cycles.

Conclusion and Recommendations synthesize the key findings from the previous chapters, summarizing the contributions of this research to the field of industrial heat treatment and

outlining future research directions. The chapter discusses how the integration of CFD modeling, optimization techniques, and machine learning enables more efficient and precise process control in electric heat treatment furnaces. The limitations of the study and potential sources of uncertainty are also addressed.

By incorporating experimental, numerical, and data-driven methodologies, this thesis provides a systematic approach to optimizing heat treatment in industrial electric furnaces, bridging the gap between academic research and industrial practice. The work resulted in three journal publications and presentations at three international conferences. Several of the findings have also been applied successfully in an industrial setting over the past two years.

CHAPTER 1

LITERATURE REVIEW

1.1 Overview of Heat Treatment Processes

Heat treatment processes are a cornerstone of modern metallurgical engineering, improving material performance by controlling microstructures through tailored thermal cycles. These treatments are vital for enhancing mechanical properties such as hardness, toughness, wear resistance, and ductility, which are key requirements in industries ranging from aerospace and automotive to heavy machinery (Totten, 2006). In these applications, components are often exposed to high stress or extreme thermal conditions, demanding precisely designed heat treatment protocols to ensure structural integrity and long-term performance. The fundamental principle of heat treatment lies in thermally activated phase transformations that occur during controlled heating and cooling cycles (Bhadeshia & Honeycombe, 2017). Although the sequence may vary depending on the alloy system and desired outcomes, three major steps are commonly applied (Brooks, 1996):

- **Austenitization:** Heating into the austenite region to enable transformation, typically as a precursor to quenching or normalizing.
- **Quenching:** Rapid cooling in water, oil, or polymer solutions to induce martensitic transformation. This step, though essential for hardening, may introduce high residual stresses and distortion if not carefully managed.
- **Tempering:** Reheating to a moderate temperature to relieve brittleness from quenching and improve ductility without severely compromising hardness.

Among the above thermal stages, tempering is especially critical for heavy-section steels such as turbine shafts, die blocks, and large forgings, where component size may exceed 30 tons. In such large-scale applications, with characteristic half-thicknesses ranging from 0.3 to 0.7 meters, the Biot number (Bi) far exceeds unity, meaning that internal temperature evolution is strongly limited by conductive heat transfer (Bouissa et al., 2020). Consequently, this demands

long soaking times and careful thermal management to ensure metallurgical uniformity across the entire cross-section (Committee, 1991; Dossett & Totten, 2013; Rakhit, 2000). Such uniformity is critical because, during tempering, brittle martensite transforms into more ductile structures, while quench-induced residual stresses are relaxed. These microstructural changes are essential for enhancing toughness and reducing the risk of crack initiation or propagation under service loads (Canale et al., 2008).

As illustrated in Figure 1.1, tempering involves a distinct holding phase at moderately elevated temperatures (between 400 and 600C), during which diffusion-driven transformations occur across the part's volume. This is particularly demanding in large forgings, where long thermal diffusion times and high thermal mass significantly delay uniform temperature development (Kaymak, 2007). Therefore, achieving thermal homogeneity in such cases becomes a fundamental operational challenge. Thus, the tempering of large-scale components is not simply a scaled-up version of small-part processes, rather, it introduces new physical regimes, time scales, and furnace design constraints that require advanced analysis (Bohlooli Arkhazloo, 2020). These combined scientific and operational challenges form the foundation of this thesis. The next sections will explore how component size, furnace characteristics, and process complexity interact to enable efficient and uniform tempering, an issue at the heart of the research problem.

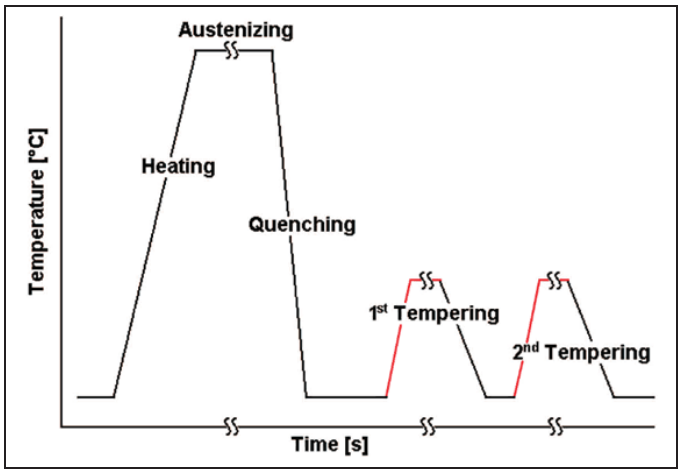

Figure 1.1 Schematic diagram of heat treatment processes
Taken from Kaymak (2007, p. 2)

1.2 Challenges in Heat Treatment of Large-Size Forgings

The heat treatment of large-size forgings presents a distinct set of challenges, stemming from their substantial scale, complex geometries, and complex thermal interactions. These factors critically affect not only the metallurgical quality and mechanical performance of the final product but also the operational efficiency and sustainability of the process. Consequently, the heat treatment of large forgings remains one of the most technically demanding and energy-intensive applications in metallurgical engineering (Bohlooli Arkhazloo, 2020; Dossett & Totten, 2013; Totten, 2006).

1.2.1 Heat Transfer Inefficiencies

Large-size forgings inherently experience pronounced thermal gradients due to non-uniform heat transfer mechanisms within both the part and the furnace environment. Heat conduction, which governs thermal transport within solids, proceeds slowly over large cross-sections, leading to delayed heat penetration and significant temperature differences between the surface and core. This internal lag can result in non-uniform phase transformations and residual stress accumulation during heating cycles (Bohlooli Arkhazloo, 2020; Mullinger & Jenkins, 2022).
At the furnace level, non-uniformity is further exacerbated by limitations in convection and radiation. Inadequate circulation of heated air or non-ideal radiation patterns within the furnace can amplify surface-level temperature imbalances. These effects become especially severe in components with irregular geometries—such as sharp edges or variable thickness regions—which are prone to localized underheating or overheating. Ultimately, such thermal non-uniformities compromise microstructural homogeneity and reduce the reliability of heat treatment outcomes (Dossett & Totten, 2013; Mullinger & Jenkins, 2022).

1.2.2 Geometric and Material Considerations

The geometry and material composition of large forgings add another layer of complexity. Thicker cross-sections and intricate shapes as shown in Figure 1.2 disrupt uniform heat

absorption, often resulting in thermal shadowing effects, where certain areas receive less heat than others. In parallel, material heterogeneity introduces metallurgical sensitivity to thermal history. Alloying elements such as chromium, nickel, and molybdenum—commonly used to improve strength and toughness—modify transformation temperatures and slow diffusion rates, making thermal cycles highly composition-dependent (Dossett & Totten, 2013). Additionally, different regions within the same forging may require distinct soaking or cooling times, due to localized variations in thickness or alloy composition. These variations increase the likelihood of differential stresses and can lead to distortion or cracking if not carefully managed (Totten, 2006).

Figure 1.2 Real scale large-size forging with an intricate geometry

1.2.3 Multi-Block Loading Configurations

In industrial settings, large-scale heat treatment often involves multi-block loading, as shown in Figure 1.3, where multiple components are placed together within the same furnace to optimize throughput. However, the proximity of blocks introduces additional challenges. Thermal interactions between adjacent blocks can lead to shadowing, localized overheating, and non-uniform airflow circulation (Nima Bohlooli Arkhazloo, Bazdidi-Tehrani, Jadidi, Morin, & Jahazi, 2021; Committee, 1991). For instance, when two large forgings are placed

side by side, the inner surfaces facing each other may experience reduced radiant heat exchange, leading to lower local temperatures.

Figure 1.3 Sample of multi-block loading

Studies have shown that optimized stacking patterns, including the use of spacers and carefully designed skids, can mitigate these issues by promoting better airflow and heat transfer (Bohlooli Arkhazloo, 2020). In some cases, computer-aided simulation tools have been used to simulate airflow paths, informing the placement of blocks to minimize temperature differentials throughout the load.

1.2.4 Process Parameters: Time and Temperature

Time and temperature are central parameters in heat treatment operations. Insufficient holding times at the target temperature can lead to incomplete stress relief or underdeveloped microstructures, while excessive durations may cause grain growth, reduced hardness, and unnecessary energy expenditure. These effects are magnified in large forgings due to significant internal temperature gradients between the surface and the core (Dossett & Totten, 2013).

The high thermal mass of forgings also necessitates prolonged heating and cooling cycles, thereby increasing energy consumption and operational costs. Achieving an optimal balance between process duration, temperature, and energy efficiency remains a significant challenge in the industry. Moreover, operators must carefully track the thermal history of each block to ensure that metallurgical requirements—such as hardness and toughness—are met in all regions of the forging (Dossett & Totten, 2013).

1.2.5 Energy and Environmental Concerns

Large-size forgings demand extended thermal cycles, which inherently consume large amounts of energy and generate substantial heat losses. Conventional furnace systems, often experience significant inefficiencies—leading to elevated fuel consumption, high operational costs, and increased greenhouse gas emissions. These concerns are especially pressing in the steel sector, which relies heavily on high-temperature heat for critical metallurgical operations (International Energy Agency, 2024; Mullinger & Jenkins, 2022).

Figure 1.4 illustrates the distribution of industrial energy demand across temperature ranges and the share of fossil fuels under various policy scenarios, including the Stated Policies Scenario (STEPS), Announced Pledges Scenario (APS), and Net Zero Emissions Scenario (NZE). In the STEPS scenario, over 50% of the energy demand for processes above 400°C is still supplied by fossil fuels, underscoring the sector's current dependence (International Energy Agency, 2024). Transitioning away from fossil sources remains a significant technical and economic challenge, particularly for high-mass components like large forgings.

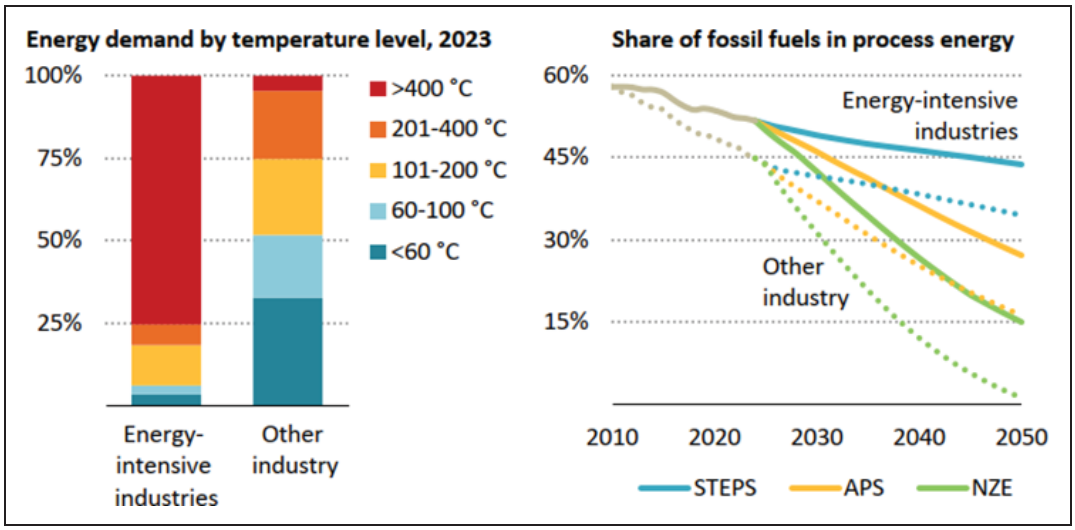

Figure 1.4 Energy demand by temperature level and fossil fuel use in industry by type and scenario
Taken from International Energy Agency (2024, p. 119)

Whereas the STEPS scenario reflects limited progress, the shift toward APS and NZE scenarios involves a growing reliance on electricity and renewables for high-temperature processes. Achieving these targets will demand innovation in furnace insulation, design, and process parameters optimization, particularly for heat treatment applications such as tempering, where long heating cycles and large thermal loads dominate.

1.2.5.1 Technological Solutions and Environmental Implications

The gradual replacement of fossil-fuel-fired furnaces with electric systems powered by renewable grids is emerging as a promising strategy for reducing carbon emissions in high-temperature applications (Pfeifer, 2017). In regions like Quebec, where low-carbon electricity is readily available, the deployment of industrial electric furnaces not only improves environmental performance but also enables tighter control over temperature distribution, ultimately contributing to higher product quality.

However, this shift entails considerable investment in infrastructure and technology. As shown in recent studies and industrial trials, merely switching the energy source is insufficient; the

entire system architecture, from furnace loading pattern to thermal management strategies, requires re-optimization (Bohlooli Arkhazloo, 2020). These developments are essential to meet the performance improvements and emission reductions projected in the APS and NZE scenarios (Mullinger & Jenkins, 2022).

In this context, digital tools such as machine learning (ML) and computational fluid dynamics (CFD) are gaining relevance. ML models, trained on historical furnace operation data, can improve parameter prediction and reduce human error. Concurrently, CFD simulations offer detailed insights into flow behavior, heat transfer, and radiation distribution, allowing identification of design inefficiencies and enabling virtual testing of design (exploration of "what-if" design) alternatives without costly physical trials. Additionally, technologies such as recuperative and regenerative heat exchangers enable partial recovery of exhaust heat, reclaiming up to 70% of energy that would otherwise be lost. When integrated into modern furnace systems, especially during transitional phases from gas to electric operation, these technologies can significantly reduce energy use and emissions (Mullinger & Jenkins, 2022).

1.2.5.2 Future Outlook

The steel industry's reliance on high-temperature thermal processes, as emphasized in Figure 1.4, underscores the urgency of adopting cleaner technologies on a broad scale. Government incentives, carbon pricing mechanisms, and targeted research funding will be key in supporting this transition. International frameworks—such as the recent COP28 agreements—reinforce the need to decarbonize energy-intensive sectors in line with global climate goals, including the 1.5°C target (International Energy Agency, 2024). By integrating furnace design improvements with renewable energy adoption, the steel industry can simultaneously address operational efficiency and environmental responsibility, shaping a more sustainable future for the steel industry's long-term heat treatment strategy.

1.3 Electric vs. Gas-Fired Furnaces for Heat Treatment

Choosing between electric and gas-fired furnaces is a central decision in industrial heat treatment, especially for large-scale applications where performance, energy efficiency, and emissions are tightly interlinked. Both technologies offer distinct advantages and limitations, necessitating careful consideration of factors such as specific product requirements, process parameters, energy costs, and environmental regulations. As global policies increasingly emphasize sustainability, the debate over which furnace type to adopt has intensified, driving further research and innovation in both approaches (Committee, 1991; Mullinger & Jenkins, 2022).

1.3.1 Gas-Fired Furnaces: Strengths and Limitations

Gas-fired furnaces have long been the dominant technology for industrial heat treatment due to their mature design framework and proven track record. One of the most common types, the batch-type car bottom furnace used in the steel industry, is shown in Figure 1.5, located at Sorel Forge. The key strengths of gas-fired furnaces include (Baukal Jr, 2004; Mullinger & Jenkins, 2022):

1. **High Energy Density:** Combustion of natural gas releases substantial thermal energy, enabling fast ramp-up times and efficient bulk heating. This makes gas-fired furnaces suitable for large-scale, high-throughput operations where short cycle times are essential.
2. **Lower Initial Capital Cost:** Compared to electric furnaces, gas-fired systems often have lower capital costs, especially when scaled up for larger furnace sizes.
3. **Operational Familiarity:** Decades of industrial use have generated extensive practical knowledge, robust control systems, and trained personnel, leading to high operational confidence in gas-fired technology.

Figure 1.5 Industrial car bottom gas-fired heat treatment furnace

However, gas-fired furnaces also face significant limitations:

1. **Non-Uniform Heating:** Burner placement can result in localized hot spots and uneven temperature distribution, particularly in large or geometrically complex forgings. This can compromise microstructural uniformity and mechanical properties.
2. **Environmental Burden:** Combustion processes generate substantial greenhouse gas emissions (e.g., CO_2, NO_x), making gas-fired systems less favorable in regions with strict emissions regulations or carbon pricing mechanisms.
3. **Thermal Inefficiencies:** A substantial portion of thermal energy is lost through exhaust gases and furnace openings. Frequent door operation and batch loading further reduce overall efficiency.

Recent technological advancements aim to reduce these drawbacks. Cleaner combustion technologies, such as low-NO_x burners and enhanced burner configurations, are being developed to improve heating uniformity and reduce emissions. Additionally, research into alternative fuels, such as hydrogen blends, shows promise for lowering the carbon footprint while leveraging existing furnace infrastructure with minimal retrofitting requirements (Baukal Jr, 2004).

1.3.2 Electric Furnaces: A Cleaner Alternative

Electric furnaces have gained traction as a viable and cleaner alternative to gas-fired systems, especially in regions like Quebec, where electricity is predominantly generated from renewable sources (Halin, 2024; Pineau, 2025). One such example, an industrial electric heat treatment furnace located at Sorel Forge, is shown in Figure 1.6. The key advantages of electric furnaces include (Cresko et al., 2022; U.S. Department of Energy, 2015):

1. **Precise Temperature Control:** Electric heating elements enable highly accurate and uniform temperature regulation, minimizing internal thermal gradients. This precision supports more consistent microstructural outcomes, which is essential for large forgings requiring tight thermal tolerances.
2. **Zero On-Site Emissions:** Electric furnaces do not produce direct emissions at the facility level, making them inherently more environmentally friendly than combustion-based systems.
3. **Higher Theoretical Efficiency:** The absence of combustion gases and flue losses allows for more direct energy transfer to the load, enhancing system efficiency, and assuming stable access to affordable and low-carbon electricity.

Figure 1.6 Industrial batch-type car bottom electrical furnace

Despite these advantages, electric furnaces face challenges (Cresko et al., 2022):

1. **Higher Operating Costs:** Electricity prices, particularly in industrial sectors, are often higher than natural gas prices, potentially reducing the efficiency-related cost benefits.
2. **Scalability Constraints:** Designing electric furnaces for large-scale applications requires specialized heating element layouts and robust thermal management strategies.
3. **Grid Dependency:** While electric furnaces produce no on-site emissions, their environmental impact depends on regional electricity carbon intensity.
4. **Skill and Infrastructure Transition:** Shifting from gas to electric systems necessitates the adoption of new control strategies, workforce retraining, and upgrades to facility electrical capacity and safety protocols.

Ongoing research and development efforts aim to address these limitations. Innovations in heating element materials, advanced insulation, and energy storage solutions are expected to enhance the scalability and responsiveness of electric furnaces. Additionally, integration with renewable energy and smart control systems is becoming more feasible, gradually improving the viability of low-carbon electric heat treatment across various industrial sectors.

1.3.3 Comparative Insights

Gas-fired and electric furnaces represent two ends of the technological spectrum, each offering distinct operational trade-offs (Cresko et al., 2022; U.S. Department of Energy, 2015):

- **Gas-Fired Systems:** Well-suited for high-throughput industrial operations requiring rapid heating and large batch capacities. However, they often face challenges such as non-uniform heat distribution, higher on-site emissions, and energy losses through exhaust gases and open doors.
- **Electric Systems:** Offer precise thermal control, lower on-site emissions, and better potential for integration with renewable energy sources. Nonetheless, they may encounter higher energy costs, design limitations at larger scales, and dependencies on electricity grid carbon intensity.

Hybrid furnace systems—which combine electric heating elements with gas combustion—are emerging as a promising intermediate solution. In these configurations, electric elements are used for precision control, while gas burners supplement the system with rapid heat-up capability or support during peak thermal loads. This hybrid approach may ease the transition for facilities currently equipped with gas-fired infrastructure by incrementally reducing fossil fuel dependency without requiring full system replacement (Cresko et al., 2022; U.S. Department of Energy, 2015). By understanding the technical strengths and limitations of each system, industries can make informed, context-specific decisions based on production scale, energy costs, environmental targets, and existing infrastructure.

1.3.4 Global Trends and Emerging Research Directions

The global push for decarbonization and energy efficiency is accelerating the transition toward electric furnace technologies in heat treatment applications (Pfeifer, 2017). However, challenges related to cost, infrastructure readiness, and scalability continue to limit wide-scale adoption in heavy industries. Advancements in heating element design, modular furnace architecture, and smart control systems are being developed to address these barriers (Kanthal, 2001). Gas-fired furnaces, though facing growing environmental constraints, remain relevant due to their energy density and maturity. Innovations such as low-emission burners, advanced insulation materials, and hydrogen-based fuels offer viable pathways to improve performance while reducing carbon output (Baukal Jr, 2004).

To meet future industrial demands, both furnace types will require better integration of predictive and control technologies. Digital tools such as CFD and ML are playing a critical role in this transformation. CFD enables precise simulation of heat transfer and flow behavior, guiding furnace design and operational improvements. Meanwhile, ML offers data-driven insights that can optimize scheduling, detect inefficiencies, and support decision-making in real time. These tools are especially valuable in large-scale applications, where traditional trial-and-error approaches fall short due to high thermal mass, long process durations, and complex loading configurations. The next section explores the applications of CFD in furnace studies.

1.4 CFD Applications in Furnace Optimization

Computational Fluid Dynamics (CFD) has become an essential tool in the analysis and optimization of industrial furnaces, facilitating high-fidelity modeling of heat transfer, fluid flow, and thermal interactions within complex systems. By modeling key phenomena—such as turbulence, radiative and convective heat transfer, and where relevant, chemical reactions —CFD enables a detailed understanding of furnace performance that is difficult to achieve through purely experimental methods (Bohlooli Arkhazloo, 2020; Mullinger & Jenkins, 2022; U.S. Department of Energy, 2015). Its application is particularly valuable in addressing challenges such as temperature uniformity, thermal efficiency, and scalability in heat treatment processes. In addition, CFD facilitates virtual testing of furnace configurations and operating scenarios, helping to reduce time and resource demands associated with physical trials (U.S. Department of Energy, 2015).

1.4.1 CFD in Gas-Fired Furnaces

CFD applications in gas-fired furnaces have primarily focused on analyzing and enhancing combustion behavior, burner design, and thermal uniformity under industrial-scale conditions. Given the reliance on combustion reactions, precise modeling of fuel-air mixing, reaction kinetics, and radiative heat transfer is critical for capturing the system's thermal behavior. These numerical approaches help resolve complex flow and heat transfer mechanisms that directly impact efficiency, emissions, and temperature gradients (Baukal Jr, 2004; Mullinger & Jenkins, 2022). Kislinger et al. (Kislinger et al., 2025) employed CFD simulations to evaluate hydrogen combustion in a semi-industrial reheating furnace (Figure 1.7) fitted with a low-swirl burner, aiming to characterize its effects on thermal efficiency and emission performance. Their findings showed that switching from natural gas to hydrogen reduced fuel consumption by 25% and shortened the heat-up time by 13%, primarily due to hydrogen's superior flame speed and diffusivity. This study reinforces the role of CFD as a predictive tool for case studies in high-temperature metallurgical furnaces involving multiphysics phenomena.

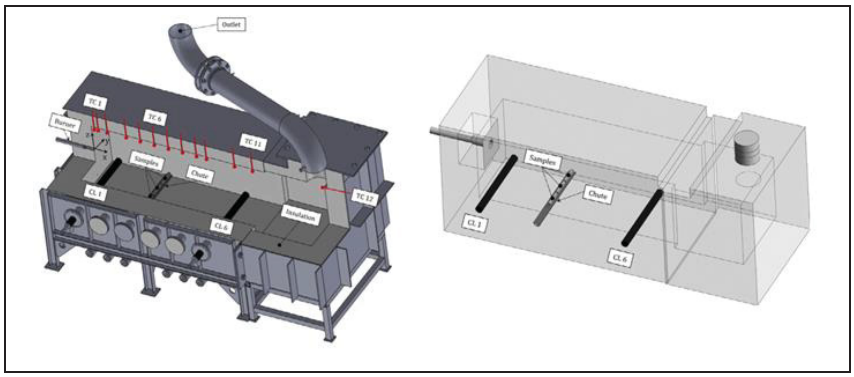

Figure 1.7 Semi-industrial reheating furnace
Taken from Kislinger et al. (2025, p. 3)

CFD has also been applied to assess fuel blending in gas-fired systems. Arroyo et al. (Arroyo, Pérez, & Cuervo-Piñera, 2023) validated a CFD model for blast furnace (Figure 1.8) gas and natural gas mixtures, showing that blends enhanced flame stability and temperature peaks compared to low-calorific BFG alone. Their model was calibrated using data from the steel plant test bench, emphasizing the role of experimental validation in achieving credible CFD outcomes. Zhuo et al. (Zhuo, Hu, & Shen, 2021) examined hydrogen injection into a blast furnace and found raceway expansion and increased reducing gas production, but with high sensitivity to boundary conditions. These works provided useful insights into how detailed thermophysical properties and boundary condition (B.C.) implementation strategies influence flow patterns and thermal fields—principles that remain valuable even in non-combustion settings requiring accurate flow control and heat distribution.

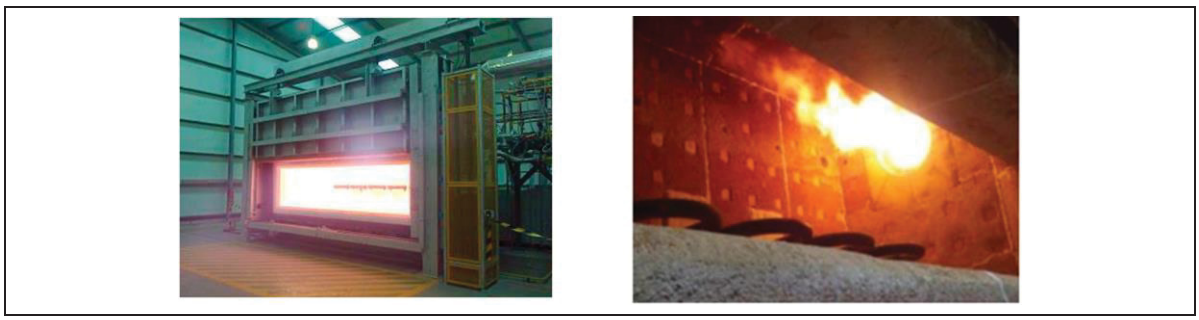

Figure 1.8 Experimental furnace for fuel blending analysis at ArcelorMittal Asturias plant
Taken from Arroyo et al. (2023, p. 3)

Arkhazloo et al. (Nima Bohlooli Arkhazloo et al., 2021) performed CFD simulations, validated by thermocouple measurements, to assess temperature distribution in a gas-fired tempering furnace treating large steel forgings (Figure 1.9). The model incorporated the Discrete Ordinates (DO) radiation method and Reynolds Stress Model (RSM), capturing up to 331 K of non-uniformity driven by geometry, loading, and burner placement. The validated CFD approach accurately reproduced heating zones, reinforcing its utility for predictive diagnostics and design improvements in large-scale tempering applications.

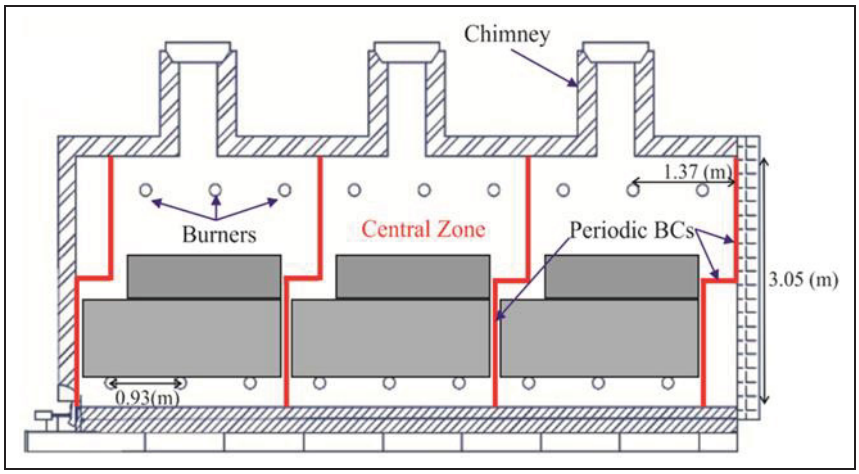

Figure 1.9 Gas-fired furnace simulated with periodic B.C.s
Taken from Nima Bohlooli Arkhazloo et al. (2021, p. 1045)

Arkhazloo et al. (N. B. Arkhazloo et al., 2019) performed coupled experimental and transient CFD simulations to analyze heating dynamics in a gas-fired furnace treating large steel forgings. By integrating k-ε turbulence, Eddy Dissipation combustion, and Discrete Ordinates radiation models, their approach captured non-uniform heating of up to 200 K, largely attributed to burner layout and internal vortex structures. Experimental validation showed deviations below 7%, reinforcing the role of view factor optimization in energy efficiency. Tang et al. (Tang et al., 2018) developed a transient 3D CFD model of a walking beam furnace incorporating real-time slab motion via dynamic mesh and UDFs, validated against instrumented slab trials at an industrial mill (Figure 1.10). The results demonstrated that zoning configuration and slab transport patterns significantly influenced discharge temperature, with

validated slab deviations under 100 K. Similarly, Mayr et al. (Mayr, Prieler, Demuth, Moderer, & Hochenauer, 2017) simulated an 18 MW pusher-type reheating furnace using a steady-state CFD approach, modeling billets as a high-viscosity laminar fluid to reduce computation time. Their model, incorporating detailed radiation and swirl/jet burner effects, matched furnace measurements with <38 K gas phase and <27 K billet deviations, highlighting the sensitivity of heating profiles to burner asymmetry and skid effects. These studies show how validated CFD models capture heating dynamics under industrial constraints.

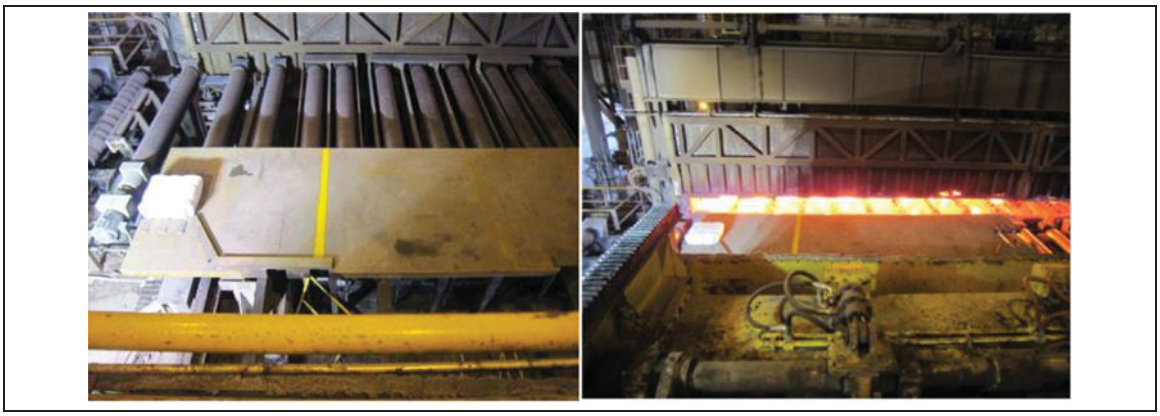

Figure 1.10 Dynamic slab charging and alignment in an industrial walking beam furnace
Taken from Tang et al. (2017, p. 781)

Zhuo and Shen (Zhuo & Shen, 2023) developed a transient CFD model to investigate coal and coke co-combustion in a blast furnace raceway, analyzing the influence of blast velocity and oxygen enrichment on burnout and flow patterns. Their results showed that increasing the blast velocity expanded the raceway by 275%, while oxygen enrichment improved coal burnout by 15%. Tang et al. (Tang et al., 2017) coupled a 3D CFD flow solver with a 2D slab heat transfer model to simulate thermal behavior in a walking beam furnace (Figure 1.11), achieving less than 2% deviation in temperature predictions. The study captured the effects of burner zoning, slab motion, and skid mark interference on heating uniformity. Yang et al. (Yang, de Jong, & Reuter, 2007) used CFD to identify heat losses in a mobile heat treatment furnace, quantifying 74% loss through off-gases and 15% through walls. Radiation plates were proposed and validated to improve retention, yielding energy savings of €342 per cycle. Similarly, Macchion

et al. (Macchion, Zahrai, & Bouwman, 2006) applied CFD to optimize flow uniformity in gas quenching chambers by redesigning the transition duct, achieving a 25% reduction in pressure drop without impairing throughput. These studies underscore CFD's versatility in addressing energy loss, flow control, and multiphysics thermal challenges in industrial heat treatment.

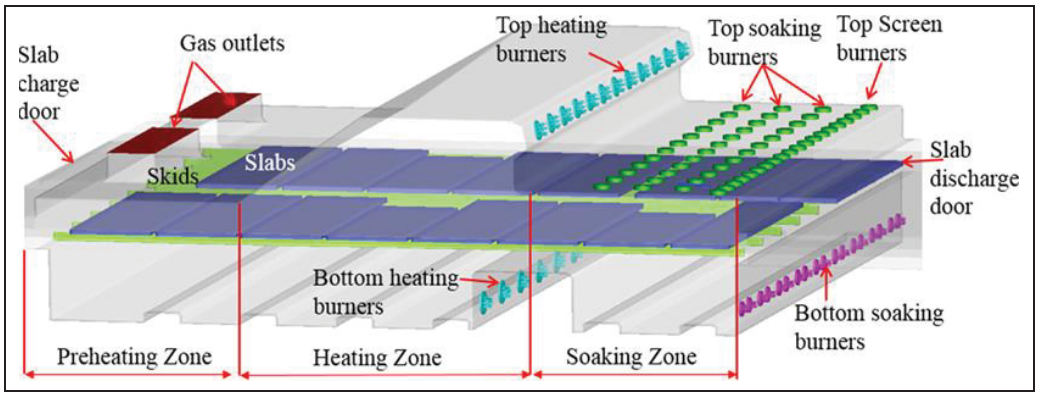

Figure 1.11 Thermal uniformity analysis of walking beam furnace
Taken from Tang et al. (2017, p. 1146)

1.4.2 CFD in Electric Furnaces

While gas-fired furnaces have been widely studied, CFD applications in electric furnaces remain mostly limited to laboratory or semi-industrial contexts. Electric furnaces rely on resistive or inductive heating elements, thus removing combustion from the heat equation but introducing new complexities in radiation-conduction balance, airflow management, and element placement. Careful modeling of natural or forced convection flows, heat transfer via surface radiation, and the furnace geometry is crucial for understanding how to achieve uniform temperature distribution. Below are examples of existing studies that emphasize thermal dynamics and airflow optimization for electric furnaces.

Angelopoulos et al. (Angelopoulos, Peppas, & Taxiarchou, 2024) developed a CFD model to optimize the thermal processing of perlite in a vertical electric furnace. The study analyzed key factors, such as feed size, air injection rates, and furnace wall temperatures, demonstrating how gradient temperature profiles and optimized airflows can reduce particle density and improve

uniformity. By employing a two-way coupling approach, the model accurately predicted particle expansion and heat transfer phenomena, providing insights into improving energy efficiency and product quality in industrial-scale electric furnaces. Figure 1.12 shows a thermal image of the bottom part of the furnace, where the intensive temperature gradation demonstrates the importance of optimizing thermal profiles to achieve uniform particle expansion and energy efficiency.

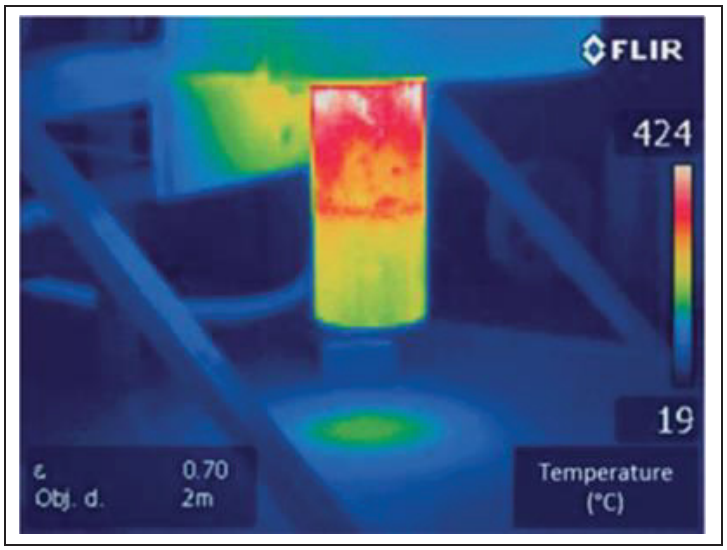

Figure 1.12 Thermal gradients in the bottom section of a vertical electric furnace
Taken from Angelopoulos et al. (2024, p. 317)

Tan et al. (Tan, Yu, & Abdullah, 2022) conducted a 3D CFD simulation of a vertical multi-wafer electric furnace for the annealing process, analyzing thermal uniformity across stacked wafers. The study highlighted significant heat losses through the top header and process door, with temperatures at the top wafers found to be 3–5% lower than the heater temperature. Design recommendations, including a full boat cover and enhanced insulation, achieved up to 28% and 22% reductions in heat dissipation, improving energy efficiency and product quality. The infrared thermal imaging in Figure 1.13 highlights hot spots during the annealing process, emphasizing areas where insulation improvements were targeted to enhance energy efficiency and reduce heat losses.

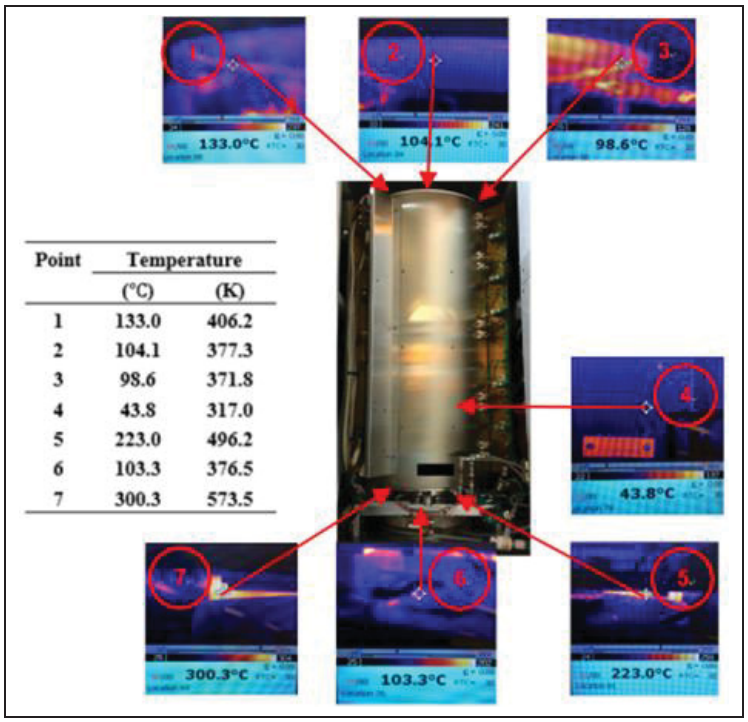

Point	Temperature	
	(°C)	(K)
1	133.0	406.2
2	104.1	377.3
3	98.6	371.8
4	43.8	317.0
5	223.0	496.2
6	103.3	376.5
7	300.3	573.5

Figure 1.13 Infrared imaging of hot spots in a multi-wafer electric furnace
Taken from Tan et al. (2022, p. 3146)

Smolka et al. (Smolka, Nowak, & Rybarz, 2010) performed a 3D CFD simulation of a laboratory-scale drying oven with ~0.25 m^3 chamber volume to analyze and optimize temperature uniformity. By adjusting heater placement, fan speed, and baffle design, they reduced temperature non-uniformity and improved heating efficiency. Experimental validation of the modified prototype confirmed the simulation's accuracy, showcasing practical improvements for small-scale drying applications. Figure 1.14 presents temperature field distributions inside the drying oven, with cross-sectional views illustrating areas of initial temperature non-uniformity and sensor placements used for validation.

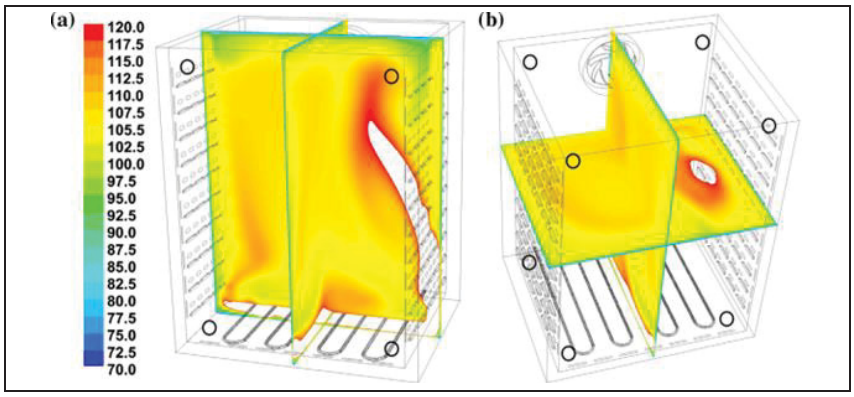

Figure 1.14 Temperature distribution and sensor locations in a laboratory drying oven
Taken from Smolka et al. (2010, p. 379)

Fu et al. (Fu, Yu, Shang, Wang, & Zhang, 2019) developed a CFD model using FLUENT to simulate heat transfer processes in a chamber electric resistance furnace for superalloy heating. The study integrated conjugate heat transfer mechanisms, including natural convection, surface radiation, and transient heat conduction, with a PID control system regulating resistance wire power. The validated model accurately captured temperature distribution and equilibration times, offering insights into optimizing heating schemes for precise temperature control in industrial applications. Figure 1.15 and Figure 1.16 illustrate the geometry of the resistance furnace and the initial temperature profile during heating with a load, respectively, highlighting the challenges of managing thermal gradients and achieving uniform heat distribution.

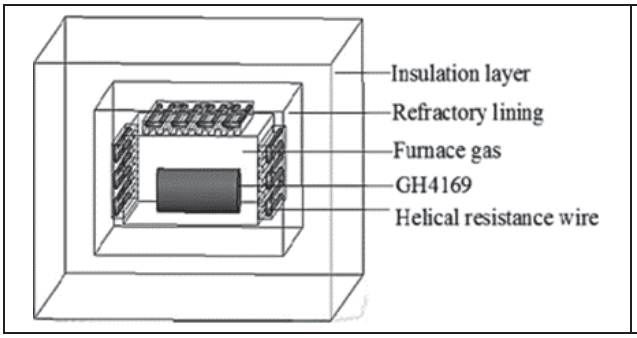

Figure 1.15 Geometry of a chamber electric resistance furnace
Taken from Fu et al. (2019, p. 683)

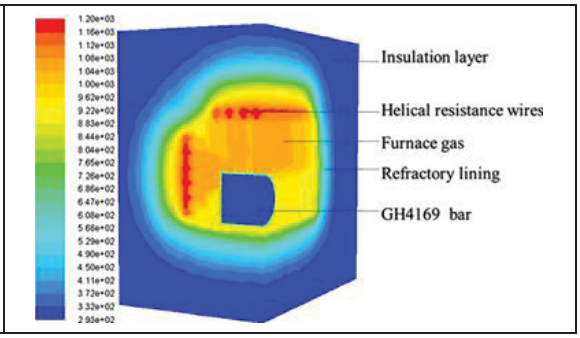

Figure 1.16 Temperature field in a loaded resistance furnace
Taken from Fu et al. (2019, p. 685)

Palacio-Caro et al. (Palacio-Caro, Alvarado-Torres, & Cardona-Sepúlveda, 2020) investigated a pit-type electric furnace with ~0.34 m^3 chamber volume using CFD to analyze the effects of fan speeds on temperature homogeneity and thermal efficiency. The study reported increasing fan speed improved temperature uniformity due to enhanced recirculation but decreased thermal efficiency as fan energy demand rose. For instance, doubling the fan speed reduced tempering time by 50% but lowered thermal efficiency by 20%. The findings offer actionable design insights for balancing energy efficiency with process performance in industrial electric furnaces. Figure 1.17 provides an isometric view and a cut view of the studied furnace, highlighting fan placement and airflow paths critical to the CFD analysis of airflow dynamics and thermal uniformity.

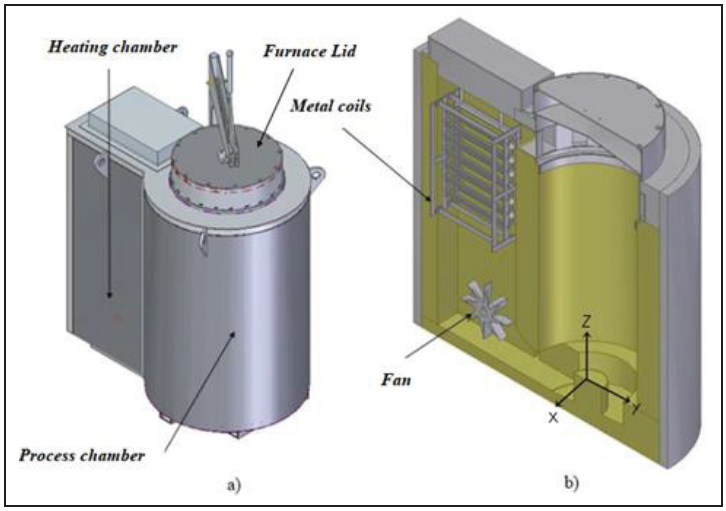

Figure 1.17 Pit-type electrical tempering furnace
Taken from Palacio-Caro et al. (2020, p. 3)

Despite the value of these studies, most CFD simulations of electric furnaces have been limited to laboratory or small-scale systems. They often simplify the geometry, neglect multi-block loading effects, or assume idealized thermal boundaries. This restricts their applicability to large-scale industrial settings, where thermal inertia, heat losses, and coupled physical interactions introduce far more complexity and computational cost. A clear need remains for validated CFD models that can scale up to industrial electric furnaces treating massive steel forgings under realistic process constraints.

1.4.3 Role of CFD in Multi-Block Loading Configurations

The optimization of loading patterns in multi-block configurations is a critical area where CFD offers unparalleled insights. When multiple forgings or components are placed within the same furnace, complex thermal interactions arise, such as shadowing, block-to-block radiation, airflow bypass, and non-uniform heat absorption. These phenomena are challenging to capture experimentally, particularly in large industrial setups.

Bohlooli Arkhazloo (Bohlooli Arkhazloo, 2020) investigated the impact of loading patterns on temperature uniformity and residence time in gas-fired furnaces using 3D transient CFD simulations. Their study revealed that improper loading configurations led to significant temperature non-uniformities, while optimized patterns reduced non-uniformity by 32% and residence time by 15.5%. This highlights the potential of CFD to identify configurations that enhance both efficiency and uniformity in large-scale operations. Figure 1.18 demonstrates temperature contours for different loading configurations, showcasing improvements achieved with optimized designs.

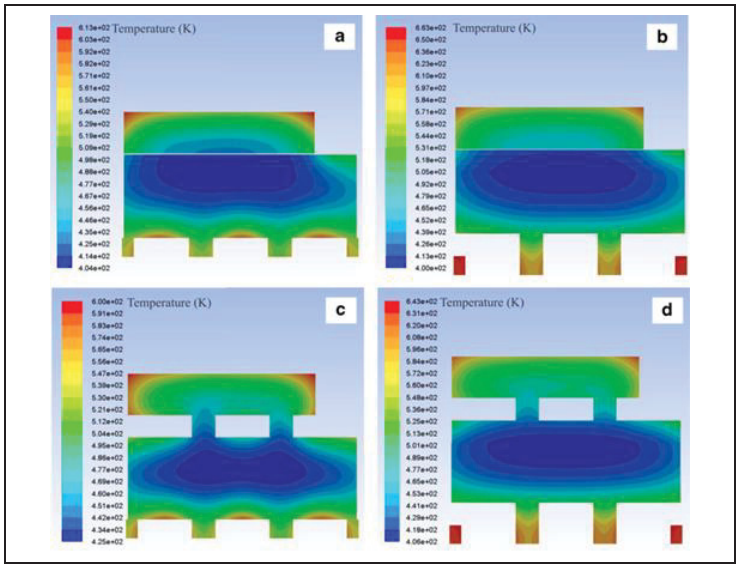

Figure 1.18 Temperature contours for optimized and non-optimized loading configurations
Taken from Bohlooli Arkhazloo (2020, p. 111)

Xu et al. (2016) (Xu, Su, Xu, & Liu, 2016) extended the CFD approach to study vacuum heat treatment furnaces for Ni-based turbine blades, focusing on the effects of shielding and part arrangement on thermal uniformity during heating and quenching. The study found that inadequate part placement led to uneven cooling and reduced process efficiency. Their CFD analysis highlighted how blade geometry and mutual shielding significantly influence temperature uniformity, particularly in multi-layer configurations. Figure 1.19 illustrates the simulated temperature distribution for turbine blades arranged in a single layer during heating and quenching, showcasing the critical impact of part positioning on thermal uniformity.

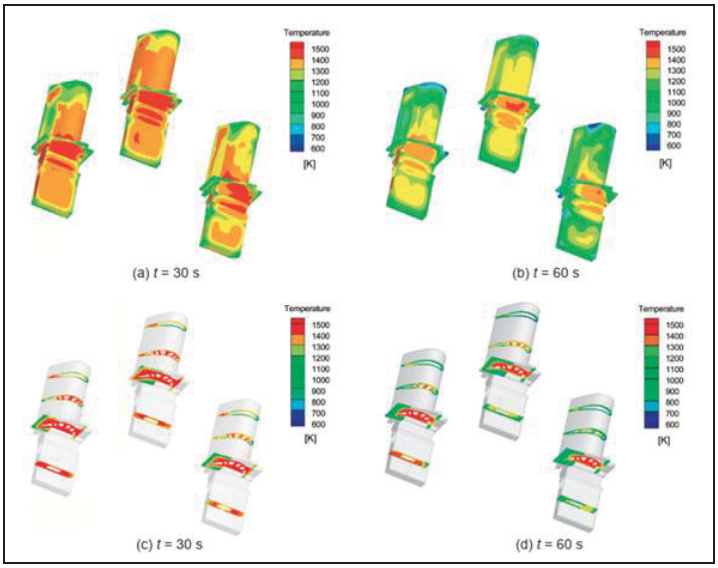

Figure 1.19 Temperature distribution of multiple blades in one layer at different times
Taken from Xu et al. (2016, p. 411)

The above studies provide illustrative examples of the critical role of CFD in optimizing furnace loading configurations across different furnace types. While Bohlooli-Arkhazloo et al. (Bohlooli Arkhazloo, 2020) addressed large steel forgings in gas-fired furnaces, Xu et al. (Xu et al., 2016) explored vacuum heat treatment, highlighting CFD's versatility in tackling complex thermal phenomena. Both works point to gaps in scaling up simulations for more intricate geometries and longer processes, highlighting areas where further research is still needed to support industrial applications.

1.5 Machine Learning for Predictive Modeling and Decision Support

Machine learning (ML) methods are increasingly applied in manufacturing to analyze complex, high-dimensional data and support data-driven decision-making (Bishop & Nasrabadi, 2006; Hastie, Tibshirani, Friedman, & Friedman, 2009). In heat treatment operations, ML offers a complementary approach to first-principles models such as CFD, especially when rapid predictions or large-scale data analysis is required. By learning patterns from historical furnace data, ML models can estimate outcomes such as material response, process duration, and optimal operating parameters without relying on explicit physical equations. A growing number of studies (Carlsson, 2021) have applied ML in steel-related manufacturing tasks, including property prediction, defect classification, and energy use estimation. However, most of these works focus either on material-level phenomena or early-stage processing steps like rolling and casting. The application of ML in furnace-level operations, particularly in the tempering of large forgings, remains limited and fragmented. Moreover, many existing models are developed under laboratory conditions (small-size samples) or small datasets (often <1000 samples), limiting their generalizability to real-world industrial cases. The following subsections review ML applications in steel production and heat treatment, focusing on their scope, limitations, and relevance to industrial furnace modeling.

1.5.1 Applications in Steel Manufacturing

Machine learning techniques have gained traction across various stages of steel manufacturing, driven by the increasing availability of process data and the demand for predictive capabilities. Several studies have explored ML for property prediction (e.g., hardness, tensile strength), defect classification, energy forecasting, and process control, particularly during casting, rolling, and forming. For example, Cui et al. (Cui et al., 2023) integrated metallurgical features—such as dislocation density and TiC precipitate size—into an ANN model to predict tensile strength and yield strength of Ti micro-alloyed steels. The hybrid approach improved R^2 from 0.82 to 0.94 versus a purely data-driven model, demonstrating that embedding physical

descriptors enhances ML reliability in modeling complex thermo-mechanical steel processes. Similarly, Adhikary (Adhikary, 2021) developed and compared five regression models to predict the ultimate tensile strength (UTS) of low-alloy steels based on chemical composition and process temperature. Among them, Random Forest and XGBoost achieved R^2 scores of 98.63% and 98.61%, respectively, confirming the potential of ML for rapid, data-driven material certification. This highlights how accurate mechanical property estimation can bypass costly physical testing when trained on representative industrial datasets. In the same direction, Chen et al. (J. X. Chen, Zhao, Sun, Zhang, & Yin, 2019) developed an XGBoost model trained on 17,710 industrial samples to predict tensile strength, compressive strength, and elongation. Achieving R^2 values of 0.96-0.99 the study emphasized the importance of temperature parameters and nitrogen content while addressing input coupling issues, highlighting the value of large datasets and feature influence analysis in steel property prediction. Likewise, Choi (Choi, 2019) used XGBoost and statistical inference to predict fatigue strength from 25 compositional and processing features, achieving R^2=0.98. While the ML model outperformed traditional regressions, the study revealed that linear models poorly captured complex interdependencies, reinforcing the need for robust ensemble methods. In terms of quality control, Takalo-Mattila et al. (Takalo-Mattila, Heiskanen, Kyllonen, Maatta, & Bogdanoff, 2022) developed a LightGBM-based binary classifier trained on 89 real-time features from over 225,000 steel slabs, achieving an AUC of 0.81 and Matthews Correlation Coefficient (MCC) of 0.27 on test data. Integrated into a Quality Monitoring Tool (QMT), this model enabled the identification of over 50% of defective slabs by inspecting only 10%, significantly optimizing inspection resource allocation. Figure 1.20 presents the real-time data flow embedded in the QMT environment, enabling actionable insights for process operators. Similarly, Ji et al. (Y. Ji, Wang, Zhou, Zhong, & Si, 2024) applied an XGBoost-based classifier to detect slag entrapment in continuous casting, training it on 15,988 real-world slabs. The model, enhanced via Bayesian Optimization (BO), reached an AUC of 0.811 and an accuracy of 75.6%, outperforming PSO and GA variants. However, despite the solid performance, the study focused only on classification and offered no predictive timeline or recommendations for actionable process changes. Figure 1.21 shows the model's workflow, from data preparation to feature interpretation.

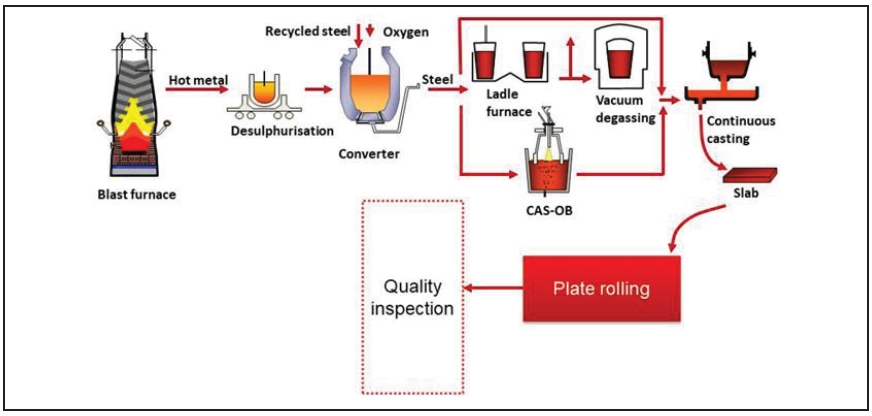

Figure 1.20 Simplified steel production process
Taken from Takalo-Mattila et al. (2022, p. 68100)

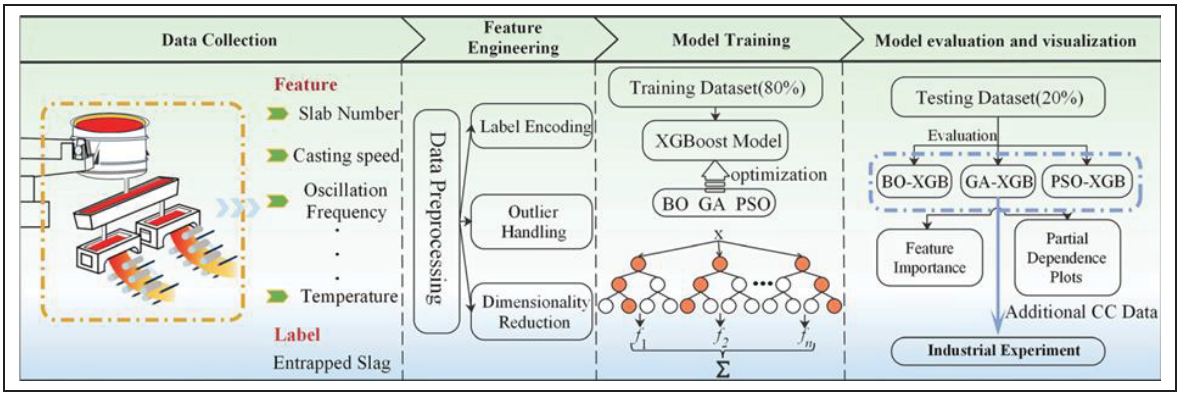

Figure 1.21 Workflow for developing and optimizing XGBoost model
Taken from Y. Ji et al. (2024, p. 2029)

Meanwhile, Mamun et al. (Mamun, Wenzlick, Sathanur, Hawk, & Devanathan, 2021) demonstrated that machine learning models can not only outperform traditional parametric methods but also offer interpretable insights for alloy design. They used XGBoost to predict the creep rupture life of 9–12% Cr and austenitic steels, achieving Pearson coefficients above 0.9 and 0.8, respectively. Shapley's analysis highlighted stress and creep rate as dominant features, while Cu and S acted as proxies for inclusions. A variational autoencoder (VAE) was tested for synthetic data generation but showed limited improvement due to rare-event distribution. In a related area, Wang and Lu (Q. K. Wang & Lu, 2024) developed a stacking ensemble model to predict residual strength in corroded pipelines using 453 data points. By

integrating passthrough strategies and diverse base/meta learners, they achieved an R^2 of 0.959. However, the model underperformed for low-strength samples, reflecting limitations in minority class representation. Their error analysis revealed high sensitivity to feature imbalances and highlighted the benefit of base learner diversity in mitigating overfitting and enhancing generalization. These investigations highlight critical aspects of ML applications in steel manufacturing—from feature importance and data imbalance to model generalization and physical interpretability— that reflect core methodological and operational issues further explored in this thesis.

1.5.2 Machine Learning in Furnace Operations

Specific to furnace operations, ML has rarely been applied to optimize heat treatment cycles or loading strategies in industrial settings, especially in electric and gas-fired furnaces. Nevertheless, existing studies demonstrate ML's capacity to support control of key operational variables such as temperature regulation, energy use, and defect mitigation. Zhou et al. (Zhou, Wang, Deng, Yao, & Liu, 2021) investigated the application of XGBoost and LightGBM algorithms for predicting the endpoint temperature of molten steel in a VD furnace—a critical control point in vacuum refining. The study used 33,031 real industrial records from Baosteel over seven years. After data preprocessing via Tukey's test and Box-Cox normalization, Random Forest-based selection reduced the features to eight critical variables. The ensemble models achieved 89.86% accuracy within ±10°C, demonstrating the potential of ensemble learning methods for tackling temperature control challenges in industrial furnaces and representing a direction of growing interest in operational optimization research.

Manojlović et al. (Manojlović, Kamberović, Korać, & Dotlić, 2022) employed machine learning to optimize energy efficiency in electric arc furnaces (EAF), addressing the complexities of nonlinear processes such as scrap melting and refining. By adopting a data-centric approach, the study emphasized extensive data cleaning and feature selection to improve model performance. Key targets included electricity consumption, operating time, and steel yield, analyzed using XGBoost, ANN, Random Forest, and SVM models. Among these,

ANN showed the greatest flexibility when switching targets, while XGBoost demonstrated high predictive accuracy. SHAP and PDP analyses revealed the impact of process parameters on energy consumption and yield. The findings highlight the significance of precise parameter control and robust data quality for enhancing process efficiency. Figure 1.22 illustrates the workflow for developing these models, showcasing the integration of data preprocessing, feature selection, and hyperparameter optimization to achieve reliable predictions. This work illustrates how precise parameter modeling can complement operational knowledge to support process improvements in industrial furnace operations.

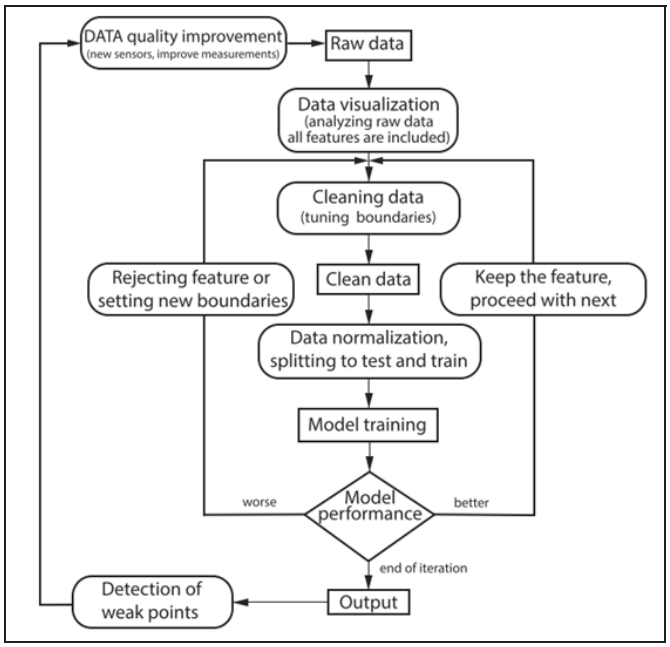

Figure 1.22 Data-centric workflow for machine learning-based optimization EAF
Taken from Manojlović et al. (2022, p. 3)

Chen et al. (C. Chen, Wang, Chen, & Yan, 2022) developed a heterogeneous ensemble framework to predict liquid steel temperature in ladle furnace (LF) refining. The study integrated tree-based ensemble models, including XGBoost, and introduced Recursive Feature Increase (RFI) and Recursive Search Optimization (RSO) for feature selection and hyperparameter tuning. Using industrial data from 828 production heats, the model achieved

6.9% lower MSE, with $R^2 = 0.574$, offering improved thermal control precision despite moderate predictive strength.

These studies collectively demonstrate ML's potential to support furnace operations through interpretable models, real-time predictions, and multivariable process evaluations. Their focus on thermal endpoints, energy yield, and operational tuning provides a basis for extending ML use to electric heat treatment furnaces. One promising direction is the use of ML in furnace scheduling and multi-block loading strategies, where predictive models could integrate historical data—block size, alloy type, and mechanical targets—to suggest optimized cycle parameters. By automatically flagging suboptimal arrangements, it will be possible to reduce thermal gradients, improve temperature uniformity, and enhance overall throughput. Such integration would bridge the gap between human expertise and data-driven methods, leading to more consistent results and greater energy efficiency.

1.5.3 Limitations and Opportunities

The reviewed studies demonstrate notable progress in applying machine learning to steel manufacturing and furnace operations. However, several persistent limitations highlight opportunities for advancing the field:

1. **Data Resolution and Operational Diversity:** While many studies, such as those by (Cui et al., 2023) and (C. Chen et al., 2022), leveraged large datasets, they often focused on controlled scenarios or narrowly defined material compositions. Variations in block sizes, multi-step heating cycles, and loading sequences were not included, limiting model generalizability to diverse production settings.
2. **Underrepresentation of Loading and Scheduling Contexts:** Most ML applications focus on isolated parameters, such as tensile strength or energy consumption. Few incorporate the structural and spatial arrangement of materials inside the furnace, a critical factor affecting heat treatment uniformity. This limits their utility in addressing high-mass, multi-block scenarios typical of industrial tempering operations.

3. **Model Interpretability and Feature Transparency:** Although SHAP and PDP analyses have been adopted in recent works e.g., (Mamun et al., 2021; Manojlović et al., 2022) many predictive models remain difficult to interpret, particularly in relation to metallurgical phenomena or thermal behavior. This reduces trust among plant operators and engineers, especially when recommendations contradict physical expectations.
4. **Gap Between Predictive Accuracy and Operational Utility:** Some high-performing models, such as those developed by (Y. Ji et al., 2024) and (Q. K. Wang & Lu, 2024), focus on optimizing numerical accuracy (e.g., AUC, R^2), but offer limited guidance for process adjustments or decision-making. These models often lack mechanisms to account for competing objectives, such as energy reduction versus processing time, or temperature uniformity versus throughput.
5. **Limited Focus on Real-Time Integration and Deployment:** Despite advances in model training and validation, relatively few studies explore the challenges of deploying ML tools within actual plant environments. Issues such as data synchronization, sensor drift, latency, and integration with existing control systems remain underexplored.

These limitations, observed across multiple studies, suggest that future ML developments must move beyond pure predictive modeling to address practical constraints, process complexity, and interpretability demands in industrial furnace operations. By learning from these gaps, emerging scientific approaches can better align with operational needs—providing actionable, trustworthy insights that complement traditional engineering expertise.

1.6 Overview of Current Research

The current body of literature reveals meaningful progress in the application of computational methods for improving heat treatment processes. CFD-based investigations have provided insights into temperature uniformity, thermal gradients, and airflow dynamics, particularly in gas-fired and lab-scale electric furnaces. Meanwhile, recent studies in machine learning have

demonstrated predictive capabilities for material properties, energy consumption, and operational parameters across steel manufacturing stages. However, the literature remains fragmented in terms of its applicability to full-scale industrial electric furnaces, especially regarding multi-block loading conditions, high thermal inertia, and data-driven operational decision-making.

1.6.1 Identified Research Gaps

1.6.1.1 Limited Studies on Industrial Electric Furnaces

While several CFD studies have explored gas-fired and small-scale furnace operations, large industrial electric furnaces—characterized by complex geometries and long-duration heating cycles—are less commonly addressed. This limits the transferability of simulation insights to real-world scenarios, particularly for tempering large forgings under variable load and temperature conditions.

1.6.1.2 Incomplete Understanding of Multi-Block Loading Effects

Stacking configuration and loading patterns have significant influences on heat distribution and final material quality. Yet, most current studies simplify these aspects or treat them heuristically. The lack of detailed investigations into radiative interference, conduction bottlenecks, and geometric shadowing leads to suboptimal practices in industrial operations.

1.6.1.3 Absence of CFD-Driven Design Optimization

Although multi-objective optimization methods and CFD simulations have individually matured, their integrated use for furnace design refinement remains scarce. Challenges such as simulation time, large design space dimensionality, and convergence stability have limited the adoption of fully coupled frameworks for furnace optimization.

1.6.1.4 Underutilized ML Potential in Loading Cycle Planning

Despite the growing use of ML for material property prediction and defect detection, its integration into furnace operation—especially for loading strategy recommendations—remains limited. There is insufficient work addressing how historical furnace logs, block geometry, and cycle parameters can be translated into robust decision-support systems. This gap restricts the deployment of intelligent guidance tools for operators dealing with high-throughput, thermally sensitive operations.

1.6.2 Research Objectives

Based on the limitations identified, this PhD research addresses the following objectives:

- **CFD Simulation of Industrial Electric Furnaces:** To model thermal dynamics and assess design improvements for industrial-scale furnaces. The focus is on long-duration tempering cycles, with realistic geometries and boundary conditions reflecting operational constraints.
- **Analysis of Multi-Block Loading and Heat Transfer Behavior:** To quantify the thermal effects of different stacking patterns and evaluate strategies for reducing temperature gradients and ensuring uniformity across large steel components.
- **Coupling CFD with Optimization Methods:** To implement optimization algorithms (e.g., Pareto-based search) that refine furnace layout and operating parameters for improved energy efficiency and product consistency.
- **Development of ML-Based Predictive Models for Cycle Planning:** To construct data-driven tools that assist in determining optimal loading configurations using historical records, production parameters, and surrogate relationships learned from industrial data.

By pursuing these goals, the study aims to bridge the gap between simulation, prediction, and operational implementation. The combination of CFD and ML methods provides a practical and scientifically grounded framework for enhancing performance, sustainability, and reliability in industrial electric furnace operations.

CHAPTER 2

METHODOLOGY

2.1 Introduction to the Overall Methodological Framework

The overarching goal of this research is to improve the efficiency and uniformity of industrial electrical heat treatment furnaces through an integrated approach encompassing (1) experimental measurements in a full-scale industrial furnace, (2) computational fluid dynamics (CFD) modeling for thermal and flow simulations, (3) multi-objective optimization to refine stacking patterns and heating element layouts, and (4) machine-learning–based analysis of operational data to predict optimal loading cycles. Throughout this study, three major research directions were pursued:

- **Stacking/Loading Pattern Analysis:** In the initial phase, the research focused on how spacers and skids influence temperature uniformity across large forging blocks. A validated transient CFD model of a 112-m³ industrial electric furnace was employed to simulate heat transfer and airflow dynamics under various loading configurations. The experimental validation used embedded thermocouples to measure temperature profiles. This phase, detailed in Chapter 3, demonstrated how spacer sizes and skid arrangements impact convective heat circulation and block heating history.
- **Heating Elements Layout Optimization:** The second phase emphasized optimizing the placement of heating elements. By employing CFD coupled with multi-objective evolutionary algorithms (e.g., genetic algorithms and Pareto-based approaches), the study explored how various configurations of wall and ceiling-mounted heating elements influence furnace temperature uniformity. Results, presented in Chapter 4, reveal how optimized heating element layouts reduce internal and surface temperature gradients, thereby enhancing mechanical property consistency in large-size steel forgings.
- **Machine Learning–Based Predictive Model:** The final phase adopted a data-driven methodology to complement the CFD analysis. Using a dataset of over 1,100 industrial tempering logs, a tree-based XGBoost regressor model was trained to predict ideal loading

cycle parameters, including total weight and length per load. This predictive model, discussed in Chapter 5, enables real-time guidance for furnace operators, enhancing decision-making efficiency.

This thesis integrates the above three research threads into a unified methodological framework. Experimental data provides critical validation for CFD simulations, while machine learning leverages both historical operational data and insights from the simulations. This synergy between thermal/fluid models and data-driven techniques establishes a robust foundation for achieving consistent product quality and reducing operational costs in industrial electric heat treatment furnaces.

2.2 Experimental Methods and Data Acquisition

2.2.1 Description of the Electrical Furnace(s) and Instrumentation

All experimental measurements were conducted on an industrial car-bottom electrical furnace located at Finkl Steel (Sorel, Quebec, Canada). The furnace features:

- A 112-m^3 heating chamber with inner dimensions of approximately 3.43 m × 4.11 m × 8.02 m.
- Electrical heating elements are installed along sidewalls, operating without exhaust systems to minimize heat loss.
- Three axial fans are mounted on the ceiling, each rotating at 1,750 rpm, to ensure air recirculation within the furnace.
- Ceramic-fiber insulation of 0.254 m thickness with thermal conductivity of approximately 0.16 W/m·K at 538 °C, reducing energy loss.

Figure 2.1 provides a schematic illustration of the furnace structure, highlighting the car-bottom design, fans placement, and the arrangement of heating elements. The furnace's heating elements collectively provide a nominal power of 1,710 kW, with real-time power monitoring at 600 V/60 Hz.

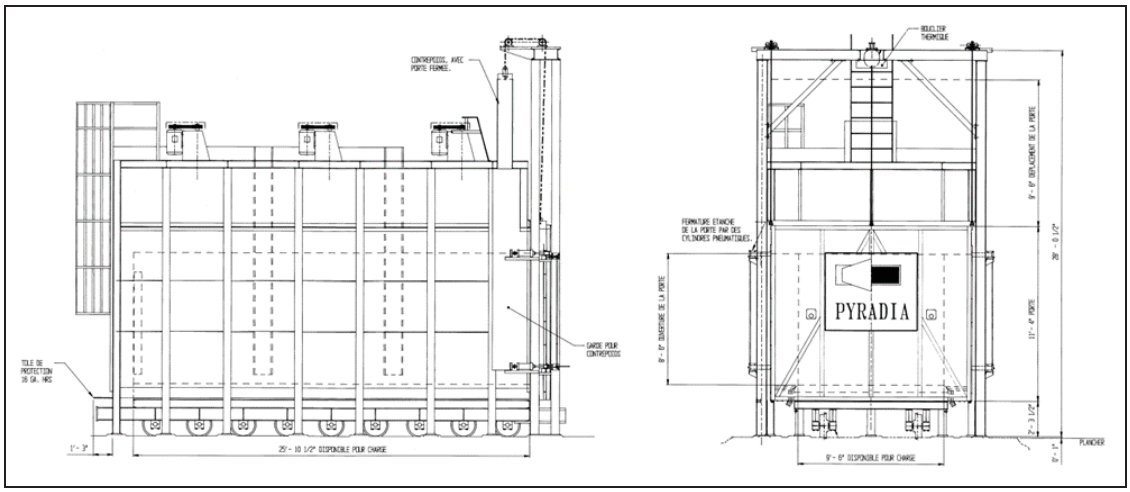

Figure 2.1 Schematic of the industrial furnace showing the car-bottom, fan placement, and heating elements

The experimental loading configuration included two large forging blocks, each weighing approximately 29 metric tons, stacked with spacers in between (as depicted in Figure 2.2). These spacers were used to replicate common industrial practices and allow for airflow circulation between blocks. Thermocouples (TCs) were installed on key surfaces to measure transient temperature profiles throughout the tempering process.

Figure 2.2 Experimental setup showing stacked forging blocks with spacers in the furnace

2.2.2 Thermocouple Placement and Calibration

Given the high operating temperatures (up to 600°C), each thermocouple was encased in a ceramic insulator before installation. TCs were labeled systematically (e.g., T1, T2) and positioned to capture:

- Edge or corner temperatures, where heat transfer is most intense due to convection and radiation.
- Center-line positions, to assess uniformity under steady-state conditions.
- Contact interfaces in stacked configurations, to identify potential cold spots beneath skids or spacers.

To maintain consistency, each thermocouple was calibrated against a known reference temperature using an ice-water (0 °C) and a secondary elevated calibration point prior to installation. This calibration procedure adhered to ISO/IEC (Automation, 1982) or internal industrial calibration standards to keep the measurement error below ±3 °C in the critical 400–600 °C range, which is typically sufficient for accurate CFD validation. Figure 2.3 shows a close-up photograph of a typical thermocouple installation on the forging surface, illustrating the shallow drilled hole and protective ceramic sleeve used to ensure accurate temperature measurement.

Figure 2.3 Close-up of thermocouple installation on a forging block

2.2.3 Measured Variables

Data collection focused on the following key variables:

- **Surface Temperatures:** Monitored continuously via thermocouples throughout the tempering cycle, capturing transient profiles for use in both experimental validation and thermal analysis.
- **Furnace Power Usage:** Real-time kWh consumption was recorded at 10-second intervals, creating transient power profiles critical for defining boundary conditions in CFD simulations (see Chapter 4).
- **Forging Dimensions and Mass:** Measurements of forging block length, width, thickness, and total mass were systematically recorded. These parameters served as essential inputs for 3D CAD modeling in CFD simulations (Chapters 3 and Chapter 4) and as key features for machine-learning predictive models (Chapter 5).
- **Forging Material Chemical Composition:** The chemical composition of the forging materials, as presented in Table 4.1 of Chapter 4, was meticulously documented. These compositions informed the calculation of critical material properties—such as thermal conductivity, specific heat capacity, and density—used in CFD simulations to accurately represent heat transfer behaviors in the forging blocks.
- **Internal Furnace Temperatures:** Six additional thermocouples, strategically located near the side walls and fans, provided average hot-air temperature measurements. These readings ensured the calibration of furnace operation under unloaded conditions and were also utilized to validate the CFD models.

2.2.4 Data Recording, Validation, and Preprocessing

The raw measurement data—including time, temperature, and operational parameters—were automatically logged onto a computer system and archived in organized datasheets. Over a nine-month data collection period, this process yielded more than 100 furnace runs, encompassing 1,162 forgings. The primary data validation and preprocessing steps were:

- **Filtering Out Incomplete Runs:** Furnace runs that were aborted prematurely or had missing thermocouple channels were flagged and excluded from the final dataset used for calibration and validation.
- **Spot-Checking Outliers:** Any unusually high or low temperature readings (e.g., T > 600°C) were carefully reviewed. Confirmed valid readings, such as those resulting from atypical operational conditions, were retained. Data points identified as sensor malfunctions or electronic glitches were either corrected or removed to maintain dataset integrity.
- **Historical Data Aggregation:** For the machine-learning model development (see Chapter 5), data from 1,162 forging blocks across multiple tempering cycles were consolidated into a single dataset. This dataset included columns for critical variables such as block dimensions (height, width, thickness), temperature setpoints, holding durations, material types, block shapes, and total loads. Further preprocessing, such as scaling and transformation (Kuhn & Johnson, 2013), ensured the dataset's compatibility with machine-learning algorithms.

By systematically collecting, validating, and processing this data, a robust experimental dataset was established. This dataset played a dual role in the research, enabling high-fidelity CFD simulations (Chapters 3 and 4) and supporting the development of advanced machine-learning predictive tools (Chapter 5).

2.3 CFD Modeling and Simulation

The present work implements CFD as an integral methodology to investigate and optimize the heat treatment of large steel forgings in a 112 m^3 industrial electric furnace. A holistic modeling strategy was adopted to capture the coupled fluid flow, heat transfer (by convection, conduction, and radiation), and temperature evolution both within the furnace chamber and inside the forging blocks. The following subsections provide an overview of the governing equations, turbulence models, radiation treatment, CAD-based geometry creation and meshing procedures, transient simulation setups, and validation against experimental data. By

integrating these elements, the CFD framework ensures a high-fidelity representation of the physical phenomena encountered under industrial operating conditions.

2.3.1 Governing Equations

A pressure-based finite volume solver (ANSYS Fluent) was utilized to solve the governing conservation equations of mass, momentum, and energy in the fluid domain (ANSYS Inc., 2023). In parallel, a conjugate heat transfer approach was applied to resolve the transient conduction inside the solid forging blocks (Versteeg & Malalasekera, 2007). This two-domain strategy (fluid and solid) allows for a realistic simulation of the heat exchange at the fluid-solid interface (ANSYS Inc., 2023):

Mass conservation (Continuity):

$$\frac{\partial \rho}{\partial t} + \nabla.(\rho v) = 0 \tag{2.1}$$

Where ρ is the density, and v is the velocity vector. Density variations due to temperature gradients in the furnace are handled via the ideal gas law (see below) (ANSYS Inc., 2023).

Momentum conservation (Navier–Stokes):

$$\frac{\partial(\rho v)}{\partial t} + \nabla.\rho vv = -\nabla p + \rho g + \nabla.\tau \tag{2.2}$$

Where p is pressure, g is gravitational acceleration, and τ represents the viscous stress tensor This governs fluid motion, accounting for buoyancy, viscous forces, and pressure gradients—all of which can significantly affect recirculating flows in the furnace (ANSYS Inc., 2023). Equation (2.2) is written in its standard instantaneous form; in the present study, turbulence effects are later incorporated through the Reynolds-averaged approach with k–ε closure (Section 2.3.2)

Energy conservation:

$$\frac{\partial}{\partial t}(\rho e) + \nabla.(v(\rho e + p)) = \nabla.(k\nabla T) + S \tag{2.3}$$

Where e is the total energy per unit mass, k is thermal conductivity, T is temperature, and S represents heat sources such as radiative heat flux or energy generated by user-defined heating elements. Equation (2.3) is critical for modeling thermal dynamics in both the furnace and forging blocks. Similar to momentum, turbulence contributions to energy transport are modeled through the chosen closure scheme introduced in Section 2.3.2.

Conduction in the forging blocks (solid domain):

$$\rho_s c_{p,s} \frac{\partial T_s}{\partial t} = \nabla.(k_s \nabla T_s) \tag{2.4}$$

where ρ_s , $c_{p,s}$, and k_s are the density, specific heat, and thermal conductivity of the forging material, respectively, and T_s is the local temperature in the solid. The solid and fluid domains are fully coupled at the block surfaces through conjugate heat transfer boundary conditions, ensuring continuous heat flux and temperature continuity across the interface (ANSYS Inc., 2023; Incropera, DeWitt, Bergman, & Lavine, 1996).

Ideal Gas Law:

For the present furnace, the working fluid is ambient air at ~1 atm and temperatures that do not exceed ≈ 600 °C (≈ 873 K). Standard property tables compiled from compressibility-factor measurements show that, under these conditions, air behaves almost ideally: the compressibility factor $Z = pv/RT$ remains within 0.98 – 1.02 for 300 K ≤ T ≤ 900 K at 1 atm (Frank Kreith, 2010; Incropera et al., 1996). Because the resulting density deviation of < 2 % is smaller than typical numerical uncertainty, density was evaluated with the ideal-gas relation:

$$\rho = \frac{\mathrm{p}}{RT} \tag{2.5}$$

Which captures buoyancy-driven gradients while avoiding the overhead of real-gas corrections. Within this temperature/pressure envelope, such corrections were therefore judged unnecessary. This relationship was applied directly within the governing equations:

- In the continuity equation (2.1), density variations ($\partial\rho/\partial t$) capture thermal expansion.
- In the momentum equation (2.2), buoyancy forces (ρg) are modeled accurately.
- In the energy equation (2.3), density-dependent changes in total energy (e) establish thermal-fluid coupling.

2.3.2 Turbulence Modeling and Multiple Reference Frames

Turbulence Modeling:

The selection of the turbulence closure was guided by the expected flow regime inside the partner's furnace. A fan tip speed of 67 m s^{-1} and a characteristic chamber height of ~ 4 m yield a hydraulic Reynolds number Re ~ 1.2×10^6 at 530 °C, confirming fully turbulent, swirl-dominated recirculation. Under comparable Reynolds numbers and temperature levels, the realizable k–ε formulation has been reported to reproduce mean velocity, k, and temperature fields in electric and gas-fired furnaces ranging from laboratory scale (<1 m^3) to industrial scale (>100 m^3) with acceptable accuracy while keeping computational cost moderate (Bohlooli Arkhazloo, 2020; Palacio-Caro et al., 2020; Smolka et al., 2010). Accordingly, the realizable k–ε model was adopted for the present simulations. This model solves two transport equations for turbulence kinetic energy (k) and its dissipation rate (ε):

$$\frac{\partial(\rho k)}{\partial t} + \nabla.(\rho k v) = P_k + \rho\varepsilon + \nabla.\left[(\mu + \frac{\mu_t}{\sigma_k})\nabla\mathrm{k}\right] \tag{2.6}$$

$$\frac{\partial(\rho\varepsilon)}{\partial t} + \nabla.(\rho\varepsilon v) = C_1\frac{\varepsilon}{k}P_k + C_2\rho\frac{\varepsilon^2}{k} + \nabla.\left[(\mu + \frac{\mu_t}{\sigma_\varepsilon})\nabla\varepsilon\right] \tag{2.7}$$

Where k is the turbulence kinetic energy (m^2/s^2), representing the energy contained in turbulent eddies; ε is the turbulence dissipation rate (m^2/s^3), indicating the rate at which turbulence

kinetic energy dissipates into heat; P_k is the production term for turbulence kinetic energy (kg/(m·s³)), representing the energy transfer from mean flow to turbulence; μ_t is the turbulent viscosity (Pa·s), given by $\mu_t = \rho C_\mu \frac{k^2}{\varepsilon}$, and σ_k and $\sigma_\varepsilon$the turbulent Prandtl numbers controlling the diffusion rates of k and ε, respectively. C_1 and $C_2$are model-specific constants empirically derived for stability and accuracy in predictions (Wilcox, 1998). Key reasons for selecting this model include (Versteeg & Malalasekera, 2007):

- **Swirl Prediction:** Its realizability constraints improved predictions of swirl and vortex generation caused by the axial fans.
- **Cost Efficiency:** It offers a good balance between accuracy and run-time (computational cost) for large-scale, transient simulations.
- **Industrial Validation:** Previous studies in furnace applications have demonstrated its effectiveness in capturing thermal stratification and recirculating flows.

Near-Wall Treatment:

Near-wall zones were modeled with the scalable wall function, which bridges the viscous sub-layer and the logarithmic region. Consequently, meshes were locally refined so that the dimensionless wall distance y^+ remained in the 30 – 300 range recommended for the realizable k–ε model. This strategy eliminates the need for the very fine prism layers required by low-Reynolds-number SST k–ω or by the enhanced-wall-treatment version of the standard k–ε model, both of which would demand $y^+ \approx 1$. It therefore lowers computational cost while, as confirmed by the experimental temperature histories presented in Chapters 3 and 4, keeping prediction errors within the validated band. The y^+ was evaluated from the friction velocity u_* and wall-normal distance y, as defined below (ANSYS Inc., 2023; Wilcox, 1998):

$$y^+ = \frac{\rho u_* y}{\mu} \tag{2.8}$$

Multiple Reference Frames (MRF):

The MRF approach was implemented to model the rotational effects of the furnace fans without requiring a sliding mesh. Cylindrical subdomains were defined around each fan, where

governing equations were solved in the rotating reference frame. The relationship between relative velocity (v_{rel}) and absolute velocity (v) is given by (ANSYS Inc., 2023):

$$v_{rel} = v - (\omega \times r) \tag{2.9}$$

Where v_{rel} is the relative velocity, ω is the angular velocity vector, and r is the position vector. This method ensures computational efficiency by avoiding the complexities of mesh deformation while accurately capturing swirl and recirculation effects.

2.3.3 Radiation Modeling

At tempering temperatures up to 600 °C, radiation can be a dominant heat transfer mode (Howell, Mengüç, Daun, & Siegel, 2020; Versteeg & Malalasekera, 2007). Two different radiation models were employed depending on the analysis objectives:

Surface-to-Surface (S2S) Model:

The S2S model neglects the participation of the gas phase and focuses on the radiative exchange between opaque surfaces in an enclosed domain. In this model, each surface or boundary is divided into discrete patches. The energy flux leaving surface i (ANSYS Inc., 2023; Versteeg & Malalasekera, 2007):

$$q_{out,i} = \varepsilon_i \sigma T_i^4 + \rho_i \sum_{j=1}^{N} F_{ij}\, q_{out,j} \tag{2.10}$$

Where ε_i is the emissivity of surface i, σ is the Stefan–Boltzmann constant, T_i is the surface temperature of patch i, $q_{out,j}$ is the energy flux leaving the surface j (emission plus reflection), F_{ij} is the view factor from surface i and surface j, and $\rho_i = (1 - \varepsilon_i)$ is the reflectivity of surface i. This approach was predominantly applied in Chapter 3, where the gas participation was

relatively small compared to the direct radiative exchange between the furnace walls and the forging surfaces.

Discrete Ordinates (DO) Model:

In cases where the furnace gas could absorb or emit radiation, or where directional effects became more influential (as in Chapter 4), the DO model was adopted. This model solves the Radiative Transfer Equation (RTE) in a finite number of discrete solid angles (ANSYS Inc., 2023; Versteeg & Malalasekera, 2007):

$$s.\nabla I(r,s) + (a+\sigma_s)I(r,s) = a\frac{\sigma T^4}{\pi} + \sigma_s \int_{4\pi} I(r,s')\phi(s',s)d\Omega' \quad (2.11)$$

Where $I(r,s)$ is the radiation intensity at position r in direction s, s is a unit direction vector, a is the absorption coefficient (m^{-1}), σ_s is the scattering coefficient (m^{-1}), σ is the Stefan–Boltzmann constant, T is the local temperature (K), $\phi(s',s)$ is the scattering phase function, describing how radiation is redistributed from direction s' to s, and $d\Omega'$ indicates integration over all solid angles 4π. By discretizing directions and solving the RTE, the DO model captures gas radiation, potential scattering, and directional intensity variations to give a more nuanced heat-flux distribution. Although more computationally demanding, this was essential for analyzing configurations where hot air had a measurable radiative interaction with the load (Versteeg & Malalasekera, 2007).

Material Emissivity:

Furnace walls were assigned an emissivity of ~0.75, while oxidized steel surfaces had slightly higher values (~0.80) (Bohlooli Arkhazloo, 2020; Paloposki & Liedquist, 2005). Sensitivity tests and furnace experiments, as reported by Staggs and Phylaktou (Staggs & Phylaktou, 2008), indicate that higher emissivity can significantly increase radiative heat flux and lead to higher surface temperatures in steel structures. This underscores the necessity of accurately specifying emissivity values in CFD simulations of radiative heat transfer in steel-dominated environments.

2.3.4 CAD Geometry, Mesh Generation, and Boundary Conditions

CAD Geometry:

A detailed 3D geometry of the car-bottom industrial electric furnace and the forging blocks was constructed in CATIA, starting from dimensioned industrial drawings and on-site measurements. Initial 2D engineering layouts provided by the industrial partner were converted into a preliminary 3D representation. Subsequently, a series of joint reviews with the partner's engineering team ensured that all critical dimensions—such as fan placement, heating element locations, and insulation thickness—were accurately reflected. Where possible, direct measurements of furnace door width, wall thickness, and car-bottom height were performed on-site to confirm the accuracy of the drawings.

In parallel, the forging block geometry was modeled based on the partner's data sheet for each forging type. For large rectangular, field measurements (e.g., length, width, thickness) were taken to verify that manufacturing tolerances were consistent with the nominal CAD dimensions. These blocks were then virtually positioned on the car-bottom in the same arrangements used in actual industrial runs, including spacers and skids to mimic real stacking practices. In addition, three cylindrical subdomains corresponding to the ceiling-mounted fans were designated for later Multiple Reference Frame (MRF) definitions, enabling the solver to capture the rotation-driven flow in the furnace.

Particular emphasis was placed on representing the heating elements. Each bank of electric resistors on the walls or ceiling (based on the simulation scenario) was incorporated as simplified surfaces with user-defined thermal boundary conditions (Section 2.2.3). This level of geometric detail allowed the CFD model to capture not only convection around the fans but also the localized radiative flux from heating element arrays. Ultimately, the validated 3D CAD model served as the foundation for generating high-fidelity computational meshes and underpinned all subsequent CFD and heat transfer analyses.

Mesh Generation:

Meshes were created using ANSYS Meshing, with local refinements to capture complex flow regions and thermal boundary layers (ANSYS Inc., 2020). Two principal types of meshes were employed across different scenarios:

- **Hexahedral-Structured Mesh:** Primarily in Chapter 3, focusing on simpler furnace geometry and fewer block configurations.
- **Poly-Hex Core Mesh:** Adopted in Chapter 4, suitable for complex heating element layouts and multi-objective optimization cases.

Cell count varied between 7.5×10^5 and 10×10^6, depending on the level of refinement and the study objectives (coarse to fine). Mesh-independence tests confirmed that beyond ~3 million cells, further refinement yielded minimal changes in block temperatures (<1–2% discrepancy). Figure 2.4 compares the poly-hex core and hexahedral meshes, highlighting refined fan subdomains and skid contact regions to accurately capture local flow phenomena.

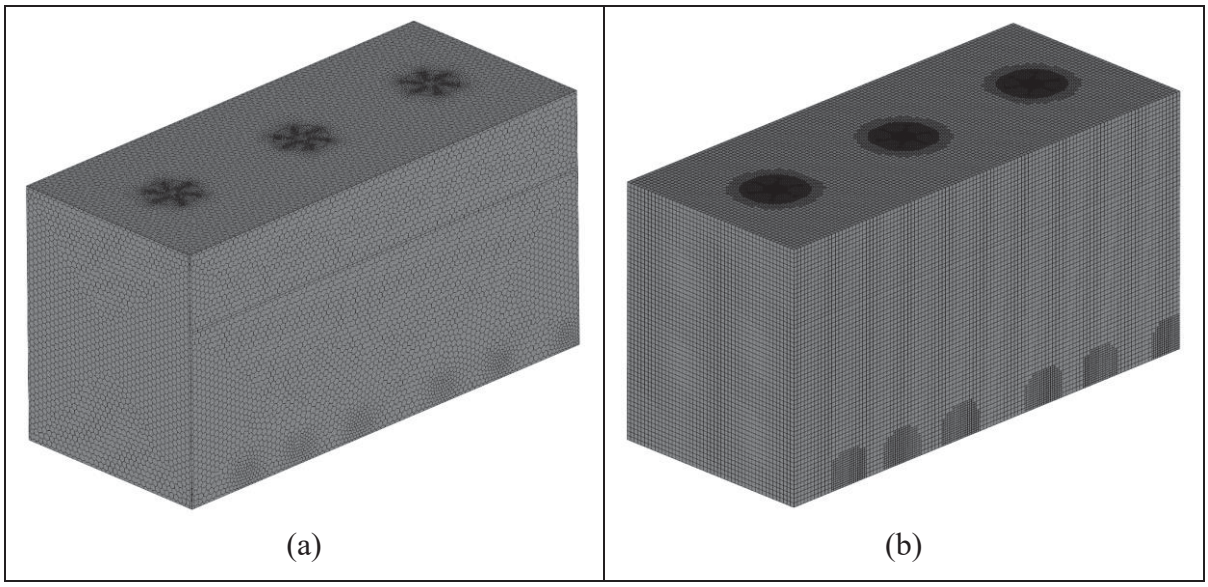

Figure 2.4 Sample computational meshes used in this study: (a) poly-hex core layout with refined fan region, (b) structured hexahedral mesh showing refinement near skids

Boundary Conditions (BCs):

Appropriate BCs were specified for the furnace walls, fans, and solid blocks so that the numerical model reproduced the dominant heat- and momentum-transfer phenomena, ensuring realistic behavior without introducing unnecessary geometric or material detail:

- **Furnace Walls:** The insulation assembly was treated as an externally insulated wall with a net heat-loss coefficient of $q_{loss} = 5.9$ kW m^{-2}, derived from a one-dimensional conduction calculation (Hadała, Malinowski, & Rywotycki, 2017) through the 254 mm ceramic-fiber blanket ($k \approx 0.16$ W m^{-1} K^{-1} at 540 °C) and validated by spot thermography that showed outer-casing temperatures below 80 °C during production runs.
- **Fans:** Each of the three ceiling fans was enclosed in a cylindrical rotating sub-domain that solved the governing equations in a frame spinning at 1750 rpm. The MRF method is recommended in the ANSYS Fluent Theory Guide (ANSYS Inc., 2023) for industrial applications because it reproduces the time-averaged swirl obtained with a full sliding-mesh model at a fraction of the CPU cost; A continuity interface enforces momentum and energy conservation across the rotating/stationary boundary. Published large-fan benchmarks report 70–85 % CPU savings while keeping velocity and pressure fields within ±3 % (Bergmann, Götten, Braun, & Janser, 2022; Go, Bae, Ryi, Choi, & Lee, 2022).
- **Forging Blocks:** Blocks were treated as conjugate solids with temperature-dependent thermal conductivity and specific heat (properties from JMatPro, see Section 4.4). No internal volumetric heat generation/loss was included, because tempering occurs above the martensite transformation range yet well below the eutectoid (A_1) temperature (~ 730 °C), where no re-austenitization arises, and therefore no significant latent-heat effects need be considered (Dossett & Totten, 2013). Radiative and convective coupling to the gas phase were activated on all block surfaces.
- **Initial Conditions:** Start-up simulations used a uniform 23 °C field to represent a cold charge. For partial-load scenarios, the measured quench-exit temperature (≈ 160 °C) was imposed on the blocks, while the gas was left at ambient.
- **Time-Dependent Heating Profile:** The electrical-power ramp recorded by the furnace PLC (10-second resolution) was converted to an equivalent wall heat-flux using $\eta_{ele}c$ =

0.98, a typical element efficiency for resistance-heated furnaces (Kanthal, 2001), and applied as a tabulated boundary condition.

2.3.5 Transient Simulation Setup and Convergence Criteria

In transient modeling, time derivatives ($\partial/\partial t$) are retained in all governing equations to resolve temporal changes in variables such as velocity, temperature, and pressure (Versteeg & Malalasekera, 2007). Owing to the prolonged nature of industrial tempering cycles—ranging from 24 to 48 hours or more—a robust transient methodology was crucial to capture the full thermal history of both the furnace environment and the forging blocks. This section details the approach used to strike a balance between computational feasibility and physical fidelity:

Time-Step Selection and Ramping Strategy

- **Time Steps:** Variable time steps were used to balance computational cost and resolution (ANSYS Inc., 2023). During non-iso thermal heating phases, smaller time steps (1−5 seconds) were employed to capture steep gradients, while longer steps (5−10 seconds) sufficed during steady soaking phases.
- **Temporal Discretization:** A second-order implicit backward-differencing (BDF2) scheme was applied. Because its error scales with Δt^2, it keeps temperature histories much closer to the true solution than the first-order Euler method, which can artificially smooth transients. Textbook tests show that BDF2 introduces roughly one-tenth of the numerical damping of Euler for heat-diffusion problems, yet it stays stable for any practical time-step size (Ferziger, Perić, & Street, 2019; Versteeg & Malalasekera, 2007).

Spatial Discretization and Solver Settings

- **Momentum and Energy:** Second-order upwind schemes were chosen to minimize numerical diffusion while preserving accuracy in regions with strong temperature or velocity gradients (Versteeg & Malalasekera, 2007).
- **Pressure–Velocity Coupling:** The SIMPLE or SIMPLEC algorithm ensured robust convergence for recirculating flows inside the furnace (Piyapaneekoon & Kowitwarangkul,

2020). In higher swirl cases, under-relaxation factors for momentum, turbulence, and energy were fine-tuned to maintain stability (ANSYS Inc., 2023).

Convergence and Monitoring

- **Residual Criteria:** At each time step, momentum, continuity, and turbulence equations converged to ~10^{-5}, whereas energy and radiation equations required residuals as low as 10^{-6} or 10^{-9}, depending on the model complexity.
- **Key Physical Monitors:** Thermocouple-mapped nodes in the forging blocks were tracked over time. Their predicted temperatures were plotted in real-time and compared to experimental logs for immediate feedback on solution accuracy.

Computational Efficiency

All simulations were run in parallel on high-performance clusters (40–64 cores) provided by Compute Canada, with CPU clock speeds of 2.4–2.65 GHz (Digital Research Alliance of Canada, 2025). Each 24–48 hours heat-treatment scenario required 4–6 days of computation. Load balancing and domain decomposition were performed to ensure no single region of the grid dominated the solve time (ANSYS Inc., 2023). By employing this multi-pronged transient approach—encompassing adaptive time-step control, careful mesh selection, and thorough convergence checks—the CFD simulations reliably captured the complex interplay of radiation, turbulence, and conduction in large-scale industrial heat treatment. This solid numerical foundation subsequently supported the optimization efforts in later chapters.

2.3.6 Validation Strategy

To build confidence in the CFD predictions (Versteeg & Malalasekera, 2007), the benchmark simulations' results were systematically compared against industrial data (Section 2.2):

- Thermocouple Correlation: Simulated temperatures at nodes co-located with thermocouples were tracked over time, overlaying them on measured temperature curves. Deviations typically fell within 2–7% of experimental values.

- Power Usage Checks: In certain cases, the net energy absorbed by the system was compared to furnace power consumption logs to ensure consistent energy balances.
- Temporal Accuracy: The average time shift between measured and predicted temperature profiles rarely exceeded 0.01% of the total cycle. This alignment was particularly crucial for identifying the soak time and ramp durations.
- Spatial Non-Uniformities: In Chapter 3, predicted temperature gradients across the block (200–300 K) matched the thermocouple observations, confirming the model's ability to capture stacking and spacer effects.

This high-fidelity validation underpins the confidence in subsequent CFD-driven optimization methods (discussed in Section 2.4), enabling robust exploration of operational parameters and design modifications that further enhance industrial heat treatment efficiency and product quality.

2.4 Optimization Methodology

A central objective of this research was to identify operating parameters—such as stacking configurations, spacer, and skid dimensions, or heating element layouts—that optimize furnace performance from temperature uniformity, consistent mechanical properties, and energy usage. Building on the validated CFD framework (Section 2.3), several multi-objective optimization methods were employed to systematically search for improved solutions while balancing sometimes conflicting objectives. The following subsections present the conceptual approaches (Section 2.4.1), elaborate on polynomial regression or surrogate modeling (Section 2.4.2), discuss key implementation details (Section 2.4.3), and define the metrics used to measure performance (Section 2.4.4).

2.4.1 Multi-Objective Optimization Approach

Motivation and Principles

In the heat treatment of large steel blocks, multiple goals arise naturally:

- Minimize temperature non-uniformities, such as peak surface-to-surface or surface-to-center ΔT.
- Reduce processing time, which translates to shorter cycles needed for the blocks to reach the target temperature.
- Limit energy consumption, either by lowering total power usage or capping peak demand.

These objectives often conflict. For instance, an arrangement that heats forgings faster may raise internal temperature gradients, potentially compromising mechanical properties. Multi-objective frameworks therefore identify Pareto-optimal solutions, which are configurations where no single objective can be improved without negatively impacting another.

Genetic Algorithm (GA)

In cases involving combinatorial parameters—such as optimal wall coverage by heating elements—a genetic algorithm was employed. Within this work, these GA studies predominantly took place during the second phase of the research (Chapter 4), investigating heating element layouts. A GA (Colin R. Reeves 2002):

- Begins with a population of candidate solutions, each representing a distinct set of design variables (e.g., coverage percentages or spacer arrangements).
- Evaluates each solution's "fitness" based on the objective functions (Section 2.4.4).
- Applies selection, crossover, and mutation to produce new generations of solutions.
- Iterates until convergence criteria (e.g., stable Pareto front) or a maximum number of generations is reached.

GAs are well-suited for high-dimensional or discrete design spaces without straightforward gradients, making them an excellent choice for industrial furnace design (Chapman, Saitou, & Jakiela, 1994).

Pareto Search (PS)

In addition to the Genetic Algorithm (GA), a Pareto Search (PS) algorithm was applied to enhance solution diversity and explore localized trade-offs within smaller or less complex design spaces. While GA efficiently scans broader solution domains, PS is particularly suitable for refining and identifying non-dominated solutions in one-dimensional or tightly constrained problems—such as wall coverage adjustments. In this study (Chapter 4), PS enabled a focused exploration of the Pareto front, where improvements in one thermal metric (e.g., center-to-surface differential) required trade-offs in another (e.g., processing time). This dual approach ensured both exploratory breadth and local precision, strengthening confidence in the final layout recommendations (MathWorks, 2021).

2.4.2 Polynomial Regression Fitting (Surrogate Modeling)

Rationale and Overview

Although one can directly link CFD evaluations to multi-objective algorithms, each candidate solution triggers a full transient CFD simulation, which is often computationally expensive. To alleviate this cost, polynomial regression (surrogate) techniques were integrated, especially during the second major phase (Chapter 4), where the design space (e.g., coverage percentage of heating elements) was extensively explored.

Surrogate Modeling Steps

- **CFD Sampling:** A set of strategically chosen design points—e.g., coverage ∈ [10%, 20%, 30%, 50%, …] or specific spacer dimensions—was simulated in detail using the validated CFD model.
- **Data Extraction:** For each sampled design, key performance metrics such as peak temperature non-uniformities, center-to-surface temperature differentials, and residence time were recorded.
- **Polynomial Fitting:** A polynomial function (often cubic) approximated how each objective responded to the design variables (e.g., coverage fraction). The general form used here can be represented as (Ostertagová, 2012):

$$\hat{y}(x_1, x_2, \dots, x_n) = \beta_0 + \sum_i \beta_i x_i + \sum_{i,j} \beta_{i,j} x_i x_j + \sum_{i,j,k} \beta_{i,j,k} x_i x_j x_k + \cdots \quad (2.12)$$

where $\hat{y}$ is the predicted objective (e.g., maximum temperature non-uniformity), x_i are the design variables (like coverage %), and β coefficients are fit from the data.

- **Surrogate Usage:** During GA or Pareto search iterations, the polynomial function provided a fast approximation instead of re-running the full CFD. This markedly reduced computational overhead, enabling the exploration of many more potential designs.

Advantages

Polynomial surrogate models offer a practical balance between computational efficiency and the ability to capture moderate nonlinear behaviors in complex systems (G. G. Wang & Shan, 2006). They are straightforward to implement and require fewer samples compared to more complex machine learning models. This efficiency makes them particularly suitable for preliminary design explorations and optimization tasks where multiple real-scale tests are infeasible or where computational resources limit the number of high-fidelity simulations such as CFD. After identifying near-optimal designs through the surrogate model, a targeted set of full CFD simulations was performed to validate these results and confirm the reliability of the surrogate-based predictions within the context of the actual furnace behavior.

2.4.3 Implementation Details and Parameter Tuning

Software Integration

The CFD simulations were carried out in ANSYS Fluent (2022 and 2023 versions) while the optimization methods—GA or Pareto search—were coded in MATLAB R2021 or Python-based frameworks. Between these platforms, data was exchanged via automated scripting or CSV output/input. This facilitated batch runs in high-performance computing environments.

Genetic Algorithm Parameters

The iterative logic of the GA, illustrated in Figure 2.5, forms the backbone of the evolutionary optimization strategy used in this study. Rather than relying on gradients, GA applies stochastic operators—selection, crossover, and mutation—to evolve candidate designs across generations. This makes it well-suited for discrete, nonlinear problems such as heating element layout, where interactions among design variables can be complex and non-intuitive. The flowchart highlights how the algorithm balances exploration and exploitation: initial diversity helps scan the broader design space, while repeated selection and recombination gradually concentrate the search near promising regions. This adaptive search mechanism is essential in high-dimensional thermal systems, where exhaustive evaluations via CFD would be computationally prohibitive (Pei et al., 2022):

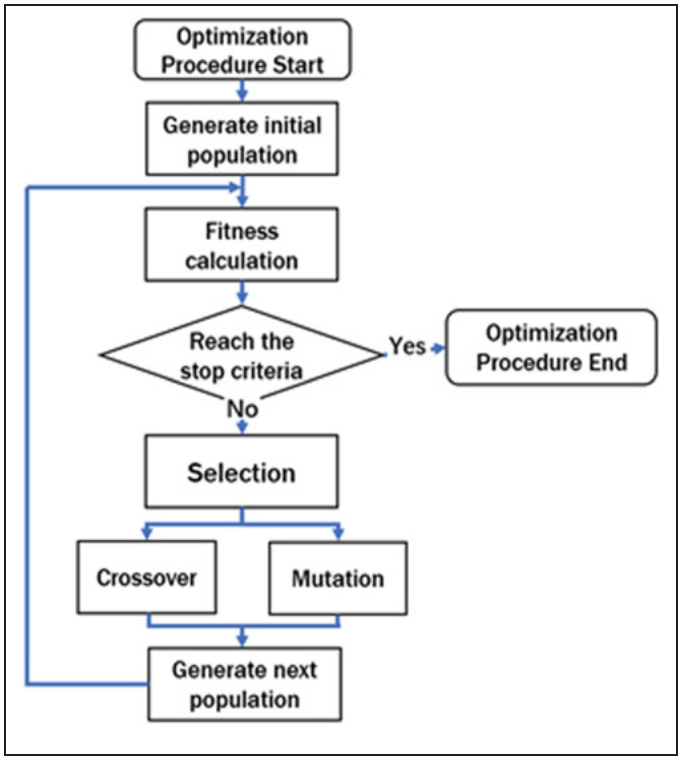

Figure 2.5 Flowchart of genetic algorithm optimization
Taken from Pei et al. (2022, p. 2)

Pareto Search Settings

Parallelly, for multi-objective optimization, a Pareto search or direct polling approach was also employed. The method systematically probed the design domain, retaining non-dominated solutions. Within ~50–100 iterations, the algorithm would stabilize a near-optimal Pareto front of solutions. Often, up to 200 front points were saved before the search terminated once consecutive improvements dropped below a threshold (e.g., 10^{-6} on objective functions).

Convergence and Final Selection

After 50–100 generations (for GA) or ~100 iterations (for Pareto search), solutions typically converged along a near-optimal frontier. Decision-makers then chose a particular solution or a set of solutions by weighing the importance of temperature uniformity vs. time or energy. If a polynomial surrogate was in use, the final designs were re-simulated with the full CFD to confirm the accuracy and ensure that surrogate approximations did not distort the solutions.

2.4.4 Evaluation Metrics

Metric Definitions

Throughout the optimization process, each candidate furnace design or loading configuration was judged by quantitative measures derived from the transient CFD or the polynomial surrogate. The most critical metrics included:

- Surface Temperature Non-Uniformity $\Delta T_{surf,\,max}$: the instantaneous difference between the hottest and coldest points on the block surface (or surfaces, in multi-block cases). Often, the peak value of this difference over the entire heat cycle was used as the objective.
- Surface-to-Center Differential $\Delta T_{sc,\,max}$: the temperature gradient between the block's outer surface and its geometric center at any point in time. Large ΔT_{sc} can indicate an undesirable risk of internal stresses or microstructural variance.
- Centers Temperature Differential $\Delta T_{centers}$: the difference between the centers of the "most heated" and "least heated" blocks in multi-block loads. This metric was particularly crucial in Chapter 3, where multiple forgings were stacked or arranged in the same furnace run.

- Time Metrics (TM): typically, the time to target, representing how many hours until each block center surpasses a chosen temperature (e.g., 537 °C). Minimizing this shortens the overall cycle.
- Energy Usage or Power Consumption: in certain design scenarios, the cumulative or peak kWh was also tracked.

Composite vs. Multi-Objective Formulations

During the preliminary phases of this study, several single-objective pilot tests were conducted by combining non-uniformity (ΔT) and time (TM) metrics into a weighted sum formulation. A representative example is:

$$F = \left(W_1 \times \Delta T_{surf,max,ub}\right) + \left(W_2 \times \Delta T_{surf,max,lb}\right) + \left(W_3 \times \Delta T_{sc,max,ub}\right) + (W_4 \times \Delta Tsc, max, lb) + (W_5 \times \Delta T_{centers}) + (W_6 \times TM_{ub}) + (W_7 \times TM_{lb}) \quad (2.13)$$

where $W_i = 1$ are weighting coefficients assigned to reflect the prioritized criteria of the industrial partner. These initial tests allowed rapid exploration but were limited in capturing the complexity of trade-offs between objectives. Therefore, in the main optimization framework, each objective was treated independently, and multi-objective algorithms (GA and PS) were applied to construct Pareto fronts. This strategy provided a deeper understanding of the competing effects between temperature uniformity and processing time which is critical for practical furnace design improvements.

In summary, the combined use of multi-objective algorithms, polynomial surrogates, robust parameter tuning, and comprehensive performance metrics constituted a central pillar of this methodology, enabling a systematic evaluation of design and operating conditions in large-scale industrial furnaces.

2.5 Data-Driven Machine Learning Method

Although the CFD-based optimization described in Section 2.4 offers a detailed understanding of flow and heat transfer phenomena, many industrial processes require rapid predictions of furnace loading outcomes. High-fidelity CFD simulations, while accurate, are computationally demanding, making them less suitable for frequent, real-time decisions (Ferziger et al., 2019). To address this limitation, a machine learning (ML) framework was established to predict optimal loading cycles, leveraging historical data collected from day-to-day furnace operations. The following subsections describe the industrial dataset (Section 2.5.1), data-validation and preprocessing techniques (Section 2.5.2), the mathematical foundation and model choice (Section 2.5.3), hyper-parameter tuning and model-building workflow (Section 2.5.4), and the metrics that will later be used for performance assessment (Section 2.5.5).

2.5.1 Industrial Dataset Description

Over nine months, operational logs were recorded for each tempering cycle performed in three identical 112 m^3 electric furnaces located at Sorel Forge. Figure 2.6 presents the front and back of a representative paper datasheet used by furnace technicians to document key parameters (e.g., block dimensions, furnace conditions) for each cycle (Finkl Steel Inc., 2021). The information from all physical logs was then digitized into a single spreadsheet, forming a unified database.

This process produced 1,162 entries (one per forging), each row containing eight input features—six numerical and two categorical—and three batch-level targets:

- **Eight Input Features**
  1. Material Homogeneity (categorical: “Same” / “Mix”)
  2. Shape (categorical: “Cylindrical” / “Cubic”)
  3. Weight (kg)
  4. Width (cm)
  5. Thickness (cm)
  6. Length (cm)
  7. Holding Duration (hr)
  8. Temperature (°C)
- **Three Target Outputs**
  1. Total Weight (kg)
  2. Forging Count (units)
  3. Total Length (cm)

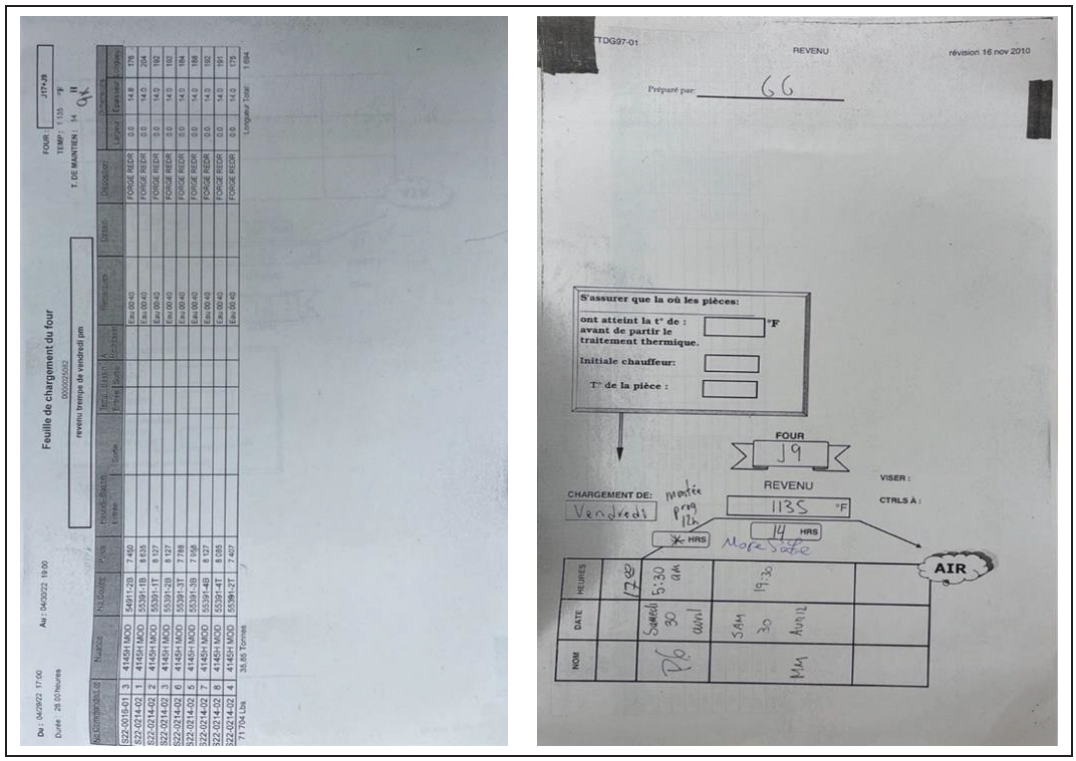

Figure 2.6 Typical hardcopy datasheet used on-site to record forging dimensions and furnace conditions

In this multi-target framing, each block's shape and dimensions become key factors in predicting how technicians group blocks into a single furnace load. Heavier and wider blocks, for instance, might be placed in fewer numbers per load, while lighter or narrower blocks could be batched together more densely. By training an ML model on these historical outcomes, the algorithm can estimate how a new forging of specific dimensions is likely to be loaded, aiding in quicker scheduling decisions and better resource utilization.

2.5.2 Data Cleaning, Validation & Transformation

Data Cleaning

The initial data—extracted from industrial logs—contained occasional incomplete or inconsistent entries (e.g., missing feature values, an overall forging width smaller than its specified thickness). Each row in the dataset underwent a validity check. If certain critical features (such as shape or weight) were missing, the relevant rows were either imputed (where possible) or removed if the missingness could not be resolved from the records.

Validation of Outliers

In some instances, extreme values (e.g., very large block weight or unusually thick forging) appeared. These outliers were traced back to the original forging logs to verify their authenticity. If confirmed as actual, such as an extra-large forging built for a special order, they were retained so that the model could capture rare but industrially relevant events. If identified as erroneous (e.g., sensor malfunctions), they were corrected or removed.

Categorical Encoding (One-Hot)

To handle categorical variables, a one-hot encoding method was employed. Suppose a given categorical feature X can take k distinct values $[x_1, x_2, \dots, x_k]$. One-hot encoding replaces X with k new binary features $[X_1, X_2, \dots, X_k]$, where (Hastie et al., 2009; James, Witten, Hastie, & Tibshirani, 2013):

$$X_i = \begin{cases} 1, & if\ X = x_i \\ 0, & otherwise \end{cases} \tag{2.14}$$

For example, “Shape_Cylinder” and “Shape_Rectangular” become separate binary columns. This procedure prevents the imposition of an ordinal relationship among categories.

Yeo-Johnson Transformation

Many numeric features (e.g., Weight, Width, Thickness, Length) displayed significant skewness or heavy tails, making direct use of raw values susceptible to outlier dominance. To mitigate these issues and to approximate normality, the Yeo-Johnson transform was applied. This transform generalizes the Box-Cox method to allow for zero and negative values, thereby accommodating industrial data that might contain measurements below unity or even negative offsets. Given an original data point x and a transformation parameter λ, the Yeo-Johnson function $\phi_\lambda(x)$ can be defined piecewise as (Yeo, 2000):

$$\phi_\lambda(x) = \begin{cases} \dfrac{(x+1)^\lambda - 1}{\lambda}, & if\ x \geq -1, \lambda \neq 0, \\ ln\,(x+1), & if\ x \geq -1, \lambda = 0, \\ 1 - \dfrac{(1-x)^{2-\lambda} - 1}{2-\lambda}, & if\ x < -1, \lambda \neq 2, \\ -\ln\,(1-x), & if\ x < -1, \lambda = 2, \end{cases} \tag{2.15}$$

Where x is the original value (which may be ≥ -1 or < -1, λ is the transformation parameter, typically determined by an internal optimization routine (e.g., maximum likelihood estimation) or cross-validation to minimize skewness, $\phi_\lambda(x)$ is the transformed value, now less skewed and more compatible with models that assume roughly Gaussian distributions of inputs. By employing the Yeo-Johnson approach, the data is mapped into a domain where extreme or rare observations exert a less disproportionate effect on subsequent analyses.

Feature Scaling

After the Yeo-Johnson transformation, Robust Scaling was applied to further reduce the influence of outliers. Unlike standard z-score normalization—which subtracts the mean and

divides by the standard deviation—robust scaling subtracts the median of a feature and then divides by the interquartile range (IQR). For a data point x, the robust-scaled value x^* is (Brownlee, 2020):

$$x^* = \frac{x - median(x)}{IQR(x)} \tag{2.16}$$

Where median(x) is the median of all observed x-values for that feature, and IQR(x) is the interquartile range, defined as the difference between 75th (Q_3) and 25th (Q_1) percentiles of x.

Because both the median and IQR are robust to large deviations in the tails of the distribution, no single extreme outlier can disproportionately shift the scaling. Consequently, robust scaling keeps the bulk of data points in a comparable range while preserving unusual observations, which may be legitimate extreme values in an industrial setting. This ensures that normal forging sizes or dimensions (centered around the median) remain the primary focus for the model, without discarding rare but significant large-scale forgings.

2.5.3 Mathematical Foundation and Algorithm Choice

Rationale

Among various gradient-boosting implementations, XGBoost (eXtreme Gradient Boosting) is recognized for its efficiency and scalability in handling industrial datasets. Several factors justify its strong performance in various applications (Wade & Glynn, 2020):

- **Adept at Mixed Feature Types:** XGBoost handles both categorical and numeric inputs, and, when combined with one-hot encoding, it effectively captures nonlinear interactions in multi-dimensional data.
- **Robust Regularization:** XGBoost offers built-in L1 and L2 regularization (i.e., alpha and lambda parameters), curbing overfitting by penalizing overly complex trees.
- **Handling Large Datasets:** The parallelized nature of XGBoost allows faster training, which is advantageous even in moderately sized industrial datasets such as ours (≈ 1,162

rows, but with potential expansions over time). Its efficiency also suits the need for iterative hyperparameter tuning and cross-validation, as described below.

Multi-Output Approach

The problem required predicting three correlated targets—Total Weight, Forging Count, and Total Length—each representing a fundamental aspect of how blocks are batched together. Although it is possible to train three separate single-output XGBoost models, a multi-output approach can sometimes enhance performance by learning shared patterns in the data (Schmid, Gerharz, Groll, & Pauly, 2022) (e.g., the same forging dimension influences both total weight and total length in the final load). Ultimately, both single- and multi-output regressors were tested; The final method was chosen based on cross-validation results, with multi-output XGBoost performing well in this industrial dataset. Preliminary trials with multiple-linear regression and a shallow two-layer ANN failed to capture the pronounced non-linear interactions in the data set (cross-validated $R^2 < 0.70$ for every target). These baselines therefore served only as sanity checks; all subsequent development focused on the gradient-boosted tree framework provided by XGBoost, whose regularised objective and column-sampling strategy are well suited to noisy, mixed-type industrial data.

2.5.4 Model Building

Hyperparameter Tuning

A range of XGBoost hyperparameters like n_estimators, learning_rate, max_depth, subsample, and colsample_bytree were examined via grid search, employing a 5-fold cross-validation scheme (Wade & Glynn, 2020). The grid search explored:

- n_estimators ∈ [100 … 2000] (step = 25),
- learning_rate ∈ [0.0125 … 0.20] (step = 0.0125)
- max_depth = 5 … 15 (step = 1),
- subsample ∈ 0.10 … 1.00 (step = 0.05),
- colsample_bytree ∈ 0.10 … 1.00 (step = 0.05)

Each hyperparameter combination was trained on ~80% of the data (using a 5-fold CV within that split) and validated on the remaining 20%. Optimal settings were those maximizing R2 while minimizing MSE, as discussed in Section 2.5.5.

Training and Implementation

All scripts were authored in Python, using the XGBoost and scikit-learn libraries. The typical training pipeline includes (Brownlee, 2020)::

1. Preprocessing: Missing data handling, outlier filtering, one-hot encoding, Yeo-Johnson transforms, and robust scaling.
2. Data Segmentation: Raw logs are split into training and test sets.
3. Hyperparameter Optimization: Iterative grid search with cross-validation.
4. Model Selection and Validation: Evaluating multiple parameters set for best performance; the final XGBoost model is locked in.
5. Deployment: The trained regressor is then ready for inference, predicting how newly defined forgings will fit into a load plan.

Learning curves were also monitored to determine whether adding more data (beyond 1,162 samples) would further reduce error. In many industrial contexts, performance plateaus once the available data volume provides adequate coverage of typical forging scenarios. Figure 2.7 illustrates the end-to-end ML pipeline (H. Liu, 2024). This flow ensured systematic data treatment, transparent model configuration, and reliable performance estimation prior to real-world deployment.

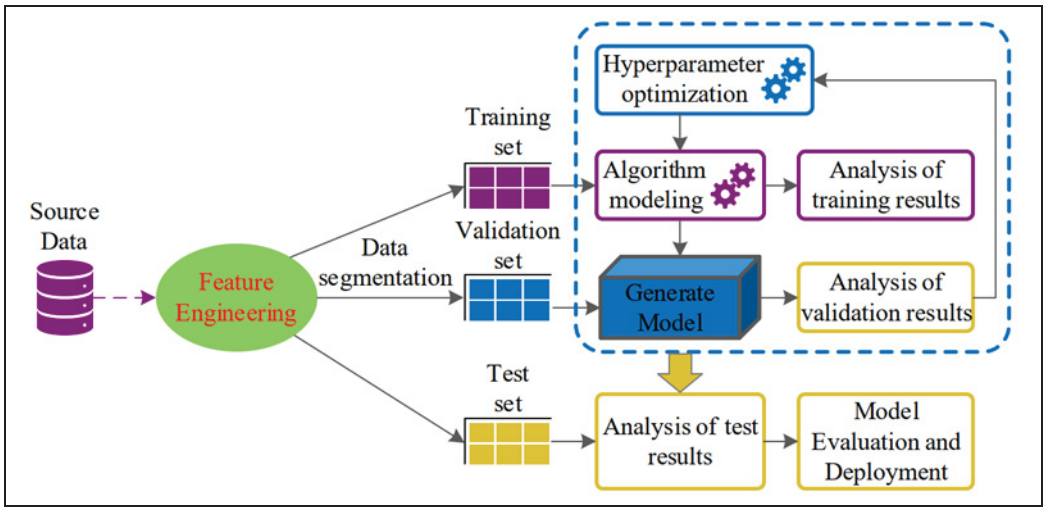

Figure 2.7 Schematic of the typical machine learning workflow used in this study
Taken from H. Liu (2024, p. 3)

2.5.5 Evaluation Metrics

To assess regression performance, the following metrics were computed on the unseen test set (i.e., data not used for training or validation folds) (Ostertagová, 2012; Pan & Montreuil, 2021):

1. Mean Absolute Error (MAE):

$$MAE = \frac{1}{N}\sum_{i=1}^{N}|y_i - \hat{y}_i| \tag{2.17}$$

2. Root Mean Squared Error (RMSE):

$$RMSE = \sqrt{\frac{1}{N}\sum_{i=1}^{N}(y_i - \hat{y}_i)^2} \tag{2.18}$$

3. Coefficient of Determination (R^2):

$$R^2 = 1 - \frac{\sum_{i=1}^{N}(y_i - \hat{y}_i)^2}{N\sum_{i=1}^{N}(y_i - \bar{y})^2} \tag{2.19}$$

Where $\bar{y}$ is the mean of the actual targets y. An R^2 value of 1 indicates perfect agreement between predictions $\hat{y}_i$ and the true values y_i, whereas 0 indicates that the model does not improve on simply predicting $\bar{y}$.

These performance metrics demonstrate that the ML-based approach could replicate or even surpass the consistency of human-driven loading decisions—particularly under real-world variations in forging dimensions and furnace conditions. Moreover, the nonlinear capabilities of XGBoost allowed the model to capture subtle interactions among shape, mass, and geometrical attributes that simpler regression methods might overlook.

2.6 Summary of Methodological Workflow

Throughout this methodology chapter, a comprehensive end-to-end workflow has been established to investigate, optimize, and predict the heat treatment performance of large steel blocks in an industrial electrical furnace. Below is a concise recap of how each methodological element (Sections 2.1–2.5) integrates into a unified approach:

1. Experimental Foundations (Sections 2.1 and 2.2)
    - The research began by defining the overall objectives: enhancing temperature uniformity, reducing suboptimal loading, and ensuring consistent mechanical properties.
    - Extensive industrial measurements provided a robust dataset: real-time furnace power usage, thermocouple readings on forging blocks, and relevant geometry information. These measurements served a dual purpose:
    - Validation: Experimental data confirmed the accuracy of the computational models.
    - ML Training: The same data informed the machine-learning pipeline for predicting loading cycles.

2. CFD Modeling and Simulation (Section 2.3)
    - A transient CFD approach was developed to simulate the car-bottom electric furnace environment, focusing on fluid flow (driven by axial fan circulation) and conjugate heat transfer (convection, conduction in the blocks, and radiation).
    - Key features included the realizable k-ε turbulence model, multiple reference frames (MRF) for fan rotation, and S2S or DO radiation models.
    - Model validation involved comparing predicted and measured block-surface temperatures. Once validated, the CFD framework enabled detailed "what-if" analyses for various stacking patterns and heating element layouts.

3. Optimization Methodologies (Section 2.4)
    - Multi-objective evolutionary algorithms (such as genetic algorithms and Pareto searches) were integrated with polynomial regression (surrogate modeling) to rapidly locate near-optimal solutions.
    - In Chapter 4, polynomial fitting significantly reduced the computational burden of exploring multiple design scenarios (e.g., heating element coverage on furnace walls).
    - By leveraging key metrics—including maximum surface-to-surface temperature differentials, center temperature gradients, and time to reach target temperature—these optimization loops systematically revealed furnace layouts that balanced uniformity with energy/time efficiency.

4. Data-Driven Machine Learning (Section 2.5)
    - Recognizing the need for quick predictions in routine operations, a machine learning framework was introduced (Chapter 5).
    - A dataset of 1,162 tempered blocks was compiled, capturing critical features (block geometry, shape, etc.) and the resulting "batch" parameters used by technicians (total weight, forging count, total length).
    - XGBoost Regressor was trained using cross-validation, robust scaling, and Yeo-Johnson transformations. This enables operators to predict how new blocks of a

particular dimension or shape are likely to be loaded, providing consistent scheduling and uniform outcomes without running a full CFD study each time.

5. Synergy and Final Integration
    - Experimental data underpins both the CFD validation and the ML dataset, ensuring real-world fidelity.
    - CFD analyses yield deep physical insights and guide essential design decisions (e.g., arrangements of spacers/skids or wall coverage by heating elements).
    - Multi-objective optimization extends CFD by systematically exploring trade-offs in design conditions, identifying robust solutions rather than a single “one-size-fits-all” configuration.
    - ML provides a fast, data-driven method for day-to-day loading cycle decisions, complementing the more detailed (but slower) CFD-based approach. The final objective is a blended methodology: critical design changes undergo CFD plus optimization, while routine scheduling relies on the ML predictor.

This integrated methodological workflow—from large-scale experiments and CFD modeling to optimization loops and ML-based predictions—facilitates a holistic strategy for enhancing the heat treatment process. In subsequent chapters, the results of each phase (Chapter 3, Chapter 4, Chapter 5) are presented and discussed, illustrating how these methods converge to offer practical, data-backed recommendations for industrial furnace operations.

CHAPTER 3

INFLUENCE OF SPACERS AND SKID SIZES ON HEAT TREATMENT OF LARGE FORGINGS WITHIN AN INDUSTRIAL ELECTRIC FURNACE

Sajad Mirzaei [a], Nima Bohlooli Arkhazloo [a], Farzad Bazdidi-Tehrani [b], Jean-Benoit Morin [c], Abdelhalim Loucif [c] and Mohammad Jahazi [a]

[a] Département de Génie Mécanique, École de Technologie Supérieure, Montréal, Quebec, Canada H3C 1K3
[b] School of Mechanical Engineering, Iran University of Science and Technology, Tehran, Iran 16846-13114
[c] Finkl Steel Inc., 100 McCarthy, Saint-Joseph-de-Sorel, Quebec, Canada J3R 3M8

Paper published in *Energies*, March 2023

Abstract

The influence of stacking patterns, through the different spacer and skid sizes, on the transient temperature distribution uniformity of large-size forgings in a 112-m^3 electrical heat treatment furnace was investigated by conducting CFD simulations and real-scale experimental validation. A 3D CFD model of the electrical furnace was generated, including a heat-treating chamber, axial flow fans, large-size blocks, skids, and spacers. Real-scale temperature measurements on instrumented test blocks during the heat treatment process were carried out to validate the CFD simulations. Results indicated that the CFD model was capable enough to determine the transient temperature evolution of the blocks with a maximum average deviation of about 6.6% compared to the experimental measurements. It was found that significant temperature non-uniformities of up to 379 K on the surfaces of the blocks due to the non-optimum stacking pattern were experienced by the blocks. Such non-uniformities could be reduced between 24 to 32% if well-adapted spacer and skid sizes were used in the stacking configurations. Based on simulation results and experimental validation work, optimum spacer

and skid sizes for uniform temperature distribution were proposed for different stacking patterns.

Keywords: Electrical furnace; computational fluid dynamics; multiple reference frame model; stacking pattern; temperature uniformity; spacer size; skid size

3.1 Introduction

High temperature industrial furnaces, in which the heat generation is mainly based on fossil fuel combustion or electricity, play a vital role in the iron and steel making industry. Energy saving in such furnaces directly limits the environmental footprint of steel-making industries, which has been reported to be among the top five most energy-intensive industry sectors (Kluczek & Olszewski, 2017). Furthermore, such an energy saving could significantly affect the final production cost (Chan, Yang, Lee, & Hong, 2010; Palacio-Caro et al., 2020) . Heat treatment processes are among the key contributors to energy usage in the iron and steel making industries. A heat treatment process called Quench and Temper (Q&T) is usually employed to obtain desirable properties in large-size high strength steel parts, such as dies or turbine shafts (Totten, 2006). The mechanical properties of the product, such as resistance, hardness, and toughness, are highly dependent on the cooling cycle and its parameters, such as quenching medium (oil, water, etc.), cooling time, quenching temperature, as well as tempering process parameters, which directly affect the metallurgical transformations of the steels. The tempering step is of crucial importance to the final mechanical properties of the product as major microstructural changes and metallurgical improvements take place during this step (Kang & Rong, 2006). These metallurgical interactions, such as the hardness reduction of brittle quench-hardened steel, improved toughness, and stress relieving, fundamentally depend on the tempering temperature and holding time in the heat treatment furnace (Askeland, Phulé, Wright, & Bhattacharya, 2003; Gao, Reid, Jahedi, & Li, 2000). It has been reported that non-uniform temperature distribution may result in non-uniform properties around the products and in some cases scrapping of the part (Bohlooli Arkhazloo, Bazdidi-Tehrani, Morin, & Jahazi, 2021; Gur & Pan, 2008). At the present time, most of the existing heat treatment furnaces in

the steel industry use natural gas as the heating source, and significant efforts have been devoted to the optimization of the tempering process in such furnaces (U.S. EIA, 2006). However, in recent years, with the implementation of new regulations on the reduction of global carbon dioxide emissions and fossil fuel usage, there has been significant growth in the employment of electrical batch-type furnaces for steel heat treatment processes, but, in contrast to gas-fired furnaces, very little data is available in the case of electrical furnaces, particularly industrial-sized ones. Thus, the accurate prediction and control of the transient temperature distribution and heat transfer to products in electrical furnaces are critical in order to optimize temperature uniformity and fluid flow circulation, similar to what was previously reported by Bohlooli et al. for gas-fired furnaces (N. B. Arkhazloo et al., 2019; Bohlooli Arkhazloo, 2020). The optimization process becomes even more complex when, due to production imperatives, multiple loading patterns and stacking configurations must be taken into account as they significantly affect the temperature distributions around the parts (Bohlooli Arkhazloo et al., 2021).

Improving the current practice in the industry, which is mostly based on empirical correlations that could result in significant deviations (Kang & Rong, 2006; S. F. Zhang, Wen, Bai, Chen, & Long, 2009), necessities a comprehensive and systematic quantitative analysis of thermal interactions within the heating chamber. Due to the complexity of the thermal field associated with turbulence and conjugate heat transfer, numerical analysis and simulation tools need to be used (Gao et al., 2000; Kang & Rong, 2006). This is also because of the fact that the experimental measurements and data acquisition are quite challenging to perform due to the high temperature ranges, size of furnaces and products, limited physical access, and huge instrumentation expenditure.

Recently, computational fluid dynamics (CFD), offering the simultaneous analysis of turbulent fluid flow and conjugate heat transfer, has been employed in several studies on the thermal analysis of industrial furnaces (Chattopadhyay, Isac, & Guthrie, 2010; S. F. Zhang et al., 2009). Studies comprising Harish et al. (Harish & Dutta, 2005) and Zhang et al. (S. F. Zhang et al., 2009), or recently published papers such as those by Mayr et al. (Mayr et al., 2017), Tang et

al. (Tang et al., 2017), and Liu et al. (Y. J. Liu, Li, Misra, Wang, & Wang, 2016), employed CFD simulations to investigate the heating procedure in different continuous reheating furnaces (for instance, pusher type furnaces or walking beam furnaces). On the other hand, batch-type heat treatment furnaces used in the tempering process, due to their longer process time (more than 24 h of heating and 48 h of holding for the large-size products (Gur & Pan, 2008)) require higher computational costs for the complete transient simulations compared to the continuous furnaces. Such a longer process time and problems regarding physical access to the heating chamber also require more attention in the instrumentation for the experimental measurements (Nima Bohlooli Arkhazloo et al., 2021).

Thus, the number of papers available in such a context is few and there is little information on the stacking pattern optimization of large-size blocks within real-scale heat treatment furnaces. The existing studies have been narrowed to investigations in the laboratory to semi-industrial medium-scale furnaces (Govardhan, Rao, & Narasaiah, 2011; Prieler, Mayr, Demuth, Spoljaric, & Hochenauer, 2015), or only to furnace medium analysis rather than simultaneous analysis of thermal interactions between the chamber medium and product (Galletti, Coraggio, & Tognotti, 2013; Singh, Talukdar, & Coelho, 2015). For instance, using CFD simulations, Filipponi et al. (Filipponi et al., 2016) investigated the effect of the door opening on the temperature distribution of unloaded batch-type gas-fired furnaces. The objectives of the reviewed literature were mainly focused on the temperature distribution of products in the conventional process rather than the subsequent optimization of the process. Among the rarely found studies on the optimization side, Palacio et al. (Palacio-Caro et al., 2020) used CFD simulations to present a detailed investigation of the influence of fans' rotational speed on the temperature uniformity of the product within an electrical convective heat treatment furnace. Díaz-Ovalle et al. (Díaz-Ovalle, Martínez-Zamora, González-Alatorre, Rosales-Marines, & Lesso-Arroyo, 2017) reported that the baffle plate geometry in an electrical convective furnace could have an important influence on the temperature uniformity of the furnace and the preheating time of the furnace. Using a 3D numerical model, Tan et al. (Tan et al., 2022) simulated the heat transfer during annealing in a vertical furnace to recommend design changes that would improve thermal uniformity across the stacked wafers. In the simulation, it was

found that the heat loss at the process door was greater than the heat loss at the top header. Their suggestions could lead to a reduction in heat loss and an improvement in the thermal uniformity of stacked wafers. Food industry researchers Amanlou et al. (Amanlou & Khoshtaghaza, 2018) developed numerical CFD models of a heating oven (cabinet dryer). In their work, they addressed the non-uniformity in the moisture content of the end product after the heat treatment. The CFD model simulated the airflow and temperature distribution inside the drying chamber, which is very similar to the challenges faced in steel industry furnaces. A similar study was carried out on a forced convection oven to investigate the isothermal airflow for a quick baking process by Ismail et al. (Ismail, Awonusi, & Akinoso, 2021). The results of their study demonstrated the importance of impeller placement in the performance of the oven. Using the commercial CFD software FLUENT, Fu et al. (Fu et al., 2019) developed an innovative approach to simulate the heating process of a superalloy workpiece in a laboratory-scale electric furnace. The model mainly focused on the heat generation rate of the energy source developed using a FLUENT user-defined function (UDF); a proportional integral derivative (PID) method was proposed to regulate furnace temperature according to the thermal scheme. Arkhazloo et al. (Bohlooli Arkhazloo et al., 2021), investigating the thermal interactions inside an industrial gas-fired furnace, reported the significant effect of stacking patterns (such as their relative locations and distances) on the uniformity of the tempering process. Such influence on the temperature uniformity of the product was also mentioned by Wang and Shang (Z. J. Wang & Shang, 2010) and Macchion et al. (Macchion et al., 2006) in their numerical studies of small-scale steel parts' heat treatment within a high pressure gas quenching chamber. According to Macchion et al. (Macchion et al., 2006), the temperature uniformity of the product was significantly affected by the position of parts within the furnace. Korad et al. (Korad, Ponboon, Chumchery, & Pearce, 2013) used steady-state CFD simulations to study the aluminum billet heat treatment inside a homogenization furnace. Their results indicated that the different billets experienced different temperature distributions as a result of the stacking pattern and their relative locations within the heating chamber.

However, up to now, little information has been available on the influence of stacking pattern parameters such as spacers and skid sizes on the temperature uniformity of large-size steel

parts within an industrial electrical heat treatment furnace. Therefore, the present study investigated the influence of stacking pattern parameters on the uniformity of large-size products' heat treatment process and their corresponding transient heating rates within an industrial electrical heat treatment furnace. Stacking pattern parameters and their relative positions were discussed using unsteady CFD simulations of the process. The three-dimensional (3D) CFD model of the electrical batch-type heat treatment furnace encompassed all the details of the 112 m^3 furnace, including axial fans, large-size forged blocks, and skids. Details of the numerical simulations, including initial and boundary conditions, were specified using experimental measurements, and the corresponding data were provided. Numerical predictions were validated using temperature measurements around instrumented 29-metric-tons large-size forged blocks during the heat treatment process. Results were analyzed and interpreted in terms of the conjugate heat transfer modes and their corresponding interactions related to the temperature distribution of large-size blocks due to the stacking pattern alterations.

3.2 Furnace Description

The present research was carried out on an industrial electrical heat treatment furnace located at Finkl Steel, Sorel, QC, Canada (Finkl Steel Inc., 2021). This batch-type car bottom furnace has two series of heating elements located on the two side walls of the heating chamber. Three axial fans are mounted on top of the furnace chamber to allow the flow of the hot air inside the chamber and around the blocks. These three fans, namely front, center, and back, have a constant rotational speed of 1750 rpm. The central fan rotates clockwise, while the other two fans have counterclockwise rotational directions, which are dependent on the fans' blades' angle. In these high temperature fans, air flows through the blades and parallel to the shaft on which the fans are mounted. A vertical distance of 1.27 m is between the axial fans and the heating elements. Figure 3.1 shows the electric furnace and its corresponding drawings, including the dimensions of the heating chamber and its details (such as skids, axial fans, and typical loading zone). Details of the fans and electrical heating elements, highlighted by red circles, can be seen in this figure. The internal dimensions of the heating chamber of the furnace

are 3.43 m, 4.11 m, and 8.02 m in the x, y, and z directions, respectively. Five steel skids with a cross-section of 0.27 m × 0.27 m and a length of 3.05 m are placed to locate the large forged blocks on the car bottom furnace. Fans circulate fluid flow to heat the products, and the furnace has no exhaust. The furnace walls are covered using refractory ceramic fibers with a thickness of 0.254 m and a thermal conductivity of 0.16 W/(m·K) at 538 ^{o}C (corresponding to the tempering temperature).

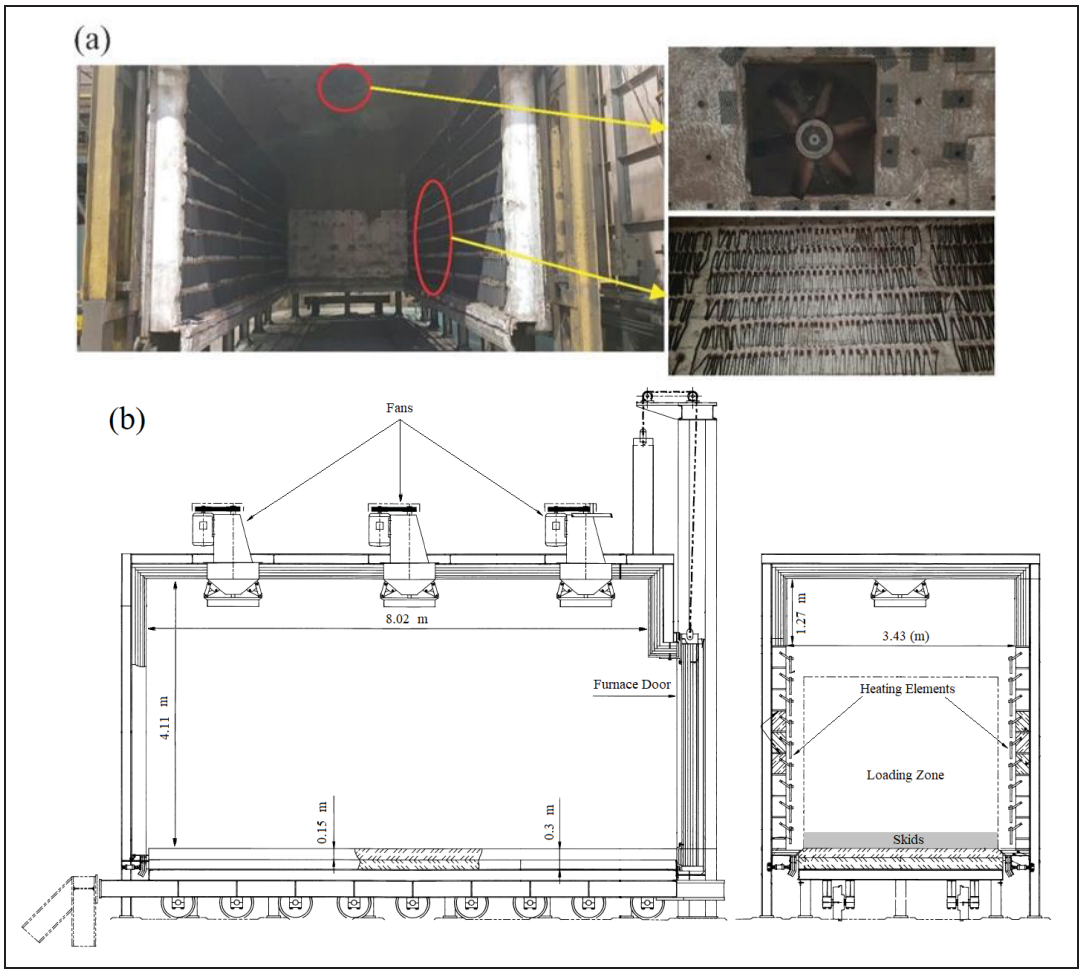

Figure 3.1 (a) Car bottom electrical furnace and (b) its corresponding drawings and dimensions

3.3 Stacking Patterns

Two main configurations (configs) of stacking with different forging sizes were considered for the analysis:

- **Config-1:** This stacking pattern consisted of two large-size rectangular parallelepiped-shaped forgings with the dimensions of 1.34 × 0.66 × 4.25 m^3 and 1.27 × 0.63 × 4.6 m^3, named hereafter as upper and lower blocks, located on the car bottom of the furnace. Config-1 provides an insight into the heat treatment of high thickness forgings in this furnace.
- **Config-2:** Three stacked blocks with the corresponding dimensions of 1.2 × 0.25 × 4.36 m^3, 1.2 × 0.25 × 3.88 m^3, and 1.2 × 0.25 × 4.2 m^3, called upper, middle, and lower blocks, respectively, were used to evaluate the stacking pattern effect on the heat treatment of blocks.

These two configs were subjected to the usage of several spacer and skid sizes to evaluate their effect on the temperature uniformity of the products. The following secondary level naming format was used to refer to each case under investigation:

- **-S5**, **-S12**, **-S17**, and **-S25**: Referring to the cubic spacer sizes of 0.05 × 0.05 × 0.05 m^3, 0.12 × 0.12 × 0.12 m^3, 0.17 × 0.17 × 0.17 m^3, and 0.25 × 0.25 × 0.25 m^3, respectively.
- **-DSK:** To identify the effect of double-size skids on the analysis.

Figure 3.2 represents the discussed blocks in the two defined configs located on the car bottom of the electrical furnace with -S5 spacers.

Figure 3.2 Industrial scale stacking patterns: (a) Config-1-S5 and (b) Config-2-S5

3.4 Experimental Measurements

Temperature measurements were conducted using five pre-calibrated (Engineering, 2022) K-type thermocouples (TC) with a stainless steel sheath. These TCs were positioned in different locations of the forgings' surfaces in Config-1. Figure 3.3 depicts the industrial scale experimental setup and its corresponding schematic view. Thus, "L" and "l" are the lengths of the lower block and upper block, respectively, "H" is the height of the lower block, and "w" is the width of the upper block. Details regarding the methods developed for reliable data acquisition were published in a recent article by Arkhazloo et al. (N. B. Arkhazloo et al., 2019). Figure 3.4 displays the transient history of the electrical energy usage profile at 600 V and 60 Hz power by the loaded furnace during the heat treatment process.

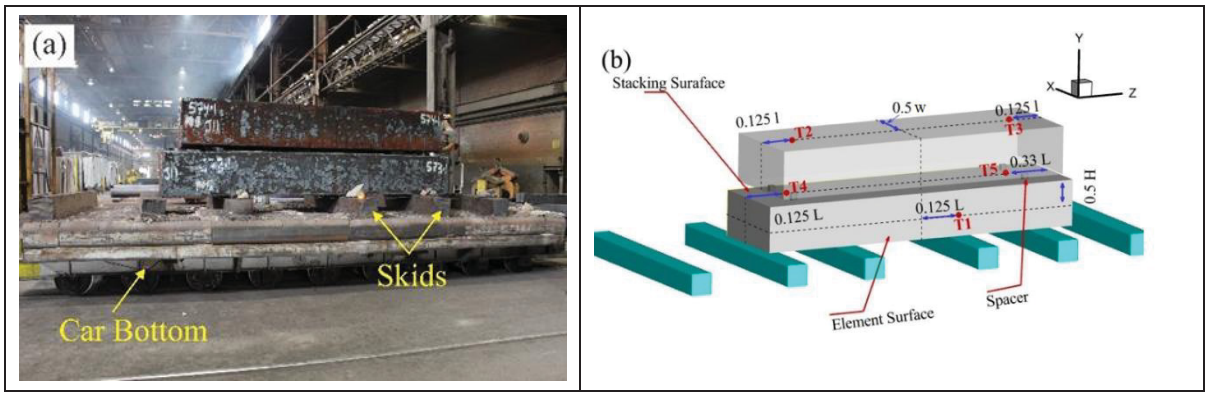

Figure 3.3 Experimental setup details including (a) real-scale experimental configuration and (b) a schematic view of five thermocouples' locations (T1-T5)

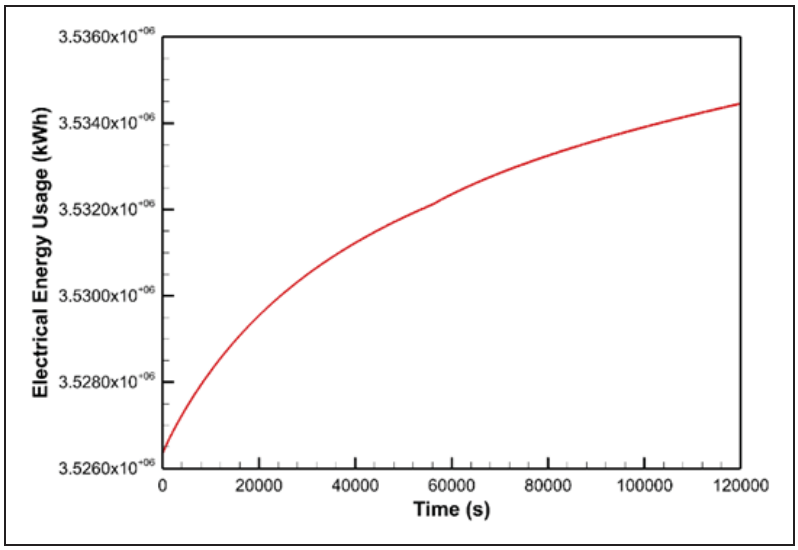

Figure 3.4 Transient history of electrical energy usage profile versus time, at 600 V and 60 Hz power consumed by the heating elements in the furnace

3.5 Computational Details

3.5.1 Governing Equations

A transient CFD simulation with a multiple reference frame (MRF) model was used to solve the Reynolds-averaged Navier-Stokes equations. Generally, MRF transforms the fluid

equation of motion to a rotating frame so that the steady-state solutions for the rotating frame are possible. This model can be applied to a steadily rotating part of a domain with constant rotational speeds. The method was reported to be reliable, especially in cases where the flow outside of the rotating frame is of interest (ANSYS Inc., 2023). In the current study, the computational domain was divided into three rotating references (three fans with a constant rotational speed of 1750 rpm) and one stationary frame (furnace chamber outside the region of the fans, including blocks). The governing equation of fluid flow for fan zones in absolute velocity formulation is as follows:

$$\frac{\partial \rho}{\partial t} + \nabla.(\rho \vec{v}_r) = 0 \tag{3.1}$$

$$\frac{\partial}{\partial t}(\rho \vec{v}_r) + \nabla.(\rho \vec{v}_r \vec{v}) + \rho(\vec{\omega} \times \vec{v}) = -\nabla \mathrm{p} + \nabla.\bar{\bar{\tau}} + F \tag{3.2}$$

$$\frac{\partial}{\partial t}(\rho E) + \nabla.(\rho \vec{v}_r H + p\vec{u}_r) = \nabla.(k\nabla \mathrm{T} + \bar{\bar{\tau}}.\vec{v}_r) + S_h \tag{3.3}$$

where, $\vec{v}_r$ and $\vec{u}_r$ are defined as a function of $\vec{r}$ (position vector of a point from the origin of the rotating frame), as follows:

$$\vec{v}_r = \vec{v} - \vec{u}_r \, , \vec{u}_r = \vec{\omega} \times \vec{r} \tag{3.4}$$

The rotational speed for the furnace chamber (except the rotating fans at 1750 rpm) is equal to zero ($\omega = 0$), which results in stationary forms of equations. It should be mentioned that a local reference frame transformation is considered for the flow variables at the interface between the zones to have consistent predictions of fluxes. However, scalars, including temperature and pressure, are passed without changes. The turbulence induced by the fan rotations was simulated using the Realizable k-ε model. It has been reported that this model has shown good agreement with experimental observations in heat treatment processes (Nima Bohlooli Arkhazloo et al., 2021).

Finally, the surface-to-surface (S2S) model was employed to compute the radiation heat transfer to the blocks from the furnace medium, skids, and adjacent blocks within the heat treatment chamber. In this model, the radiative heat transfer equation is simplified by considering only the surface-to-surface radiation, as follows: (i.e., ignoring the medium's absorption, emission, or scattering effect on the radiation heat transfer) (ANSYS Inc., 2023).

$$q_{out,k} = \varepsilon_k \sigma T_k^4 + \rho_k \sum_{j=1}^{N} F_{kj} q_{in,k} \tag{3.5}$$

where, $q_{out,k}$ is the energy flux leaving the surface k and $q_{in,k}$ is the energy flux incident on the surface from the surroundings. ε_k, ρ_k, and T_k are the emissivity coefficient, reflection coefficient, and temperature of surface k, respectively. F_{kj} is defined as the view factor between surface k and surface j, and σ is the Stefan-Boltzmann constant.

3.5.2 Model Description

Simulations were carried out using ANSYS FLUENT 2022 R2 software, based on the finite volume method applying the unsteady SIMPLE algorithm (Versteeg & Malalasekera, 2007) to non-uniform hexahedral computational grids. A schematic view of the computational domain, including the boundary conditions and details of the heating chamber corresponding to the experimental measurements, is also presented in Figure 3.5. Three sets of meshes including 758,000, 3,155,000, and 10,576,000 cells, named coarse, medium, and fine mesh, respectively, were created to verify the independence of results from mesh size. It was found that the medium mesh performed reasonable predictions compared to the fine mesh, and the prediction differences were negligible. Therefore, the medium case with 3,155,000 cells was employed for the rest of the simulations. An average heat loss of 594 W/m^2 was applied to the furnace walls. This value was calculated in accordance with the approach proposed by Hadala et al. (Hadała et al., 2017). Standard wall functions were applied to the no-slip condition walls, including furnace walls and forgings surfaces. The steel blocks' surface emissivity (ε) was set to 0.8, while an emissivity of 0.75 was considered for the furnace refractories. The effect of

heating elements was considered using transient heat flux through the side walls. Transient temperature-dependent thermophysical properties of the materials were calculated using the JMatPro 11 software (SenteSoftware). The steel under investigation was a high strength medium carbon steel-modified P20. It should be mentioned that during the transient calculations, each time step continued up to a convergence of 10^{-5}, 10^{-6}, and 10^{-9} for the continuity, energy, and radiation equations, respectively.

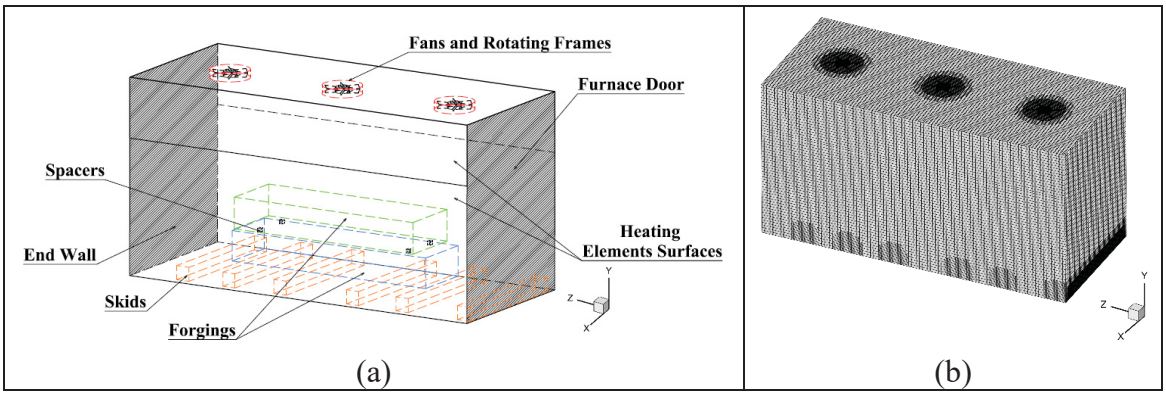

Figure 3.5 (a) The computational domain including solid zones, walls, heating elements surfaces, fans, and rotating frames, and (b) computational grids

3.6 Results and Discussion

3.6.1 Validation

The measured transient temperatures of the forged blocks' surfaces at different TCs locations and the corresponding CFD model predictions are represented in Figure 3.6. It can be seen that there is a noticeable difference between the transient temperature histories of different TCs during the heat treatment process, which will be discussed in detail in the following subsections. The CFD predictions showed reliable consistency as compared to the measurements. The results of the CFD model predictions at the TCs locations displayed a very good agreement with a maximum average of about 6.62% deviation compared to the experimental measurements. Owing to the consistency between the predictions and measurements, it can be concluded that the CFD model with the MRF, which requires a lower

computational cost and inherits a better converging trend compared to the dynamic mesh modeling, was reliable in the context of the present study. Therefore, this model was employed to evaluate the influence of different stacking patterns and spacer sizes on the heating history of the large-size blocks in the application under investigation.

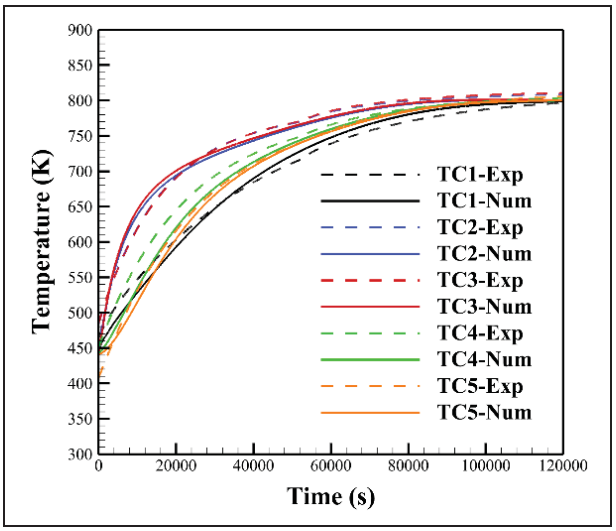

Figure 3.6 Validation of CFD simulations with the MRF model

3.6.2 Config-1 Analysis

The transient evolution of maximum temperature non-uniformities of large-size blocks during the heat treatment process in Config-1 is shown in Figure 3.7. The maximum temperature non-uniformity (Delta T) was defined as an instantaneous temperature difference between two points on the surfaces of the blocks, which experienced the maximum and the minimum temperatures, respectively. It can be seen that both blocks experienced significant non-uniformities during the heat treatment process. Such non-uniformity was also reported for gas-fired furnaces (Bohlooli Arkhazloo et al., 2021). This temperature non-uniformity is not usually considered in metallurgical investigations of the heat treatment process, where the main attention is concentrated on the temperature gradient between the center and the surface of the block. It can be observed that the curves had an increasing trend up to 0.1 of the total heat treatment time (t/t_T~0.1) when the maximum non-uniformities of 195 K and 200 K were

produced around the lower block and upper block, respectively. Then, the non-uniformities were reduced to a certain level at the end of the process, at which the furnace and block were held at the isothermal tempering temperature of 800 K. However, it should be noted that such non-uniformities were experienced even after 6 h of tempering (by about 176 K for the lower block) and could significantly affect the mechanical properties of the final product from one end of the product to another.

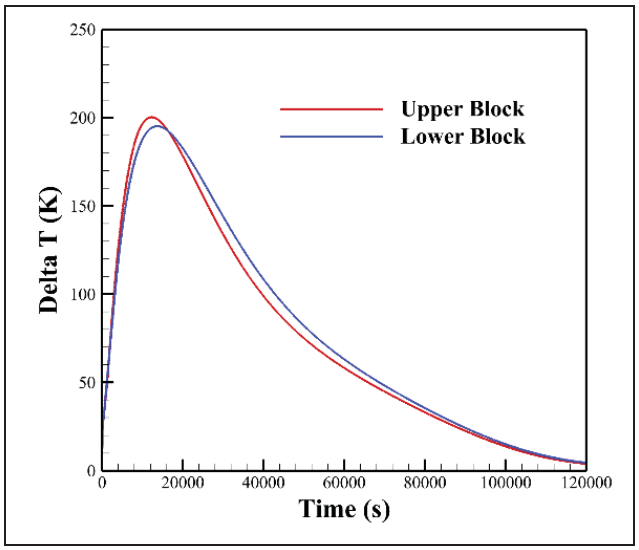

Figure 3.7 Transient temperature non-uniformities experienced by different blocks of Config-1-S0 during the heat treatment process

To determine the effect of spacer usage on the temperature distribution of blocks during the process, contours of the temperature distribution at the central cross-section of the blocks in Config-1-S0 and Config-1-S5 at t/t_T = 0.1, when the maximum non-uniformities were identified, are depicted in Figure 3.8. From Figure 3.8a, for Config-1-S0, both blocks experienced an uncommon temperature gradient from different surfaces to the center of the block. Ideally, it is expected that the blocks have a uniform increasing temperature from the center to the surface of the block with approximately the same temperature at equal depths.

However, results not only showed that the different surfaces of the blocks followed different temperature patterns, but that the minimum temperature was also not located at the center of

the block, but shifted toward the blocks' stacking surfaces. This was more evident in the upper block, whose minimum temperature was located on its lower surface (stacking surface). It could be seen that in this block, a reducing temperature gradient occurred from the upper left and upper right corners toward the lower surface. Furthermore, a similar trend was found for the lower block, the minimum temperature of which was identified at the upper surface. Such an irregular temperature gradient for the large-size blocks was also reported by Arkhazloo et al. (Nima Bohlooli Arkhazloo et al., 2021) for heat treatment within a gas-fired furnace. According to (Nima Bohlooli Arkhazloo et al., 2021), although the unloaded gas-fired furnace was uniform during the conventional uniformity test, blocks showed significant temperature non-uniformities after loading and during the heat treatment process of products. The reason was due to the size of the products, which extremely affected the furnace flow field, including vortical structures and thermal boundary layers. Given the temperature uniformity of the unloaded furnace in the present study, it can be said that the similar effect of large-size products on the fluid flow circulation within the electric furnace is the reason behind the identified temperature non-uniformities.

The results indicate that using -S5 spacers contributes to shifting the coldest point toward the blocks' center and reduces the sharp temperature gradient at this cross-section compared with Config-1-S0. In addition, the use of spacers appears to result in higher temperatures at the block center (shrinkage of contour's minimum level) in Config-1-S5 compared to Config-1-S0. Therefore, it can be said that not only could the spacers contribute to the uniformity of the temperature distribution during the heat treatment process, but they also result in higher heating rates compared to the conventional stacking method without spacers.

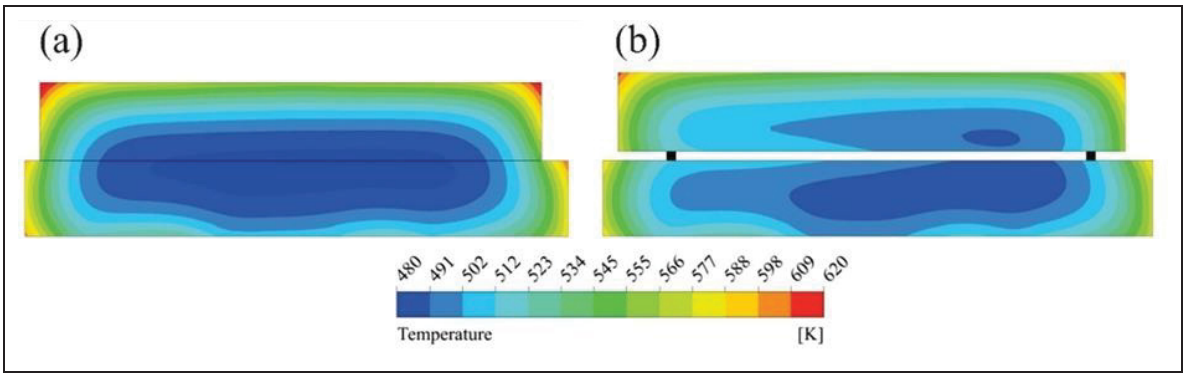

Figure 3.8 Contours of temperature distribution at the central cross-section of blocks at t/t_T = 0.1 (a) Config-1-S0 and (b) Config-1-S5

The influence of the spacer size on temperature uniformity was also investigated. The results are presented in Figure 3.9, where the transient history of block non-uniformities in Config-1 is compared for different spacer sizes. It can be seen that there is a significant reduction in the maximum temperature non-uniformities of blocks (peak of the non-uniformity curves) as a result of spacer usage. The data presented in Figure 3.9 also shows that even small spacers (-S5) could considerably reduce the maximum non-uniformities by about 19% and 23% for the upper and lower blocks, respectively. However, it is interesting to note that larger spacer sizes would not always lead to a reduction in the maximum non-uniformities because they could also act as heat sinks. Hence, depending on the size and mass of the spacers, they can lead to a local temperature non-uniformity. For instance, the maximum non-uniformity of the lower block (Figure 3.9a) for the -S12 and -S25 cases are higher than those of -S5 and -S17, respectively. Therefore, although an increase in the spacer size from -S5 to -S17 resulted in a reduction of temperature non-uniformity by about 11%, the increase in the spacer size from -S5 to -S12 increased the maximum temperature non-uniformity of the products. In this stacking pattern, it could be said that the -S17 showed the optimum efficiency characterized by the minimum temperature non-uniformities around the blocks.

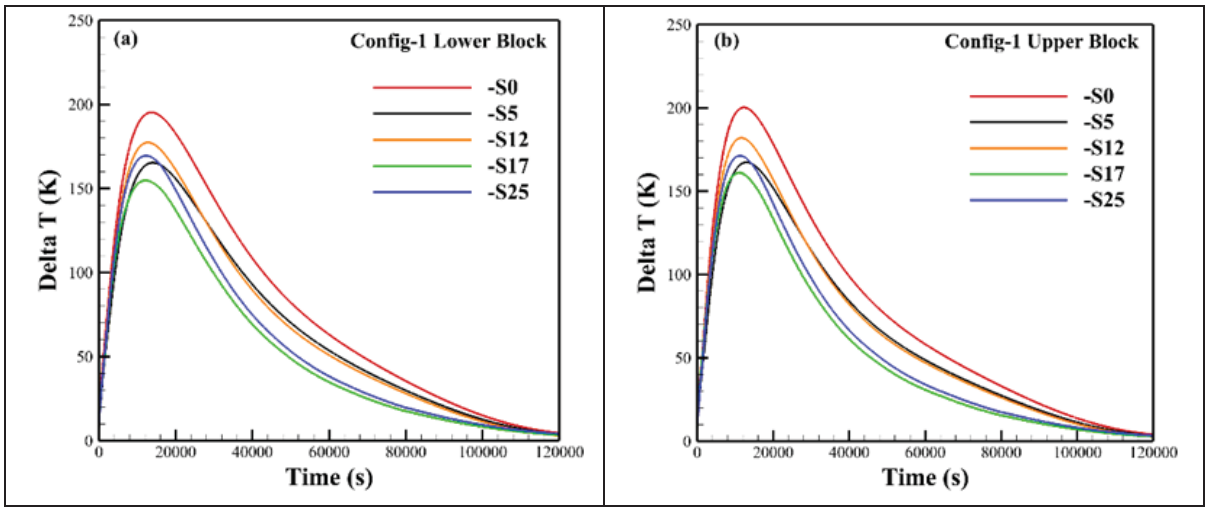

Figure 3.9 Effect of spacer size on temperature non-uniformities of products in Config-1: (a) lower block and (b) upper block

In addition, the area under each curve in Figure 3.9 represents the total non-uniformity that a block experienced during the heat treatment process. In other words, the differences between the area under the curves determine the difference between the total transient temperature non-uniformities experienced by the blocks. Table 3.1 presents the total temperature non-uniformity reductions due to the usage of different spacer sizes compared to Config-1-S0.

Results in Figure 3.9 and Table 3.1 show that the area under cases with spacers were clearly contracted compared to Config-1-S0. It should be noted that these contractions were not only on the peak areas of the curves, but also on the secondary descending part of the curves when the blocks were at higher temperatures (close to the target tempering temperatures). Therefore, the positive effect of spacers is not just about the early stage of the process, but is rather evident throughout the entire process. Analysis of the obtained results indicated that the maximum shrinkage belonged to the -S17, with about a 23% and a 26% reduction compared with -S0 for the upper and lower blocks, respectively. It can be seen that the -S17 with both reduction on the peak and tail of the curve could present more effective performance compared to the other spacers.

Table 3.1 Total temperature non-uniformity reduction of blocks with different spacer sizes in Config-1 compared to Config-1-S0

Products	-S5	-S12	-S17	-S25
Lower Block	16%	12%	26%	22%
Upper Block	12%	9%	23%	19%
Average Effectiveness	14%	10.5%	24.5%	20.5

The positive effect of spacers could be discussed by considering different heat transfer modes during the process. Specifically, the presence of the spacers contributes to better fluid flow circulation within the heating chamber and around the blocks. This circulation around the block and specifically around the stacking surfaces results in the accession of convection heat transfer at those specific surfaces. Furthermore, the space between the blocks enhances the absorbed radiation heat from the furnace chamber by those surfaces due to scaling up on the radiation shape factor. Given the temperature ranges, it could be said that the convection heat transfer contribution to the reduction of temperature non-uniformity is mostly related to the peak reduction at the early stage of the process. Because at the early stage of the process, both the furnace atmosphere and blocks are at lower temperatures, the effect of radiation heat transfer is minor. On the other hand, it can be said that the positive contribution of spacers on the accession of radiation heat transfer is correlated to the secondary part of the curves, in which the area under the tails of the graphs were contracted. Therefore, the superposition of the introduced convection and radiation heat fluxes to the stacking surfaces using spacers results in a reduction of identified temperature non-uniformities compared to those of the conventional stacking pattern (Config-1-S0).

3.6.3 Config-2 Analysis

The temperature distribution contours of the central cross-section of the three blocks in Config-2-S0 and Config-2-S5 are depicted in Figure 3.10. The temperature distribution non-uniformities around the blocks are more significant for Config-2-S0, as compared with Config-1-S0, where the three blocks were loaded on the furnace. Contours reveal that the middle block faced an adverse tempering situation in which the block surfaces experienced lower

temperatures than the center of the block. Considering the fact that the block's surface areas (upper and lower surfaces) were exposed to a higher cooling rate in the previous step (quenching in water), such an adverse situation could considerably change the metallurgical transformation during the tempering, which should be prudently taken into consideration since this situation is not in accordance with what is expected from the metallurgical point of view for the design of the optimum heat treatment process. A similar trend was also found for the lower and upper blocks, where the minimum temperatures were close to the stacking surfaces, and significant temperature differences were predicted around the blocks. However, it can be seen that the use of spacers in Config-2-S5 resulted in better temperature distribution, and the very low temperature area (blue contours) in the middle block was contracted in Config-2-S5 (Figure 3.10b). Although the temperature uniformity in Config-2-S5 is not ideal, the minimum temperature, in this case, was shifted toward the center of the block, which is desirable for heat treatment accuracy.

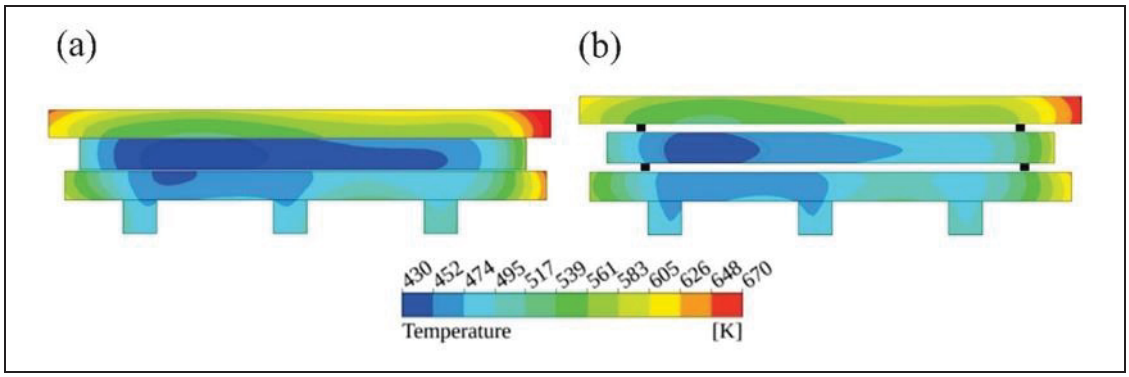

Figure 3.10 Temperature distribution at the central cross-section of (a) Config-2-S0 and (b) Config-2-S5

In the case of Config-2-S0, the blocks were located near the furnace's door. Due to this, the minimum temperatures were shifted toward the left side (furnace door), where the door blocked the fluid flow of the furnace. In addition, the effect of skids on the temperature distribution of the lower block can be clearly identified in this figure. The coexistence of the low temperature areas in this block and skids illustrates the effect of skids on the discussed temperature distribution map. This effect can be evidently recognized for both cases in Figure

3.10. Therefore, in this configuration, the stacking of blocks not only affected the blocks' temperature distribution, but their corresponding orientations with respect to the heating chamber details (i.e., door and skids) also affected the heating thermography.

Another significant fact that should be considered in the results presented in Figure 3.10a is that the upper block had higher temperatures (i.e., heating rates) compared with the lower and central blocks. This is in contrast to what is expected in an optimum heat treatment process in which uniform and equal heating rates are required for all the blocks in one batch of forgings. Therefore, not only did each block in Config-2-S0 have irregular and significant temperature non-uniformities, but the blocks had completely different heating histories. Such a situation could lead to the rejection of a block in this stacking setup after post-heat treatment inspections. On the other hand, it can be seen that the -S5 spacers in Figure 3.10b could help in this matter by reducing the temperature difference between the blocks. Nonetheless, because the existing non-uniformities could impact the blocks' final mechanical properties, further evaluation of the spacer and skid sizes should be conducted.

The transient evolution of temperature non-uniformity curves of three blocks for Config 2-S0 are shown in Figure 3.11. Similar trends to those for the large blocks in the Config-1-S0 are observed. However, a comparison of the maximum non-uniformities of blocks in both cases displayed that the blocks in Config-2-S0 experienced higher temperature non-uniformities. The data analysis in Figure 3.11 shows that the upper, center, and lower blocks had maximum temperature non-uniformities of 299 K, 379 K, and 337 K, respectively. In other words, although the blocks in Config-2-S0 had smaller dimensions compared to the blocks in Config-1-S0, they experienced more temperature non-uniformities from one end to the other. Such a level of temperature non-uniformity could be related to the loading cycle (i.e., three loads vs. two loads) and also to the orientation of blocks with respect to the furnace details within the heating chamber.

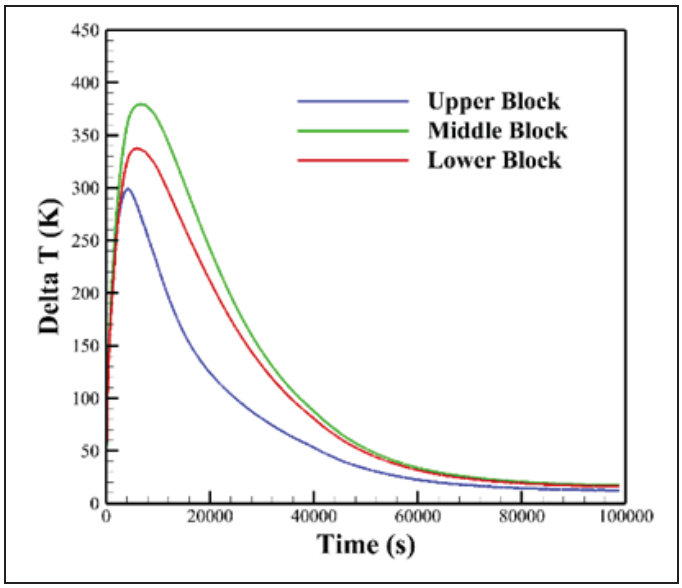

Figure 3.11 Transient histories of blocks' temperature non-uniformities in Config-2-S0

The comparative curves of temperature non-uniformities as a result of five different spacer sizes used in Config-2 are illustrated in Figure 3.12. The corresponding total temperature non-uniformity reduction values compared to Config-2-S0 are presented in Table 3.2. The results of Figure 3.12 prove the positive effect of spacers on the reduction of temperature non-uniformity peaks in Config-2. The maximum temperature non-uniformities as a result of the -S5 spacer usage were reduced from 299 K, 379 K, and 337 K for the upper, middle, and lower blocks (in the -S0 setup) to 205 K, 237 K, and 246 K, respectively. It can be seen that similar to Figure 3.9, -S12 and -S25 had lower effectiveness compared to -S5 and -S17, respectively. Furthermore, -S17 displayed the best performance among all the other spacers, with an average temperature non-uniformity reduction of 34% compared to Config-2-S0 (see Table 3.2). This is in accordance with the good performance of -S17 for the first stacking setup in Config-1. Thus, it can be said that -S17 is the optimum spacer size among the sizes studied for tempering in the present investigation.

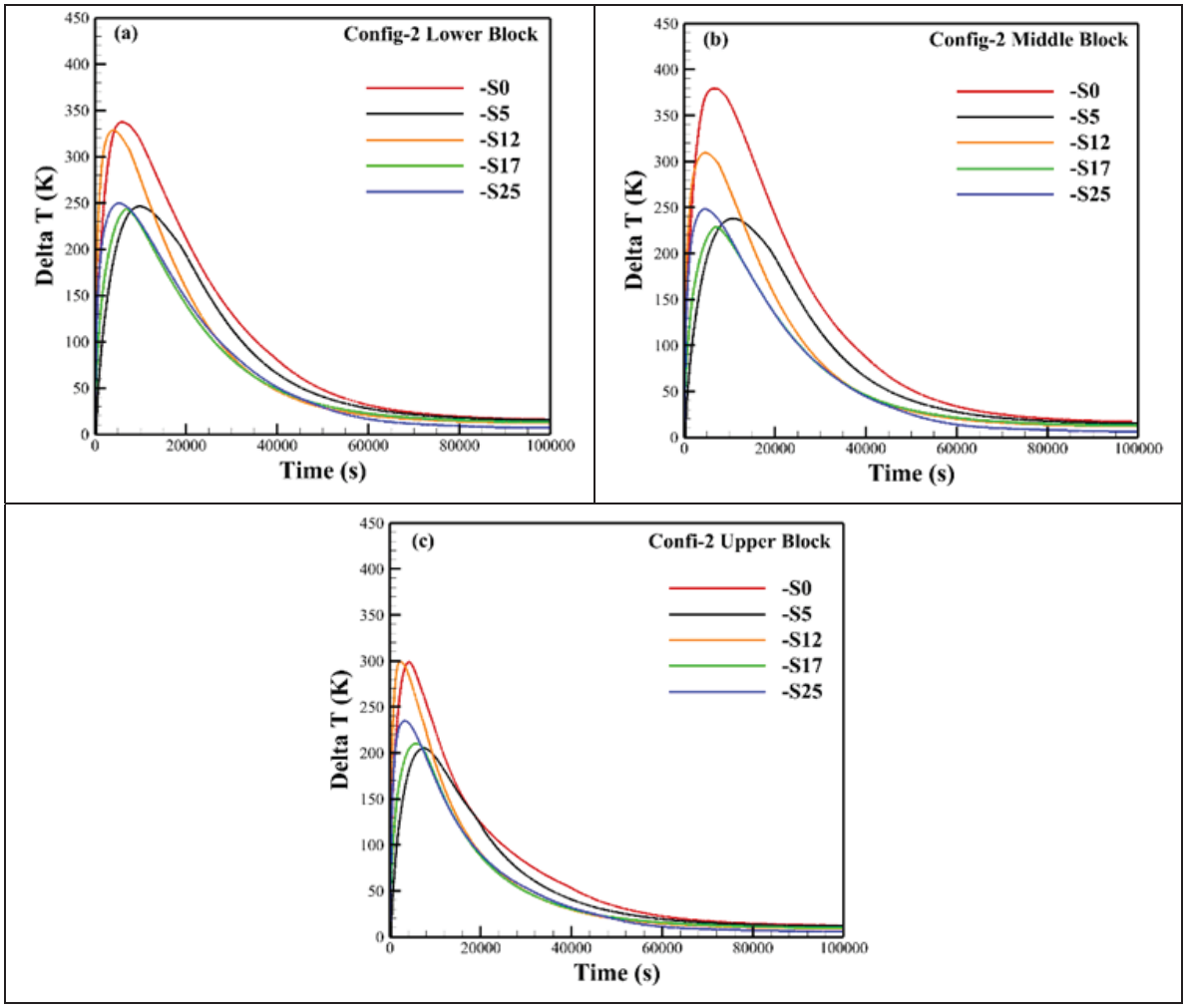

Figure 3.12 Effect of spacer size on temperature non-uniformities of products in Config-2: (a) lower block, (b) middle block, and (c) upper block

Table 3.2 Total temperature non-uniformity reduction of blocks with different spacer sizes in Config-2 compared to Config-2-S0

Products	-S5	-S12	-S17	-S25
Lower Block	21%	17%	32%	28%
Middle Block	29%	27%	40%	35%
Upper Block	19%	17%	30%	26%
Average Effectiveness	23%	20.3%	34%	29.6%

Furthermore, a comparison of the predictions presented in Figure 3.11 and Figure 3.12a,b indicates that although the middle block in Config-2-S0 experienced the maximum non-uniformities, the usage of spacers imposed a situation in which the middle block experienced significantly lower temperature non-uniformities. It can be seen that in the spacer-imposed setups, the lower and middle blocks experienced fairly similar non-uniformities, resulting in a similar heat treatment for the batch of forgings in the furnace.

3.6.4 Effect of the Double-Size Skid on the Heat Treatment Process

The effect of skid size on the temperature uniformity of blocks during the heat treatment process is illustrated in Figure 3.13.

Figure 3.13a and Figure 3.13b indicate that the use of a double-size skid in the heat treatment process of Config-1 led to a significant reduction of the identified maximum temperature non-uniformity (peak of the curves) and the total non-uniformities (areas under the curves) of both the lower and upper blocks. Analysis of the corresponding data reported in Table 3.3 shows that the double-size skid resulted in a 5% reduction for -S17 and an average of 14% reduction for the -S5 setups in Config-1. It can be said that the double-size skid contributes to better temperature uniformity by reducing the distance between the fans and the forgings. The effectiveness of such alteration is more significant for the -S5. Therefore, considering the practical difficulties of using -S17 in the production routines, the Config-1-S5-DSK could be effectively used for the heat treatment of large-size products.

Table 3.3 Effect of the double-size skid on temperature non-uniformity reduction of blocks in Config-1 compared to Config-1-S0

Products	-S5	-S5-DSK	-S17	-S17-DSK
Lower Block	16%	29%	26%	31%
Upper Block	12%	27%	23%	28%
Average Effectiveness	14%	28%	24.5%	29.5%

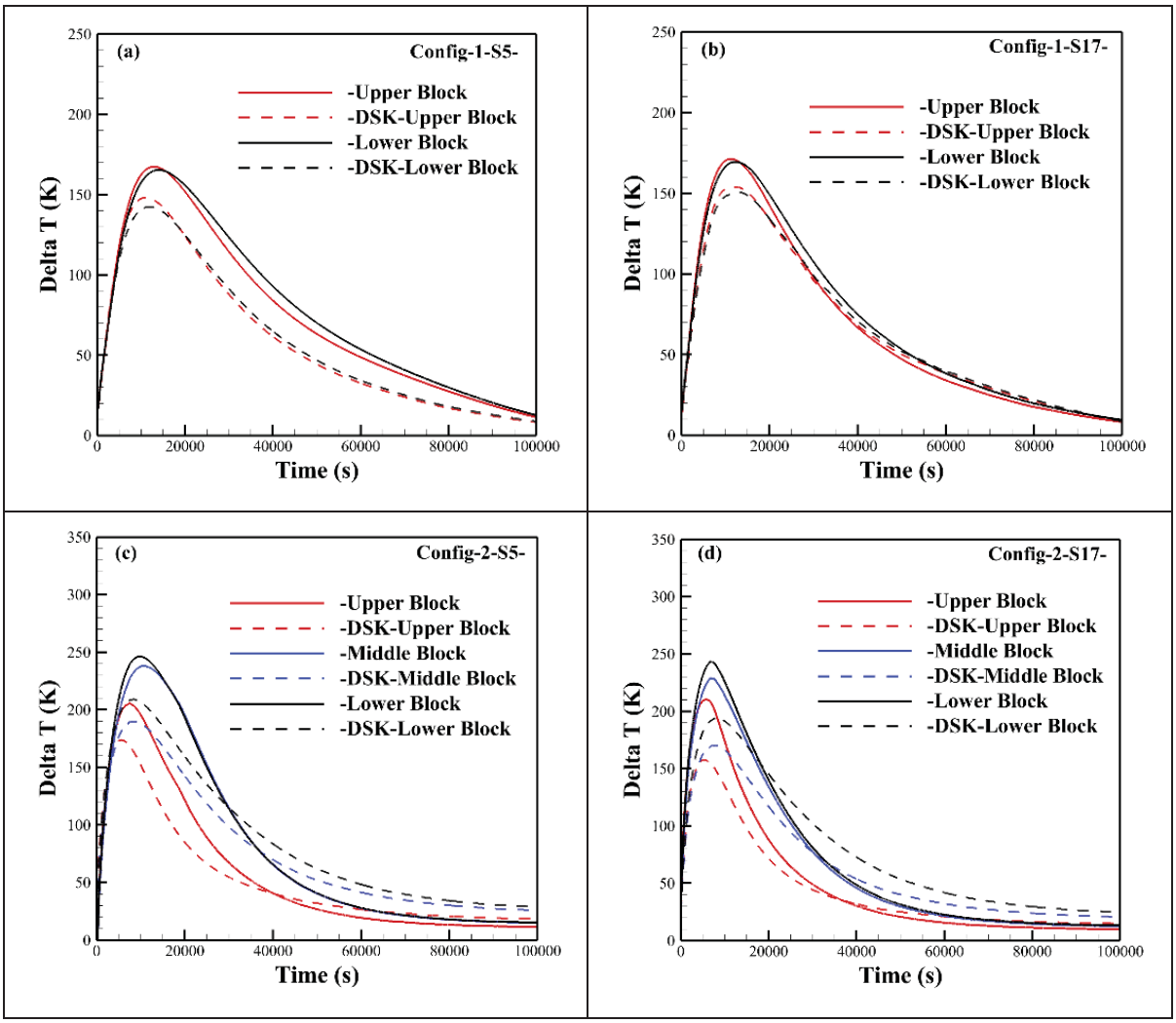

Figure 3.13 Double-size skids effect on temperature non-uniformities of products in (a) Config-1-S5, (b) Config-1-S17, (c) Config-2-S5, and (d) Config-2-S17

In addition, Figure 3.13 c and d, together with Table 3.4, demonstrate that -DSK had different impacts on the temperature uniformity of the heat treatment in Config-2. It is observed that the usage of double-size skids first resulted in changes in the sorting of loads with respect to the maximum identified temperature non-uniformities. In the case of -DSK stacking, the lower block experienced higher temperature non-uniformities than the other blocks. This is in contrast with what was identified for Config-2-S0 (see Figure 3.11), where the middle block had the maximum non-uniformities, and Config-2-S5 and S-17, for which both the middle and lower blocks had a similar temperature non-uniformity (refer to Figure 3.12). This can be

related to the diameter ratio of the spacer and skids with respect to the blocks. In Config-2, the ratio of skid diameter to the block thickness is higher than those of Config-1, where the large-size blocks are loaded. In Config-2, the lower block, which is in simultaneous contact with spacers and double-size skids, tolerated more severe temperature non-uniformities. In other words, although the -DSK results in the reduced distance between the fans and therefore provides better temperature uniformity, the high amount of added mass to the setup negatively affects the temperature uniformity of the lower block. This is because of the fact that the double-size skids in Config-2 act like an extra loading, which in turn resulted in the stacking non-uniformity phenomenon. From Figure 3.13c,d, it can be seen that although the lower block experienced lower values of temperature non-uniformities in the peak area (by about 10%), higher temperature non-uniformities (16%) were observed later on toward the end of the process, resulting in a total of a 3% increase in temperature non-uniformities for this block.

However, -DSK in Config-2 positively contributed to reducing the temperature non-uniformities for the middle and upper blocks. Therefore, although -DSK could contribute to the reduction of temperature non-uniformities of the stacked blocks in both configurations, its employment should always be in parallel with the consideration of the skid diameter to block diameter for the lower block, which is in direct contact with the skids. In other words, -DSK can be effectively used for heat treatment when the larger block is loaded as the lower block in the configuration.

Table 3.4 Effect of the double-size skid on temperature non-uniformity reduction of blocks in Config-2 relative to Config-2-S0

Products	**-S5**	**-S5-DSK**	**-S17**	**-S17-DSK**
Lower Block	21%	18%	32%	28%
Middle Block	29%	35%	40%	45%
Upper Block	19%	28%	30%	37%
Average Effectiveness	23%	27%	34%	36.6%

3.7 Conclusions

A numerical analysis of the effect of the stacking pattern on the temperature uniformity of the high-strength steel parts during the heat treatment process within an industrial electrical furnace was performed. The 3D CFD model of the furnace, validated by real-scale experimental measurements, was employed to examine the effects of different spacers and skid sizes on the temperature uniformity of the products. Both convection and radiation heat transfer modes in a turbulent flow field of the heating chamber were taken into consideration. Two different setups of stacked forgings with different large-scale block sizes were used to increase the applicability of the present findings to the real practice of the heat treatment process in industrial sections. It was shown that using spacers of different sizes could affect temperature distribution at different stages. The optimum spacers-skids combination was determined for each configuration. The main conclusions of the investigation are summarized as follows:

1. The transient CFD model with MRF computation, covering practical details of the furnace, can be a reliable representative of the furnace under investigation. It is shown that the 3D CFD model predicted the transient temperature of the large-size blocks by a maximum average of 6.62% deviation during the heat treatment process.
2. It was shown that maximum temperature distribution non-uniformities of up to 200 K and 373 K could exist in the case of two rows and three rows of blocks stacked, respectively.
3. The effective usage of the spacers could significantly reduce the temperature distribution non-uniformities of the blocks by up to an average of 34% for the optimum spacer size.
4. The -S17 spacer size was identified as the optimum spacer size for both the large-size blocks and blocks stacking in this setup of materials.
5. The double-size skid could be effectively used for the heat treatment process, particularly when it comes to the stacking of large-size blocks. Using this approach could increase the average effectiveness of temperature uniformity for large products by a maximum of 14%.

6. An adverse influence of the double-size skid was found for the heat treatment of the low thickness blocks.
7. The present CFD model and experimental data are applicable to the optimization of a furnace design and the operational conditions of industrial heat treatment furnaces.

Author Contributions: S.M.: conceptualization, methodology, software, validation, formal analysis, investigation, resources, data curation, writing—original draft preparation, writing—review and editing, visualization. N.B.A.: conceptualization, methodology, software, validation, formal analysis, investigation, data curation, writing—original draft preparation, writing—review and editing, visualization. F.B.-T.: supervision, methodology, formal analysis, writing—review and editing. J.-B.M.: conceptualization, investigation, supervision, resources, formal analysis. A.L.: investigation, resources, formal analysis, writing—review and editing. M.J.: conceptualization, methodology, supervision, formal analysis, writing—review and editing. All authors have read and agreed to the published version of the manuscript.

Funding: This work was funded by the Mitacs in the framework of [IT27097, IT03151] Grants.

Data Availability Statement: Not applicable.

Acknowledgments: The authors would like to extend their gratitude to Finkl Steel, especially its research and development and heat treatment departments, for providing the large blocks as well as the instrumentation and measurements used in these studies.

Conflicts of Interest: The authors declare no conflict of interest.

CHAPTER 4

INFLUENCE OF HEATING ELEMENTS LAYOUT ON TEMPERATURE UNIFORMITY IN A LARGE SIZE HEAT TREATMENT FURNACE

Sajad Mirzaei [a], Nima Bohlooli Arkhazloo [a], Jean-Benoit Morin [b], and Mohammad Jahazi [a]

[a] Département de Génie Mécanique, École de Technologie Supérieure, Montréal, Quebec, Canada H3C 1K3
[b] Finkl Steel Inc., 100 McCarthy, Saint-Joseph-de-Sorel, Quebec, Canada J3R 3M8

Paper published in *Case Studies in Thermal Engineering*, September 2024

Abstract

Computational Fluid Dynamics simulations were used to optimize heating elements placement on the walls of a large-size electrical heat treatment furnace in order to reduce temperature gradients within the furnace and uneven temperatures on different faces of the blocks which could result in variabilities in final mechanical properties. Initial evaluations of different layouts highlighted the effectiveness of equipping two side walls. Subsequently, an optimal percentage of side wall coverage was identified through simulations and multi-objective evolutionary optimization. Genetic and Pareto search algorithms yielded 10% and 14.2% as optimum values, respectively. Implementing an optimal coverage demonstrated significant reductions in surface temperature non-uniformity, surface-to-center temperature differential, and temperature differences between loaded blocks. These improvements suggest a potential for enhanced uniformity in mechanical properties across a batch of products. This approach presents a promising strategy for obtaining consistent and efficient heat treatment cycles in industrial heat treatment furnaces resulting in energy saving and improved product quality.

Keywords: Industrial electric furnace, heat treatment, temperature uniformity, optimization, heating elements placement, CFD simulation.

4.1 Introduction

Large-size furnaces are widely used in industry for the heat treatment of all kinds of alloys (superalloys, aluminum alloys, steels, etc.). The largest number of such furnaces are found in the steel industry because of the extensive use of steel when compared to other alloys. Most, if not all, steel products go through one or several heat treatment cycles and as a result, heat treatment processes are among the main sources of energy consumption and environmental footprints. However, they are mandatory steps of the manufacturing process of high strength steels used in many industries. Therefore, the efficiency of a heat treatment furnace in terms of its energy consumption as well as its capability in producing uniform temperature distribution that affects steel's metallurgical transformations are of critical importance (Totten, 2006). In their majority, heat treating industrial furnaces use natural gas as the main source of heating; however, in recent years, due to new environmental requirements, the interest towards the use of electric furnaces has significantly increased (Canale et al., 2008). Despite their promising future, significant challenges still remain to be addressed from a design perspective, e.g., layout, size, and type of electric heating elements, as well as the impact of electricity-based heating, on the final mechanical properties of the product versus a gas-fired based heating approach. This study has been defined in this context and investigates resistance electric furnaces' design parameters, focusing on the balance between energy efficiency and product quality, and emphasizes the application of computational fluid dynamics (CFD) for furnace thermal analysis.

Extensive work has been conducted in recent years on the application of CFD to optimize different aspects of resistance electric furnaces. For instance, Palacio-Caro et al. examined a pit-type electric steel tempering furnace by CFD, testing fan speeds to improve thermal efficiency. Their study, using a moving-reference frame (MRF) method, revealed the critical role of fan speed in optimizing temperature homogeneity and heat transfer in high-temperature furnaces; however, in their study the impact of heating elements on temperature uniformity in the parts was not considered (Palacio-Caro et al., 2020). Similarly, Smolka et al. conducted transient simulations across 30 different cases using ANSYS Fluent to enhance airflow and

thermal dynamics in a laboratory-scale drying oven. Adjusting fan speeds and heater placements, they improved temperature uniformity, achieving a reduction in non-uniformity from 4.2°C to 2.3°C in the modified prototype under specific conditions. Despite these advancements, the study did not establish a quantitative correlation between the simulation parameters and the resulting temperature uniformity, offering potential directions for future research to optimize device design further (Smolka et al., 2010). From another aspect, Filipponi et al. highlighted the substantial energy losses in steel industry furnaces during door-opening events using CFD simulations. Their study showed a significant energy loss of 5606 MJ, during a 10-minute door opening and related it to convective heat flux (Filipponi et al., 2016). Also, Fu et al. investigated temperature distributions in a laboratory-scale resistance furnace for superalloy heat treatment, using ANSYS Fluent. They incorporated a dynamic PID control strategy to regulate the furnace temperature. This approach enhanced the model's ability to predict the equilibrium time required for heating superalloys. Although they developed a robust predictive model, Fu et al. did not analyze temperature discrepancies observed between the center and the surface of the bar (Fu et al., 2019).

Analogously, Angelopoulos et al. developed a CFD model for mineral microsphere expansion in a vertical electric furnace (VEF), examining how furnace wall temperature and air feed rate affected particle states and the final product quality. They reported that increasing the furnace wall temperature under isothermal mode from 900 to 1200°C reduced microsphere density by 28.7%-43.2% across different feed rates, emphasizing the critical impact of precise temperature control on the quality of the product. However, their study stops short of addressing the scalability of these findings to industrial operations (Angelopoulos et al., 2024). In a recent publication, the present authors used CFD, to examine the impact of stacking patterns on temperature uniformity of large-size steel blocks and reported that optimal spacer and skid sizes could reduce temperature non-uniformities by at least 24%. The CFD predictions were validated experimentally; thereby, demonstrating, CFD's efficacy in predicting transient temperatures and optimizing industrial settings (Mirzaei et al., 2023). Furnace design optimization studies using 3D CFD by Tan et al. resulted in reducing heat losses by at least 22% in a vertical wafer annealing furnace (Tan et al., 2022). In another study, Díaz-Ovalle et

al. employed CFD by ANSYS CFX to assess the influence of baffle plate geometries on heating efficiency in a convective electric oven, connecting baffle design with enhanced energy utilization and uniform baking conditions. However, their analysis did not quantify the temperature uniformity and preheating time improvements, and simulations were conducted without considering the effects of load, which could alter oven performance in real-world conditions (Díaz-Ovalle et al., 2017).

The present work focuses on the optimization of heating elements layout and the use of evolutionary algorithms to improve resistance electric furnace efficiency. To this end, a 3D computational fluid dynamics model featuring complex features such as axial fans and heating elements was utilized to simulate the tempering process of high strength steel blocks. The simulation results were then validated experimentally at the industrial scale to test the reliability of the predictions. In a third step, Genetic and Pareto search algorithms were utilized to refine the layout, securing enhanced temperature uniformity within the furnace and through the thickness of the heat-treated steel blocks.

4.2 Furnace and Experimental Measurements Description

The current study was conducted on an industrial electrical heat treatment furnace situated at Finkl Steel in Sorel, Quebec, Canada (Finkl Steel Inc., 2021). This batch-type car bottom furnace boasts a total power capacity of 1710 kW and features two sets of heating elements placed on the opposing side walls of the heating chamber, which collectively encompass 70% of each side wall's surface area. The furnace design incorporates three axial fans positioned atop the chamber, facilitating the circulation of heated air within and around the treated blocks. These fans maintain a consistent rotational speed of 1750 rpm. Notably, the airflow in these high-temperature fans follows a path through the blades, running parallel to the mounting shaft. Figure 4.1 provides a visual representation of the electric furnace, accompanied by detailed diagrams illustrating the heating chamber's dimensions and key features. The internal dimensions of the furnace's heating chamber span 3.43 m, 4.11 m, and 8.02 m. The loading pattern consists of two large rectangular parallelepiped-shaped forging blocks stacked on top

of each other. The upper block (UB) has dimensions of 4.25×1.34×0.66 m^3, while the lower block (LB) measures 4.6×1.27×0.63 m^3, each weighing about 29 metric tons. Five steel skids are used to support the placement of these forged blocks on the car bottom of the furnace. This configuration provides insight into the heat treatment of high thickness forging blocks, which is particularly challenging (N. B. Arkhazloo et al., 2019).

Circulation of the fluid flow by the fans facilitates product heating, and the furnace is designed without an exhaust system. To maintain insulation, the furnace walls are enveloped by insulating blankets made from spun Fiberfrax ceramic fibers (Unifrax, 2017), featuring a thickness of 0.254 m and a thermal conductivity of 0.16 W/mK at the tempering temperature of 537°C. In conjunction with the 6 thermocouples integrated into the furnace controller system, 5 pre-calibrated K-type thermocouples with stainless steel sheathing were positioned on various points of the steel blocks' surfaces, as illustrated in Figure 4.2. Thus, 'L' and 'l' denote the lengths of the lower and upper blocks, respectively; 'H' and 'h' represent their heights; and 'W' and 'w' indicate the widths of the blocks. According to the ISA Standard (Automation, 1982), the K-type thermocouples enveloped in a stainless steel sheath have an accuracy level of ±2.2°C or ±0.75% within furnace operating temperatures. Comprehensive insights into the frameworks designed to achieve robust data collection are presented in recent publications by Arkhazloo et al. (Nima Bohlooli Arkhazloo et al., 2021; N. B. Arkhazloo et al., 2019). Furthermore, Figure 4.3 visually depicts the dynamic evolution of the electrical energy consumption profile of the loaded furnace throughout the heat treatment procedure at a power of 600 V and 60 Hz frequency. It is essential to note that the accuracy of the curve in Figure 4.3 is closely tied to the furnace control system's capability to collect data every 10 seconds, highlighting the impact of the system on monitoring and adjusting energy consumption. The changing slope of the curve over time indicates variations in power consumption rate, with the initial steep slope suggesting high power usage, while the gradually leveling slope towards the end signifies a transition to a more constant and stable power consumption rate. This transition reflects the furnace's operational adjustments as it reaches an isothermal state in the heat treatment process.

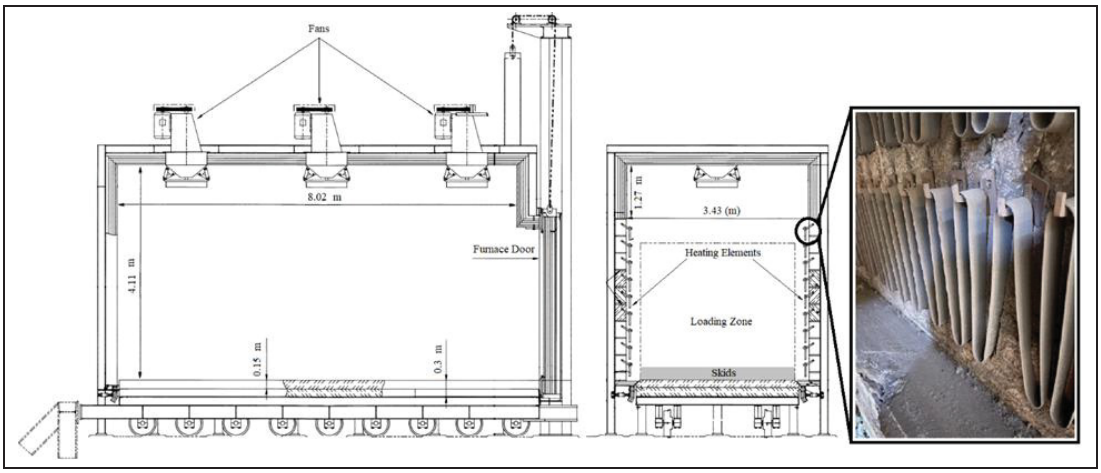

Figure 4.1 Industrial electrical heat treatment furnace structure

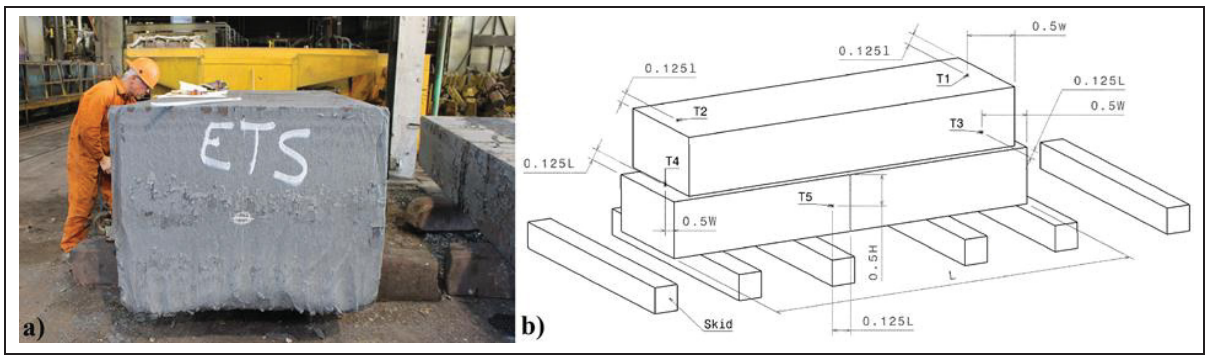

Figure 4.2 a) Instrumented high strength steel block b) a schematic view of the five thermocouples' locations

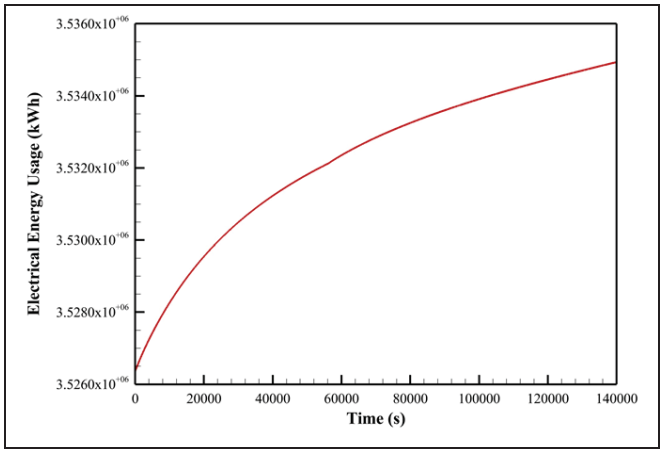

Figure 4.3 Dynamic evolution of the electrical energy consumption profile

4.3 Heating elements Layouts

The analysis of the heating elements layout was conducted in two distinct phases. In Phase 1, methodical exploration of various scenarios was conducted, involving the strategic arrangement of heating elements across different configurations of furnace walls available in the literature (Kanthal, 1999). This phase aimed to identify the impact of heating the stacked high thickness blocks from different directions on thermal uniformity compared to the original condition. The four applicable heating elements layouts subjected to testing were:

1. Two Side Walls Equipped (TSWE), representing the current furnace setup with 70% of the surface area of each side wall covered by heating elements (original condition used for experimental validation, referred to as TSWE-70);
2. All Four Walls Equipped (AFWE), encompassing both sides, the back wall, and the door, with 70% of the surface area of each wall covered by heating elements;
3. All Walls Including the Ceiling Equipped (AWICE), with 70% of each of the four walls plus the whole ceiling covered by heating elements;
4. Only Ceiling Equipped (OCE), with the whole ceiling covered by heating elements and none of the side walls equipped.

Phase 2 was focused on determining the optimum percentage of side wall coverage by the heating elements. This phase aimed to fine-tune the area of the side walls being covered by heating elements to optimize thermal uniformity while maintaining the current setup, which is more favorable for industrial partners due to its practicality and cost-effectiveness. Within this phase, seven distinct cases were simulated, each embodying varying coverage percentages identified as TSWE-10, -20, -30, -50, -70, -90, and -100. In each simulation case, the TSWE values represent the percentage of the furnace side walls covered by heating elements. As the TSWE value increases, it signifies a greater area of the side walls being covered, resulting in more extensive exposure of the furnace's interior to the heating elements. The only independent variable in Phase 2 was the surface area of wall coverage. In Figure 4.4, a schematic representation of the simulated geometries is presented.

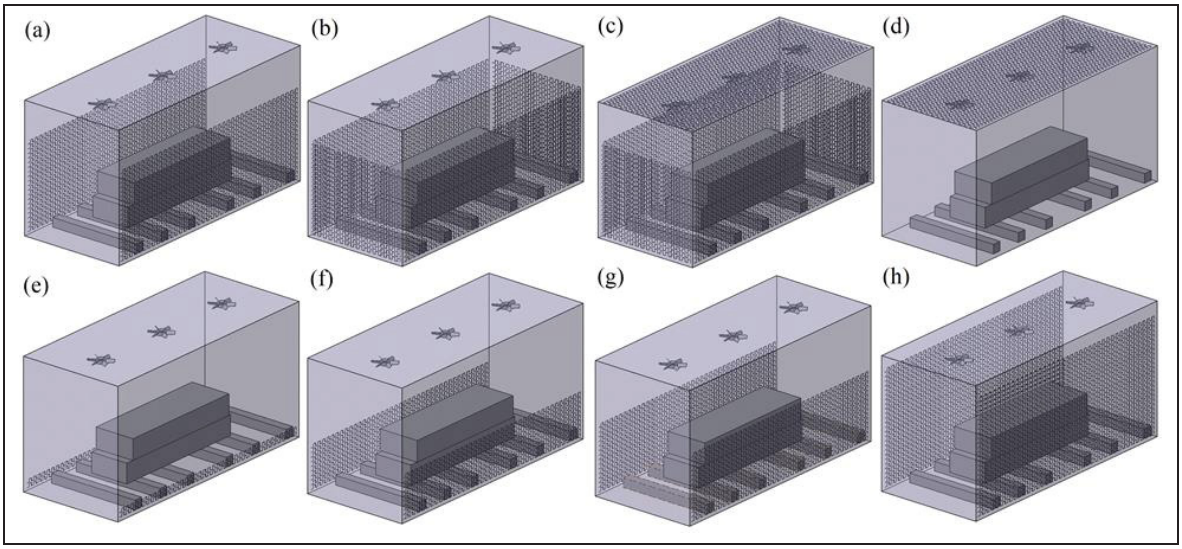

Figure 4.4 Comparative geometries under investigation: a) TSWE-70 (original condition), b) AFWE, c) AWICE, d) OCE, e) TSWE-10, f) TSWE-30, g) TSWE-50, and h) TSWE-90

4.4 Computational Details

The methodology integrates computational fluid dynamics modeling, polynomial regression, and advanced optimization algorithms. It must be mentioned that an almost similar approach has been previously applied by other researchers to analyze electrical arc furnaces (Coskun, Sarikaya, Buyukkaya, & Kucuk, 2023), yet its application to heat treatment furnaces has not been previously reported. The details related to each method are presented in the following:

4.4.1 CFD Model Development

Based on the developed CAD model including described details in section 2, three sets of poly-hex core computational grids, namely coarse, medium, and fine, were tested to ensure grid independence of the obtained results. The medium computational grid, comprising about 1.47 million cells as shown in Figure 4.5, was found to offer predictions that were closely aligned with the fine computational grids and thus was chosen for subsequent simulations. The developed poly-hex core computational grids using ANSYS Fluent Mosaic Technology (ANSYS Inc., 2020), incorporating three boundary layers, balanced computational cost, and

simulation accuracy. The poly-hex core mesh technology provides the advantage of higher computational efficiency due to its reduced cell count and improved orthogonality (Arocena & Danao, 2023). The minimum orthogonal quality of the computational grids was 0.1, ensuring adequate accuracy for the simulations.

The furnace power consumption profile shown in Figure 4.3, divided by the total surface area of the considered heating elements in each case, was applied as the input energy profile boundary condition. Additionally, an average heat loss value of 594 W/m², calculated based on the approach proposed by Hadala et al. (Hadała et al., 2017) and the furnace specifications detailed in section 2, was used as the boundary condition for the furnace walls.

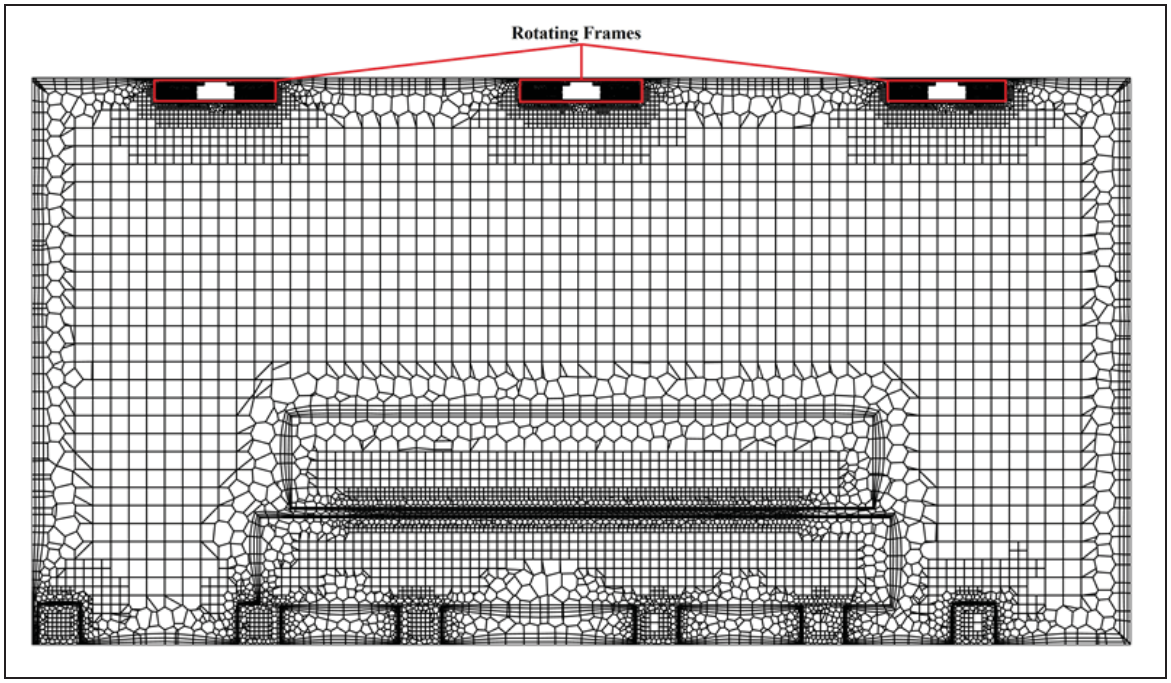

Figure 4.5 Computational grid at the central cross-section (furnace side view)

Simulations were conducted using ANSYS Fluent 2022, which utilizes the finite volume method for computational analysis (ANSYS Inc., 2023). This study specifically focused on heat transfer under turbulent flow conditions induced by fan rotation. The fundamental governing equations employed in the simulation were the continuity equation, the Navier-

Stokes equation for momentum, and the energy equation, as detailed in equations 1-3 (ANSYS Inc., 2023). Consequently, to handle the pressure-velocity coupling in this complex flow scenario, the SIMPLEC algorithm was adopted which offers a more consistent and rapid convergence (Van Doormaal & Raithby, 2007).

Continuity Equation:

$$\frac{\partial \rho}{\partial t} + \nabla . (\rho v) = 0 \tag{4.1}$$

Momentum Equation:

$$\frac{\partial (\rho v)}{\partial t} + \nabla . \rho v v = -\nabla p + \rho g + \nabla . \tau \tag{4.2}$$

Energy Equation:

$$\frac{\partial}{\partial t}(\rho e) + \nabla . (v(\rho e + p)) = \nabla . (k \nabla T) + S \tag{4.3}$$

Here, ρ is the fluid density, p is the pressure, v is the velocity field, g represents the gravitational acceleration, τ is the stress tensor, e is the total energy per unit mass, which includes both kinetic and internal energy, T is the temperature, k is the thermal conductivity and S encompasses radiation and other heat sources.

In the present work, the turbulence associated with the induced flow circulation caused by fans rotation was modeled using the two-equation realizable k-ε turbulence model (Shih, Liou, Shabbir, Yang, & Zhu, 1995) in conjunction with the multiple reference frame (MRF) model (ANSYS Inc., 2023). This was achieved by considering cylindrical-shaped zones around each of the fans inside the furnace where the MRF model was applied. The computational domain was divided into three rotating reference frames corresponding to the three fans and one stationary frame for the rest of the furnace, including the blocks. The MRF approach

transforms the fluid equation of motion to a rotating frame, enabling steady-state solutions for rotating parts of the domain (Mirzaei et al., 2023). The governing equations for the MRF zones include modifications to the Navier-Stokes equations to account for rotational effects.

To accurately capture the near-wall effects, scalable wall functions were employed in conjunction with the realizable k-ε model. This approach improves the accuracy of turbulence modeling close to the walls, where flow characteristics are significantly different from the bulk flow. The scalable wall functions ensure that the near-wall treatment is appropriate across a wide range of Y^+ numbers and flow conditions (Arocena & Danao, 2023). This combination of the realizable k-ε model and the MRF model allows for capturing both the large-scale rotational flows induced by the fans and the finer turbulence structures within the furnace. For the turbulence model, this is achieved by solving the equations for turbulence kinetic energy (k) and dissipation rate (ε), as outlined in Eq. 4 and 5. It uses a different formulation for the turbulent viscosity and the constants $C_{1\varepsilon}$ and $C_{2\varepsilon}$ compared to the standard k-ε model. These modifications make the Realizable model more accurate for a wider range of turbulent flows (Shih et al., 1995). It must be noted that the above approach is in agreement with studies by other researchers (Dogruoz & Shankaran, 2017; Smolka et al., 2010) who reported that k-ε and MRF could be reliably used to study turbulent flow under conditions closely resembling the present work.

$$\frac{\partial(\rho k)}{\partial t} + \nabla.(\rho k v) = \nabla.[(\mu + \sigma_k \mu_t)\nabla \mathrm{k}] + P_k - \rho\varepsilon \tag{4.4}$$

$$\frac{\partial(\rho\varepsilon)}{\partial t} + \nabla.(\rho\varepsilon v) = \nabla.[(\mu + \sigma_\varepsilon \mu_t)\nabla\varepsilon] + C_{1\varepsilon}\frac{\varepsilon}{k}P_k - C_{2\varepsilon}\rho\frac{\varepsilon^2}{k}\frac{\partial}{\partial t}(\rho e) + \nabla.(v(\rho e + p)) = \nabla.(k\nabla T) + S \tag{4.5}$$

Here, k is the turbulent kinetic energy per unit mass, μ is the molecular viscosity, μ_t is the turbulent viscosity.σ_k is the turbulent Prandtl number, P_k is the production of turbulent kinetic energy, ε is the turbulent dissipation rate, σ_ε is the turbulent Prandtl number for ε, $C_{1\varepsilon}$ and $C_{2\varepsilon}$ are model constants.

Among the radiation models reported (Versteeg & Malalasekera, 2007) by Versteeg for calculating radiative heat transfer in a 3-dimensional furnace geometry, the S_{16} discrete ordinates (DO) method has an acceptable accuracy level, comparable to the Monte Carlo (MC) method. However, the MC method demands substantially more computational resources, over 20 times greater than the DO method. In the S_n DO model, the 'n' denotes the number of discrete angular directions used in the numerical approximation of the radiative transfer equation. Jamaluddin and Smith (Jamaluddin & Smith, 1988) tested different approximation orders (S_2, S_4, S_6, and S_8) for the DO model in a 3D rectangular enclosure, aiming to evaluate their effectiveness against exact analytical and numerical solutions. The S_4 approximation was deemed adequate, considering its balance between accuracy and computational time. Although the surface-to-surface (S2S) model was previously used for the same geometry by Mirzaei et al. and they reached an acceptable average error of 6.6% (Mirzaei et al., 2023). However, for considering the radiation effects in the present work, the S4 DO model following Jamaluddin and Smith tests (Jamaluddin & Smith, 1988) was adopted in this study. This model provides a numerical solution to the radiative transfer equation (RTE) over a limited set of discrete solid angles, which can be mathematically expressed as (ANSYS Inc., 2023):

$$\nabla.(I(\vec{r},\vec{s})\vec{s}) + aI(\vec{r},\vec{s}) = a\frac{\sigma T^4}{\pi} \tag{4.6}$$

Where I denotes the radiative intensity at the position $\vec{r}$ in direction $\vec{s}$, a is the absorption coefficient, and σ stands for the Stefan-Boltzmann constant.

The ideal gas model was employed to account for variations in air density due to temperature changes while keeping pressure constant. This model is appropriate for the current study as it simplifies the calculations and is sufficiently accurate for the temperature range considered in the simulations (Nakhaei et al., 2020). The ideal gas assumption facilitates efficient computation without significant loss of accuracy, given the relatively constant pressure conditions within the furnace. Notably, in addressing the challenges of heat treatment processes, this study specifically considered the impact of temperature variations on the thermo-physical properties of large blocks made of high-strength medium carbon steel.

Utilizing JMatPro software (SenteSoftware), an application proficient in calculating properties for complex alloys, these varying properties were estimated and subsequently incorporated into the CFD model, as illustrated in Figure 4.6. The accurate chemical composition of the material, measured by the authors' team and presented in Table 4.1, served as the input for the JMatPro software. The robustness of JMatPro in accurately determining the properties for such specific alloy compositions has been corroborated in the existing literature (Mayr et al., 2017) and aligns with the findings from previous investigations by the authors (Mirzaei et al., 2023).

In this simulation, particular attention was given to the temperature-dependent thermal conductivity and specific heat, critical parameters for precisely modeling the heat conduction within the steel blocks and ensuring the system's energy equilibrium. In Figure 4.6, the green curve represents thermal conductivity, which shows a slight initial increase, peaks at approximately 140°C with a value of 41.5 W/m.K, and then progressively decreases as the temperature rises, stabilizing at about 35.2 W/m.K during the isothermal phase of the tempering process. Conversely, the specific heat exhibits a consistent upward trend from ambient temperature to the final target tempering temperature of 537°C, increasing from 450 J/kg.K to approximately 752 J/kg.K. It is important to highlight that in simulations involving fluid-solid interactions, as well as metallurgical and thermal domains that necessitate physically coupled models, the precision of the numerical simulation is critically dependent on pre-calculated, temperature-dependent variables (Lavadera et al., 2024; Qiu, Li, Feng, Chen, & Zhang, 2019). These are closely associated with the phases present in the steel and their transformation throughout the process (G. H. Wang & Li, 2019).

Table 4.1 Chemical composition of the investigated steel (wt%)

C	Mn	Si	Ni	Cr	Mo	Cu	Other
0.35	0.99	0.41	0.5	1.86	0.53	0.16	Micro Alloying

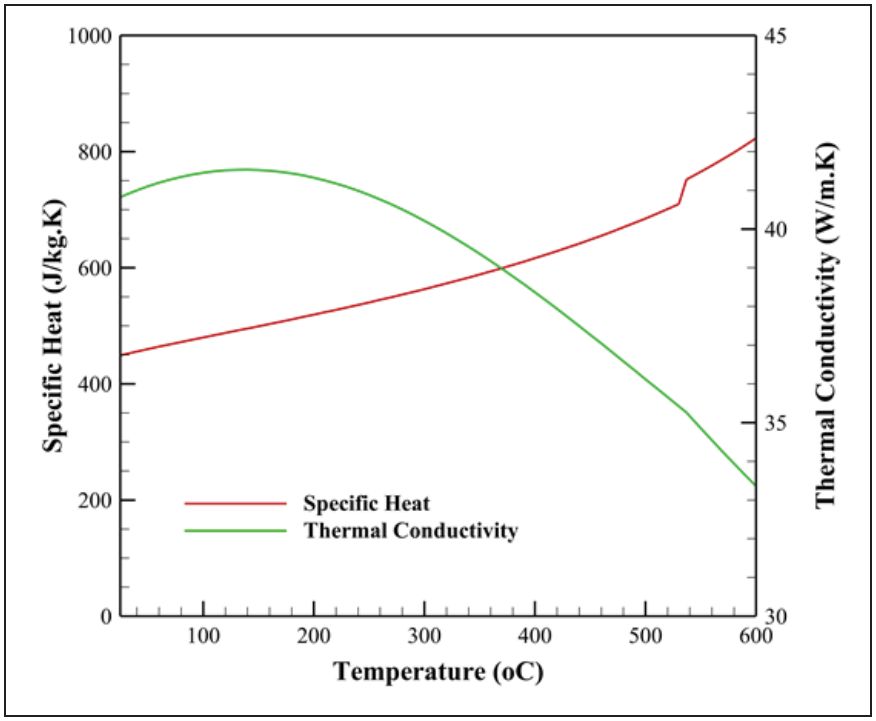

Figure 4.6 Temperature-dependent thermo-physical properties of large block

For the convergence criteria, values of 10^{-5} were set for the continuity, momentum, and turbulence equations, while a finer 10^{-6} threshold was applied to the energy and radiation equations, ensuring accurate and stable simulation outcomes.

4.4.2 Polynomial Regression Fitting

Once the CFD simulations provided results for different scenarios, the relationship between the TSWE values and the furnace performance parameters (surface temperature non-uniformity, surface-to-center temperature differential, centers temperature differential) was quantified using polynomial regression of degree 3. The general form of a polynomial regression is (MathWorks, 2021):

$$y_x = \beta_0 + \beta_1 x + \beta_2 x^2 + \cdots + \beta_n x^n + e \quad (4.7)$$

Where y_x is the dependent variable (e.g., surface temperature non-uniformity), x is the independent variable (e.g., wall coverage percentage), n is the polynomial degree, β's are the coefficients that characterize the magnitude and direction of the influence of each term, and e is the error term.

To ensure the regression models are comparable despite differing scales of the parameters, the extracted values from the CFD simulations were normalized. The normalization process adjusts the scale of each parameter, facilitating direct comparison for optimization purposes. The normalized values were calculated using the equation:

$$\text{Normalized Value} = \frac{y_x - y_{min}}{y_{max} - y_{min}} \tag{4.8}$$

MATLAB 2021 tools were employed to fit these polynomial functions to the normalized data points obtained from CFD simulations, enabling predictive insights into furnace behavior under different conditions.

4.4.3 Multi-Objective Optimization

To determine the optimal layout based on the derived polynomial relationships, two evolutionary optimization algorithms were employed:

Genetic Algorithm (GA) is well known for obtaining optimal solutions by emulating the process of natural evolution (S.N. Sivanandam, 2007). The algorithm starts with an initial population of potential solutions, evaluates their fitness, and iteratively refines the population through processes analogous to selection, crossover (recombination), and mutation. The 'crossover heuristic' function was employed as the crossover function. This particular method was chosen because it is specifically tailored for multi-objective optimization (Umbarkar & Sheth, 2015). This method enhances variation among the solutions, broadening the search across the solution space and increasing the likelihood of identifying optimal solutions for each

objective in multi-objective optimization scenarios (Umbarkar & Sheth, 2015). The approach to minimizing the objective functions is inspired by methodologies outlined in 'Multi-objective Evolutionary Optimisation for Product Design and Manufacturing' (Deb, 2011). Table 4.2 provides an overview of the hyperparameters used in the implemented genetic algorithm. Pareto search (PS) algorithm was also used; it is characterized by its unique ability to effectively identify and differentiate Pareto optimal solutions in multi-objective optimization contexts (MathWorks, 2021), which is complementary to the GA method and therefore will allow a more accurate analysis of the results. In this methodology, the 'GPSPositiveBasis2N' polling strategy for the PS algorithm was selected specifically. This choice was made due to its systematic utilization of 2N positive basis vectors in each iteration of the PS algorithm. The 'GPSPositiveBasis2N' method is adept at navigating one-dimensional search spaces (MathWorks, 2021), which aligns well with the requirements of the current problem. By employing this strategy, it was aimed to enhance the capability of the PS algorithm in identifying potentially superior solutions, thereby optimizing the effectiveness of the algorithm in this specific context. Given a set of objective functions $F=[f_1(x), f_2(x),\ldots, f_i(x)]$, a solution x^* is Pareto optimal if there is no x such that (Fleischer, 2003):

$$f_i(x) \leq f_i(x^*) \ \forall i \tag{4.9}$$

And

$$f_i(x) \leq f_i(x^*) \tag{4.10}$$

For at least one j. Table 4.3 outlines the hyperparameters for the applied Pareto search algorithm.

Table 4.2 GA hyperparameters

Max Generations	1000
Population Size	500
Crossover Fraction	0.6
Crossover function	Crossover heuristic
Pareto Fraction	0.4
Function Tolerance	1e-6

Table 4.3 PS algorithm hyperparameters

Max Function Evaluations	24000
Pareto Set Size	200
Min Poll Fraction	0.5
Poll Method	GPSPositiveBasis2N
Pareto Set Change Tolerance	1e-6
Max Iterations	1000

By cohesive blending these tools and techniques, the study pinpointed the layouts that significantly elevated the furnace's performance, achieving enhanced uniformity in temperature distribution and other desired quality parameters.

4.5 Results and Discussion

4.5.1 Validation

Figure 4.7 provides a comparative representation, expressed in percentage, of the transient temperatures observed on the surfaces of the forging blocks for different thermocouple (TC) locations and the corresponding predictions obtained from the CFD model. The error percentage shown in this figure reflects the accuracy of the TSWE-70 model, which represents the original condition of the furnace where the experimental test was conducted. In this original condition, 70% of the furnace side walls were covered by heating elements, hence the designation TSWE-70.

Over the entire 41.6-hour duration of the heat treatment process, the CFD predictions present consistency when compared with the actual measurements showcasing a maximum average deviation of approximately 2% (attributed to TC5) further confirming the robustness of the developed CFD model within the scope of this investigation. The outlier circles for TC1 and TC2 indicate instances where the model's predictions varied from the empirical data by a margin that is larger (and notably smaller for TC2) than the typical variation observed. These outliers, while exceeding the main error range, maintain an error below 6 percent, thereby supporting the overall accuracy of the simulation.

This validation paved the way for the model's utilization in assessing the influence of heating elements' layout on the thermal history of the large-size blocks under scrutiny. Subsequently, nine other models were developed and assessed to evaluate different heating element configurations: AFWE, AWICE, OCE, TSWE-10, TSWE-20, TSWE-30, TSWE-50, TSWE-90, and TSWE-100.

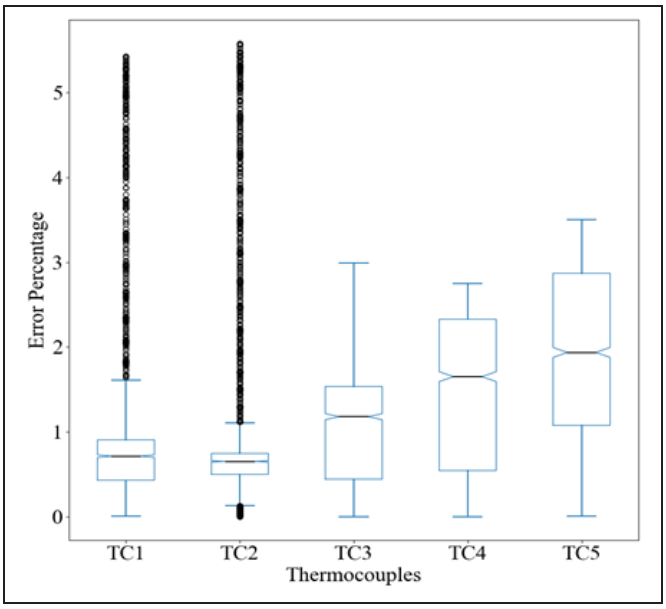

Figure 4.7 Validation of the CFD model

4.5.2 Phase-1 Analysis

Figure 4.8 illustrates the volume average temperature profiles, or in other words, the heating curves experienced by both large blocks over the tempering process in layout TSWE-70 (original condition). The blue dashed line represents the temperature of the upper block (UB), while the black dashed line denotes the lower block (LB). Initially, the blocks exhibit different volume average temperatures due to their distinct initial conditions, with the lower block starting at a slightly higher temperature than the upper block.

Throughout the non-isothermal cycle, both blocks progressively absorb heat. The upper block (UB) shows a steeper initial rise in temperature, indicating a more rapid heat absorption compared to the lower block (LB). However, as time progresses, the rate of temperature increases for both blocks start to converge. Around the 100,000-second mark, both blocks reach approximately 530°C, and their temperature profiles begin to level off as they approach the target temperature for the isothermal cycle. During the subsequent isothermal cycle, both blocks maintain the target temperature, demonstrating more uniform thermal conditions for the remainder of the process. This phase is crucial for achieving the desired mechanical properties in the tempered steel, as it ensures that the blocks are held at a consistent temperature.

This analysis underscores the intense thermal behaviors in the initial phase (non-isothermal cycle), which lead to some temperature non-uniformities. The distinct heating rates in the early stages can be attributed to the varying direct exposure each block receives from the respective heating elements. These dynamics are further discussed in Figure 4.9, which delves into the temperature distributions and uniformity across different heating element configurations.

Notably, the volume average temperature profiles indicate that the current TSWE-70 setup effectively brings both blocks to the desired temperature, but the differences highlight potential areas for optimization in the heating process to minimize temperature gradients and improve overall uniformity.

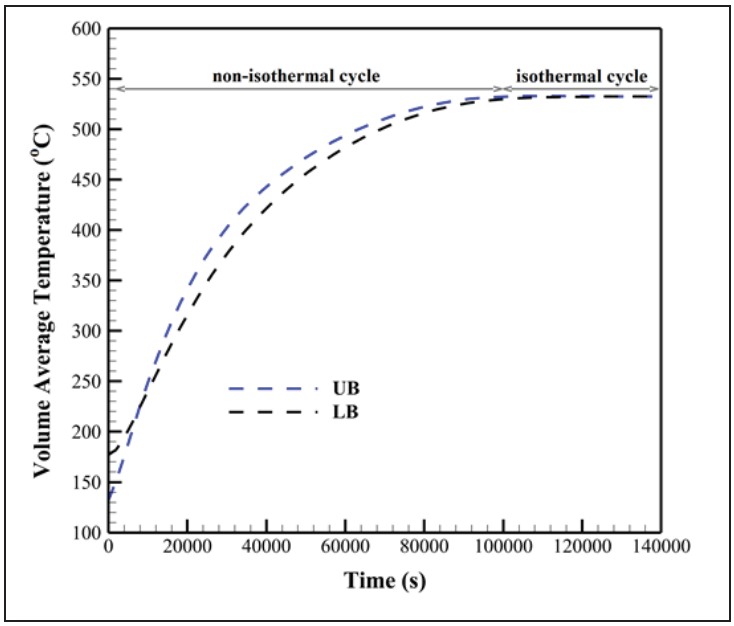

Figure 4.8 Volume average temperature profiles of upper (UB) and lower (LB) blocks in layout TSWE-70

In Figure 4.9(a), the transient changes in maximum surface temperature non-uniformities of large blocks during heat treatment across four layouts from phase 1 are depicted. The surface temperature non-uniformity is defined as the instantaneous temperature difference between two points on a block's surface, with one having the highest and the other the lowest temperature. Notably, significant non-uniformities were observed during heat treatment, aligning with findings for gas-fired furnaces (W. C. Ji, Li, Wei, & Yi, 2021; D. J. Wang, Zhang, Zhu, & Jiang, 2024). Metallurgical heat treatment studies usually overlook this non-uniformity, focusing more on the temperature gradient from the block's surface to its center. In layout AWICE, where all four walls and the ceiling were equipped with heating elements, the non-uniformities surged to a notable 212°C around the upper block, increasing at rates up to 76.5°C/h. Other layouts, particularly TSWE-70, recorded lower non-uniformities at 200°C. By the end of the process, non-uniformities decreased, aligning with the isothermal tempering temperature of 537 °C. However, prolonged exposure to these non-uniformities could impact the mechanical properties across the product, as a large value for surface non-uniformities indicates different thermal histories experienced by one end of the block compared to the other.

This variation is directly correlated with the final mechanical properties of the product, as discussed in the literature (Gao et al., 2000; Kang & Rong, 2006).

The initial peak in surface temperature non-uniformity is most pronounced in the AWICE and AFWE configuration, reaching the maximum early in the process. This indicates that equipping all walls and the ceiling with heating elements leads to more rapid but uneven heating. The curves for OCE and TWSE-70 configurations also show significant initial non-uniformities, but these reduce more quickly compared to AWICE and AFWE. The TSWE-70 configuration, on the other hand, shows a relatively lower initial non-uniformity, suggesting a more controlled and uniform heating process.

The total surface temperature non-uniformity (surface area under each curve) for both blocks is notably less in TSWE-70. This indicates the advantage of the TSWE-70 configuration in maintaining more consistent surface temperatures throughout the heat treatment process. Additionally, the rate at which the non-uniformity decreases provides insights into the thermal stability of each configuration. For instance, the faster reduction of non-uniformities in the TSWE-70 layout implies a quicker stabilization of temperature differences, which is beneficial for achieving uniform thermal conditions. Figure 4.9(b) illustrates the transient changes in the surface-to-center temperature differential of each block during phase 1. The surface-to-center temperature differential of each block is calculated as the immediate temperature difference between the block's hottest surface point and its center point.

TSWE-70 outperforms, with the smallest differential at 188°C and 170°C for both upper and lower blocks, respectively. In contrast, the highest differentials for the lower and upper blocks are observed in layouts OCE and AFWE, respectively. This indicates that these layouts lead to rapid but uneven internal heating, causing significant temperature gradients within the blocks. The curves for TSWE-70 show a more controlled rise, having a notably smoother and lower peak, suggesting better internal thermal uniformity. The difference can be attributed to the direct exposure each block receives from the respective heating elements. Comparing this with Figure 4.9(a), it is evident that the TSWE-70 configuration not only minimizes surface

temperature non-uniformity but also reduces internal temperature gradients, which is crucial for achieving uniform mechanical properties. The AFWE and AWICE layouts, while showing high surface temperature non-uniformity in Figure 4.9(a) for the upper block, also exhibit significant surface-to-center temperature differentials in Figure 4.9(b), indicating their inefficiency in achieving uniform heating.

The rate at which the surface-to-center temperature differential decreases provides insights into the thermal stability of each configuration. The fast reduction of temperature differentials in the TSWE-70 layout implies a quicker stabilization of internal temperature differences, beneficial for achieving uniform thermal conditions throughout the block. This aligns with observations from Figure 4.9(a), where TSWE-70 also showed a faster reduction in surface temperature non-uniformity. Notably, the OCE configuration shows a faster reduction in surface-to-center non-uniformity for the upper block, indicating an advantage in achieving thermal stability in this specific direction of heating. However, for the lower block, the OCE configuration results in a slower reduction of non-uniformity, highlighting the variability in performance based on block position and heating direction.Figure 4.9(c) illustrates the evolving temperature disparities at the centers of the two blocks during the heat treatment process across four different layouts. The center temperature differential is obtained by subtracting the temperature of the center of the upper block from the lower one. Initially, the center of the upper block was approximately 45°C cooler compared to the lower block. However, as the heat treatment advanced, this temperature gap was not only mitigated but also reversed, particularly noticeable in the OCE layout. In this layout, the temperature at the center of the upper block exceeded that of the lower block by about 56°C after 8 hours. In contrast, the other layouts, namely AWICE, AFWE, and TSWE-70, displayed smaller differences in the center temperatures of the blocks over time.

Comparing this with Figure 4.9(b), it is evident that the OCE layout not only exhibits high surface-to-center temperature differentials but also large discrepancies between the centers of the blocks, particularly for the lower block. This reinforces the observation that the OCE layout is less effective in providing uniform heating, both on the surface and internally. The

significant temperature differential in the OCE layout can be attributed to the direct exposure of the upper block to heating from the top, which causes uneven heating between the upper and lower blocks.

The AWICE and AFWE layouts, while showing intermediate performance, still exhibit higher temperature discrepancies than TSWE-70 but lower than OCE. The AWICE and AFWE layouts, while showing intermediate performance, still exhibit higher temperature discrepancies than TSWE-70 but lower than OCE. AWICE shows considerable center temperature differentials compared to TSWE-70 and AFWE because it also includes the ceiling equipped with heating elements like OCE, so the upper block receives more heat from the top direction. However, its maximum is lower than OCE because in AWICE, in addition to the ceiling, all four side walls are equipped with heating elements, so at any moment, the ceiling elements have a lower portion of heat to emit.

On the other hand, the TSWE-70 layout shows the smallest and most stable temperature discrepancies between the block centers, indicating a more uniform heat distribution throughout the blocks. This is consistent with the findings from Figure 4.9(a) and Figure 4.9(b), where TSWE-70 also demonstrated better performance in minimizing temperature non-uniformities and differentials.

Overall, these observations highlight the impact of different furnace designs on the thermal history of each block, despite being part of the same batch and subject to the same heat treatment schedule. The TSWE-70 configuration consistently demonstrates superior performance in maintaining uniform temperatures, both on the surface and internally, leading to more consistent mechanical properties in the treated blocks.

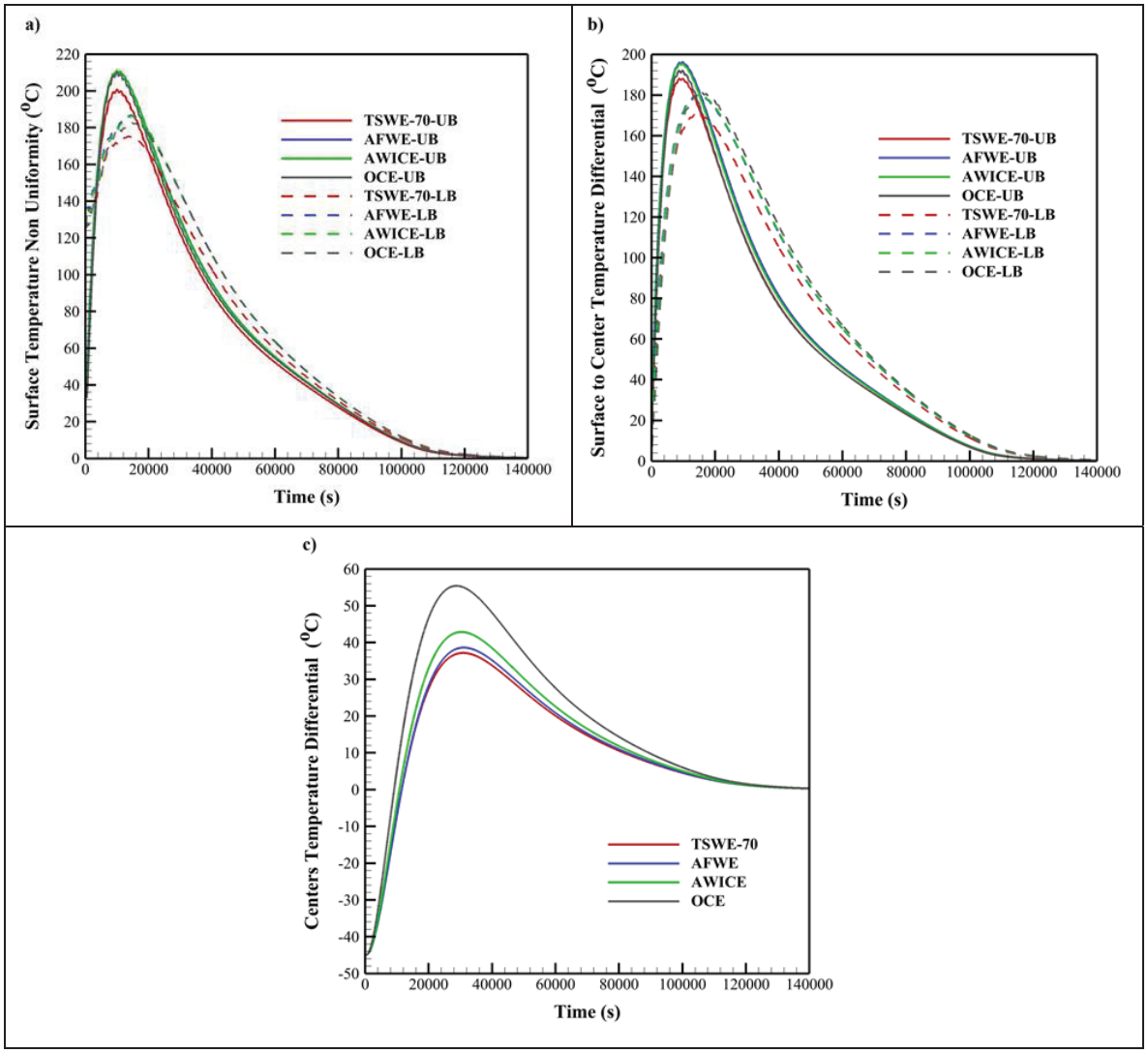

Figure 4.9 Comparative thermal dynamics of upper (UB) and lower blocks (LB) during heat treatment: analysis of a) surface temperature non-uniformity, b) surface-to-center temperature differentials, c) centers temperature differential under heating elements layouts

Table 4.4 compares the maximum values experienced for each of the vital parameters in each of the layouts relative to layout TSWE-70. It can be seen that alternative layouts, compared to the optimal layout, result in an increase in maximum surface non-uniformities ranging from 4.2% to 6.6%. Furthermore, the surface-to-center temperature difference within the blocks increases from 2.2% to 6.3%. Such surface temperature non-uniformity along with surface-to-center temperature non-uniformities within each block in a batch result in different zones undergoing varied thermal histories. This variation implies that each zone is exposed to varying

temperatures for different durations during the non-isothermal cycle. Such differential thermal exposure can result in inconsistencies in mechanical properties across the blocks (Gao et al., 2000; Kang & Rong, 2006), which can ultimately be attributed to the furnace's design.

However, the significant point of interest in this table pertains to the temperature difference at the center of the blocks. As observed, the use of AFWE, AWICE, and OCE configurations results in progressively higher temperature differences at the center of the blocks. For example, in layout OCE, which is a common pattern for heating elements placement in electric furnaces (Kanthal, 1999), this temperature difference has increased by up to 49% compared to the TSWE-70 configuration. This substantial increase highlights the inefficiency of the OCE layout in providing uniform heating, likely due to the predominant top heating leading to significant thermal gradients.

Table 4.4 Percentage deviations of performance parameters for each layout compared to TSWE-70

Layouts	Maximum surface temperature non-uniformity-UB	Maximum surface temperature non-uniformity-LB	Maximum surface-to-center temperature differential-UB	Maximum surface-to-center temperature differential-LB	Maximum centers temperature differential
AFWE	+4.8	+6.6	+4.4	+5.4	+3.9
AWICE	+5.2	+6.3	+3.9	+5.5	+15.4
OCE	+4.6	+4.2	+2.2	+6.3	+49.1

Despite the discussed superior performance in TSWE-70, it's crucial to note that this configuration also exhibits considerable surface temperature non-uniformity and a noteworthy difference from the surface to the center. More importantly, there's a significant temperature discrepancy between the centers of the blocks, even though identical final properties are expected for both of them. A further confirmation of the above analysis is illustrated in Figure 4.10 where a cross-sectional temperature contour of the loaded blocks in the furnace with TSWE-70 configuration at the final moment of the non-isothermal cycle (after 27.8 hours from the start of the process) is depicted. It can be seen that the majority of the volume of the upper

block, particularly its center as indicated by the dashed lines, is about the target temperature. In contrast, the center point of the lower block and a large surrounding area is approximately 10°C cooler. This indicates unequal energy absorption by these two blocks, underscoring the need for improvement in furnace design to achieve optimal performance.

To address these discrepancies, the next phase of the study involved fine-tuning the coverage area of the side walls by heating elements within the TSWE configuration. This adjustment aimed to optimize thermal uniformity while retaining the existing setup, which is preferred by industrial partner for its practicality and cost-effectiveness. Specifically, this fine-tuning process involves adding or removing rows of heating elements along the furnace's side walls, making it a practical and cost-effective solution for improving thermal uniformity without necessitating a complete overhaul of the existing furnace design.

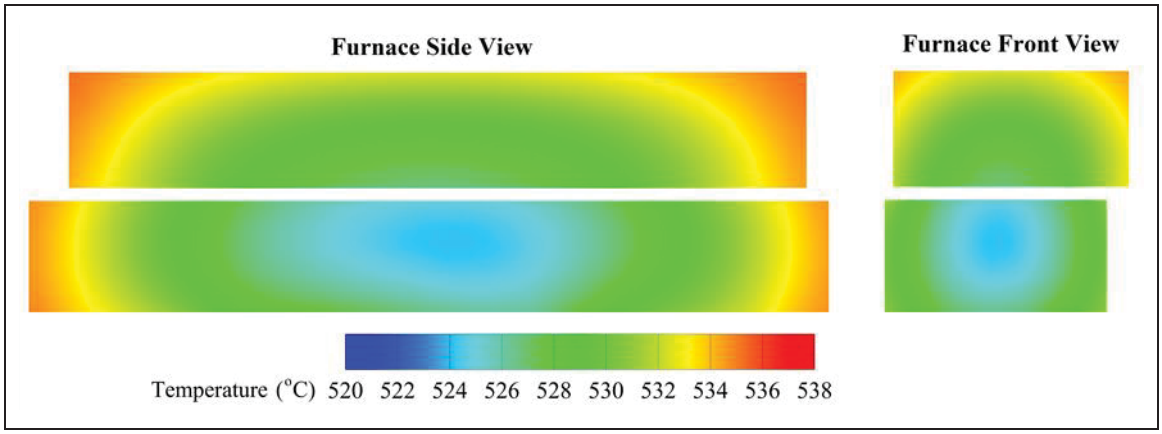

Figure 4.10 Temperature contour of loaded blocks at the central cross-section at t=100,000 s (End of non-iso thermal cycle) for TSWE-70

4.5.3 Phase-2 Analysis

As outlined in Section 3, the second phase of this study focused on determining the optimum percentage of side wall coverage by the heating elements, examining seven distinct cases. These cases involved varying the coverage percentages on the two side walls to 10%, 20%, 30%, 50%, 70%, 90%, and 100%. This phase aimed to analyze the dependency of key

performance parameters on the extent of wall coverage by the heating elements. Ultimately, this will aid in determining the optimal coverage for achieving uniform thermal conditions.

As illustrated in Figure 4.11, the following parameters are presented in a normalized form as a function of wall coverage percentage by heating elements: maximum surface temperature non-uniformity of the upper and lower blocks, maximum surface-to-center temperature differential of the upper and lower blocks, required time for the upper and lower block centers to reach the target temperature, and centers temperature differential. The purpose of normalizing these values is to prevent any single objective from overpowering the others due to scale differences, accelerate convergence in iterative optimization methods, and facilitate a clearer interpretation of variable importance (He et al., 2021).

Table 4.5 indicates the accuracy of the extracted polynomial functions for each of the performance parameters, relative to the extent of wall coverage with heating elements. The data reveals a strong fit for the polynomial models, as evidenced by the high R-squared values and low mean square errors (MSE) across all parameters. The R-squared value, or R-sq%, is particularly important as it represents the percentage of variation in the response that is explained by the model (Chicco, Warrens, & Jurman, 2021; Rabiee, Ahmadian-Elmi, Hajmohammadi, & Mohammadifar, 2023). Notably, the minimum R-squared value observed is 97.88% for the surface temperature non-uniformity of the lower block, which still indicates a highly significant model fit. Conversely, the mean square error (MSE) is a measure of the variation that the model does not capture, with the highest MSE being 0.0077 for the same parameter. This suggests that while the model is highly predictive, there are a small degree of variations that it does not account for (Ostertagová, 2012). In general, the present acceptable degrees of fit suggest that the polynomial functions are highly effective in predicting the thermal behavior of the blocks under various conditions of wall coverage by heating elements.

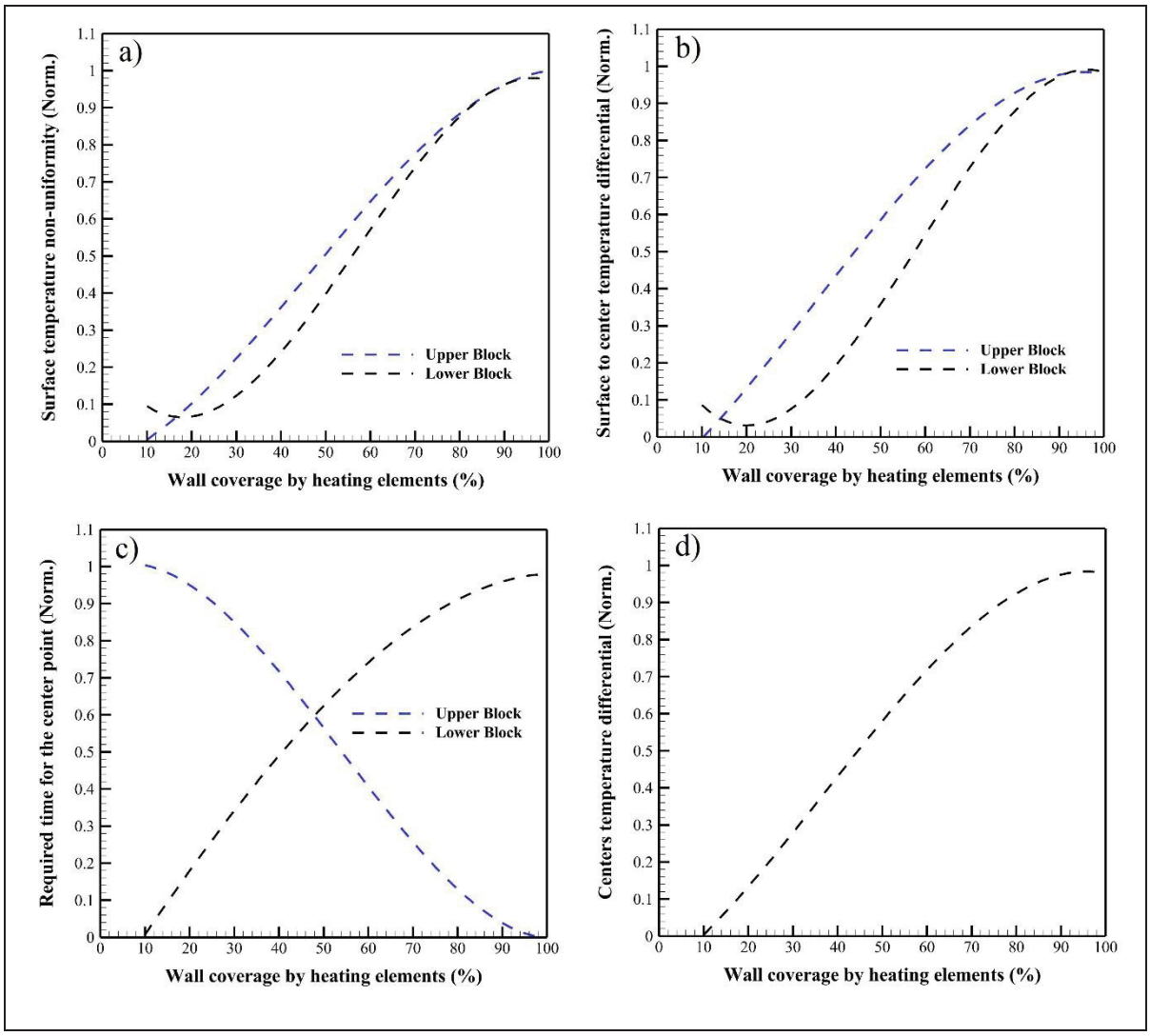

Figure 4.11 Polynomial regression curves of blocks thermal parameters vs. wall coverage by heating elements: a) surface temperature non-uniformity of the blocks b) surface-to-center temperature differential c) required time for the blocks' center to touch the target temperature d) centers temperature differential

Table 4.5 Accuracy of the extracted polynomial functions for performance parameters

Formulated objective functions as a dependency on wall coverage by heating elements	R-sq %	MSE
Surface temperature non-uniformity of the upper block	99.60	0.0014
Surface temperature non-uniformity of the lower block	97.88	0.0077
Surface-to-center temperature differential of the upper block	99.85	0.0005
Surface-to-center temperature differential of the lower block	98.63	0.005
Centers temperature differential	99.53	0.0015
Required time for the upper block center to touch the target temperature	99.57	0.0017
Required time for the lower block center to touch the target temperature	99.46	0.0016

Figure 4.11(a-d) present the thermal behaviors of the upper and lower blocks in relation to the heating element's wall coverage. In Figure 4.11(a), the normalized surface temperature non-uniformity as a function of the wall coverage percentage by heating elements is depicted for both upper and lower blocks. The surface temperature non-uniformity of the upper block (blue curve) starts at 0 at 10% coverage, indicating an optimal situation for the upper block in terms of surface non-uniformity. This value steadily increases, reaching a normalized value of 1 at 100% coverage. Conversely, the lower block (black curve) begins at 0.1 at 10% coverage, decreases to a minimum near 0.06 at about 20% coverage, and then follows a similar upward trend to the upper block, also reaching 1 at 100% coverage. Overall, both curves follow a similar trend. The lower non-uniformity at lower coverage levels, especially for the lower block, can be attributed to the more effective distribution of heat at these levels, which balances the surface temperatures. At 20% coverage, approximately three-quarters of the lower block's side surfaces and all the skids are directly faced to the heating elements, resulting in a more balanced temperature distribution. As coverage increases, the additional heating elements expose more block surfaces directly, leading to increased non-uniformity due to uneven heat distribution. This underscores the importance of optimizing wall coverage by heating elements to achieve uniform surface temperatures.

In Figure 4.11(b), the normalized surface-to-center temperature differential as a function of the wall coverage percentage by heating elements is shown for both upper and lower blocks. The upper block's differential (blue curve) starts at 0 at 10% coverage and steadily increases, reaching a normalized value of 1 at 100% coverage. On the other hand, the lower block's

differential (black curve) begins at 0.1 at 10% coverage, decreases to a minimum near 0.03 at about 20% coverage, and then rises similarly to the upper block, also reaching a normalized value of 1 at 100% coverage. When comparing this to Figure 4.11(a), which depicts the normalized surface temperature non-uniformity, it is observed that both parameters exhibit similar trends in response to changes in wall coverage by heating elements. This similarity suggests a consistent underlying thermal behavior influenced by the distribution of heating elements. As wall coverage increases, both surface temperature non-uniformity and surface-to-center temperature differential tend to increase, indicating that more extensive heating element coverage leads to greater thermal gradients within the blocks.

In Figure 4.11(c), the normalized required time for the center points of the upper and lower blocks to reach the designated temperature is depicted as a function of the wall coverage percentage by heating elements. The upper block's required time (blue curve) starts at a normalized value of 1 at 10% coverage, indicating that this coverage requires the most time for the upper block to reach the target temperature. As the coverage increases, the required time decreases, reaching a normalized value of 0 at 100% coverage, indicating the least time required. Conversely, the lower block's required time (black curve) starts at a normalized value of 0 at 10% coverage, showing that this coverage requires the least time for the lower block to reach the target temperature, and increases to a normalized value of 1 at 100% coverage, indicating the most time required. This inverse relationship between the two blocks can be attributed to the distribution of heat within the furnace. At lower coverage levels, the heating elements primarily affect the lower block, which is closer to the heat source, resulting in quicker heating. As the coverage increases, the heat is distributed more evenly across the furnace, and the upper block benefits from increased exposure, leading to a decrease in the required time to reach the designated temperature. Therefore, achieving optimal thermal uniformity required fine-tuning the coverage percentage, which is discussed in detail in the next section (5.4).

In Figure 4.11(d), the normalized temperature differential at the centers of the two blocks is depicted as a function of the wall coverage percentage by heating elements. The curve starts at

0 at 10% coverage, indicating the best situation with the least central temperature difference experienced by the centers of the two blocks over the process. As the wall coverage increases, the temperature differential increases steadily, reaching a normalized value of 1 at about 100% coverage, indicating the worst situation with the highest maximum central temperature differential. This steady increase in temperature differential can be attributed to the distribution of heat within the furnace. As explained in Figure 4.11(a), at lower coverage levels, the heat is more effectively concentrated around the blocks, promoting a more uniform temperature distribution. As the coverage increases, the additional heating elements expose more block surfaces directly, leading to uneven heat distribution and greater temperature differentials at the centers of the blocks. This trend underscores the importance of optimizing the wall coverage by heating elements to achieve uniform internal temperatures within the batch of products.

4.5.4 Optimization Results Comparison

Building on the polynomial representations constructed to model the performance parameters as a function of the wall coverage by the heating elements in the Phase-2 Analysis, advanced multi-objective optimization algorithms were subsequently utilized to determine the optimal wall coverage percentages that concurrently minimize these polynomial representations. Among the seven polynomial curves, four show their minimum at 10% coverage, two at approximately 20%, and one at 100%. This distribution, along with considering equal importance for all objectives, influences the genetic algorithm to select 10% as the optimal coverage due to its systematic approach to multi-objective optimization. Similarly, the Pareto search algorithm, which balances trade-offs differently, selected 14.2% as the optimal coverage. Both algorithms converged on optimal values ranging narrowly from 10% to 14.2%, which markedly deviates from the original 70% wall coverage, suggesting a critical reassessment of the conventional layout.

Table 4.6 presents a comparative analysis, indicating performance improvements at both optimized wall coverage percentages when benchmarked against the baseline condition

(TSWE-70). The enhancements achieved by both algorithms are notably close, despite the differences in their methodological approaches and the multifaceted trade-offs involved, as depicted in Figure 4.11. Based on Table 4.6 values, the improvements at the selected optimum wall coverages are almost the same. However, the 10% wall coverage determined by the genetic algorithm was slightly more effective in reducing temperature differentials for the upper block, whereas the 14.2% wall coverage identified by the Pareto search algorithm provided slightly better results in minimizing temperature differentials for the lower block.

Comparative analysis shows that the 10% coverage is about 4.5% better in temperature uniformity across the batch of products compared to the 14.2% coverage. This finding is particularly significant from a product manufacturing point of view, as it promises more consistent products quality. These optimizations suggest that adjusting the wall coverage percentage by heating elements in the TSWE layout can result in a substantial reduction in performance anomalies. Specifically, surface non-uniformities and surface-to-center temperature differentials can be expected to decrease by 4.0 to 7.8 percent, and centers temperature differential can reduce by as much as 70.6 percent. Such rectifications promise notable enhancements in the homogeneity of final properties across individual blocks and an entire batch of products.

Table 4.6 Percentage deviations of performance parameters for each case compared to TSWE-70

Wall Coverage	**Maximum surface non-uniformity-UB**	**Maximum surface non-uniformity-LB**	**Maximum surface-to-center temperature differential-UB**	**Maximum surface-to-center temperature differential-LB**	**Maximum centers temperature differential**
10 %	-7.8	-4.0	-5.8	-5.9	-70.6
14.2 %	-7.4	-4.2	-5.5	-6.2	-66.1

Figure 4.12 depicts the temperature contours within two large blocks at the 50,000-second moment, or approximately one-third of the total tempering process duration, offering insights

into the temperature distribution across the mid-cross-section influenced by varied walls coverage by heating elements. Figure 4.12(a) illustrates the result of the heating elements layout with 10% wall coverage, revealing a gradual and even temperature gradient from the surface to the center of both blocks. This is characterized by a predominant temperature span of 435°C to 485°C in both blocks, with notably similar central temperatures indicating a uniform heat distribution beneficial for the tempering process. In contrast, the 70% wall coverage layout result shown in Figure 4.12(b), which represents the original condition, exhibits a wider temperature spectrum across the surfaces, particularly for the lower block, ranging from approximately 420°C to nearly 500°C. Moreover, the temperatures at the center of the two blocks differ markedly, reflecting a pronounced thermal imbalance. These variations underscore the enhanced heating performance achieved through the TSWE-10 layout, which promotes a more homogeneous temperature field during the non-isothermal tempering cycle, as opposed to the disparate conditions observed with the original heating elements configuration. These insights could inform not only the design of new furnaces but also the development of future tempering process cycles, leading to reduced non-uniformities in heat treated materials by ensuring a more homogenous thermal profile.

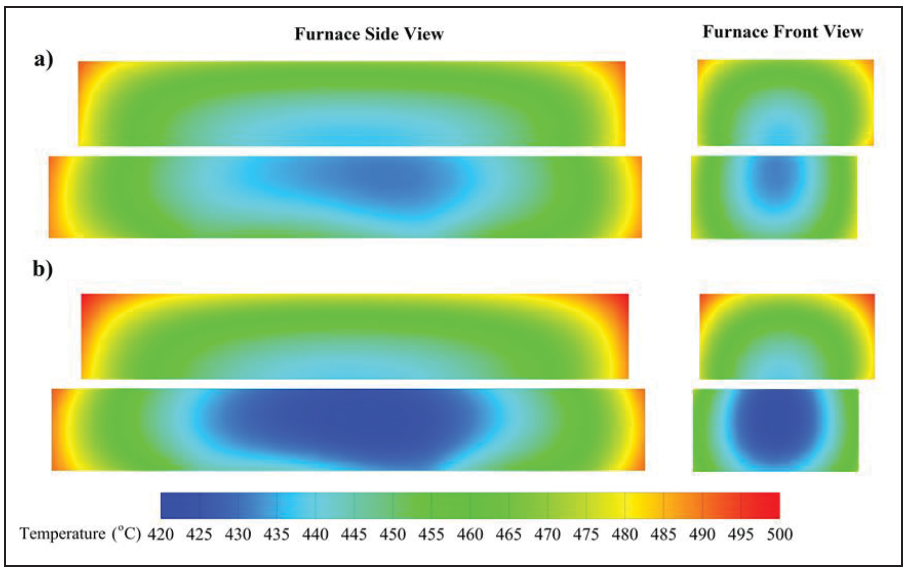

Figure 4.12 Temperature contour of loaded blocks at the central cross-section at t=50,000 s (one-third of total process duration): a) TSWE-10 b) TSWE-70

4.6 Conclusions

In the present investigation, the influence of heating elements layout on the uniformity and quality of heat-treated products in an industrial-scale electrical tempering furnace was examined using a combination of experimental and simulation tools. The key insights are:

1. The developed CFD model, incorporating the turbulence k-ε realizable model, DO radiation model, MRF model, and pre-calculated, temperature-dependent thermophysical properties, has proven to be a reliable representation of the electric heat treatment furnace under investigation.
2. The current layout of the heating elements, two Side walls equipped (TSWE) with heating elements, exhibits the lowest surface non-uniformities and minimized surface-to-center temperature differential for both blocks compared to other typical layouts for this furnace type.
3. The TSWE layout demonstrates the smallest differential in centers temperature for a batch of products at any given moment, compared to other investigated layouts.
4. Correlation between the performance parameters of the electric furnace and the walls' coverage by heating elements was determined.
5. Through the use of multi-objective optimization algorithms, optimal coverage values for the furnace's side walls by the heating elements were identified, ranging from 10% to 14.2%. This finding significantly diverges from the conventional 70% wall coverage, necessitating a critical reassessment of the standard layout.

In future research, the metallurgical aspects of the improved tempering process in an electric furnace will be explored to achieve a better understanding of heat treatment processes.

CRediT authorship contribution statement

Sajad Mirzaei: Conceptualization, Methodology, Visualization, Formal analysis, Validation, Writing – original draft, Writing – review & editing. **Nima Bohlooli Arkhazloo:** Methodology, Writing – review & editing. **Jean-Benoit Morin:** Resources, Writing – review

& editing. **Mohammad Jahazi:** Supervision, Conceptualization, Resources, Writing – review & editing, Project administration, Funding acquisition.

Declaration of competing interest

The authors declare that they have no known competing financial interests or personal relationships that could have appeared to influence the work reported in this paper.

Data availability

The data that has been used is confidential.

Acknowledgments

The authors express their sincere appreciation to Finkl Steel, particularly the research and development and heat treatment teams, for supplying the large blocks and for their contributions in instrumentation and measurements for this research. Special thanks to the Digital Research Alliance of Canada for providing access to high-performance clusters, vital for our high-computational simulations, and their great support team.

Funding

This research was financially supported by Mitacs under the grant [IT27097].

CHAPTER 5

LOADING DATA-DRIVEN DECISION SUPPORT FOR FURNACE LOADING IN STEEL TEMPERING: A MACHINE LEARNING APPROACH BASED ON INDUSTRIAL OPERATIONS

Sajad Mirzaei [a], Jean-Benoit Morin [b], and Mohammad Jahazi [a]

[a] Département de Génie Mécanique, École de Technologie Supérieure, Montréal, Quebec, Canada H3C 1K3
[b] Finkl Steel Inc., 100 McCarthy, Saint-Joseph-de-Sorel, Quebec, Canada J3R 3M8

Paper submitted for publication, May 2025

Abstract

This study develops a machine learning (ML)-based decision-support model to assist in planning loading cycles for large-scale electric tempering furnaces in steel manufacturing. Addressing the limitations of experience-driven approaches, a data-driven framework was introduced using real-world production data from 1,162 tempered forgings. The model incorporates eight input features—capturing physical dimensions, material grouping, and process parameters—and applies a tree-based, multi-output Xtreme Gradient Boosting Regressor (XGBRegressor) algorithm. Cross-validation and test-set evaluations demonstrated strong predictive performance, with R^2 scores of 0.74, 0.88, and 0.87 across three critical batch-level targets: Total Weight, Forging Count, and Total Length. Post-processing analyses, including feature importance rankings and Partial Dependence Plots (PDPs), highlighted the dominant influence of forging shape and width on loading configurations, while predefined process parameters such as temperature and holding duration showed limited impact. The model also identified interpretable thresholds in block dimensions, offering practical guidance for managing new or irregular loading scenarios. This framework enhances planning consistency, reduces reliance on subjective decision-making, and provides a foundation for

integrating ML-driven support into industrial furnace operations without replacing technician expertise.

Keywords: Heat Treatment, Furnace, Loading Cycle, Xtreme Gradient Boosting Regressor, Machine Learning.

5.1 Introduction

In the steel manufacturing industry, tempering is a critical post-forging step that directly influences product quality and mechanical properties. During this phase, previously quenched blocks or cylinders are reheated to controlled temperatures and durations to relieve residual stresses and optimize toughness and hardness (Totten, 2006). Despite its standardized goals, tempering remains highly sensitive to the loading configuration inside the furnace, where an improper grouping of forgings can cause inconsistent heating, non-uniform properties, increased energy consumption, and product rejection at quality control (QC) stages (Committee, 1991; Rakhit, 2000).

At the industrial partner of this study (Finkl Steel Inc., 2021), three 112 m^3 electric tempering furnaces operate daily, each consuming up to 8–10 MWh per cycle or about 150 kWh per metric ton of treated steel. Technicians rely on their experience to group forgings of different sizes, shapes, and material grades into loading batches. These batches define a “loading cycle”—a unique combination of total block weight, physical dimensions, shape types (cubic or cylindrical), material homogeneity, and required tempering time and temperature. Notably, the target temperature and duration vary by steel grade—Finkl processes over 26 different materials—which adds significant complexity to decision-making. This planning is typically performed manually, guided by empirical expertise, and encoded into “furnace loading sheets.” When these subjective strategies fail to ensure uniform tempering, blocks may be rejected after QC testing, resulting in energy waste and financial loss.

Although Computational Fluid Dynamics (CFD) has been applied in past studies to assess heat transfer and stacking effects, its utility is limited by prohibitive runtimes. A single 3D transient simulation for a 48-hour tempering cycle may require over 72 hours of calculation on 64 CPU cores to complete, making it impractical for real-time support (Mirzaei et al., 2023; Mirzaei, Arkhazloo, Morin, & Jahazi, 2024). Additionally, such simulations demand detailed geometric inputs and well-characterized boundary conditions, which are rarely available in daily operations. These limitations underscore the need for an alternative tool—one that can learn from past successful operations and provide predictive insight even in non-standard or edge-case scenarios.

Machine Learning (ML) has shown significant promise in manufacturing through its ability to model complex relationships, uncover hidden patterns, and generate interpretable predictions from noisy or incomplete data. Accordingly, ML has gained increasing attention across the steel industry, particularly for tasks involving properties prediction and defect detection. To begin with, Cui et al. (Cui et al., 2023) combined ML with metallurgy principles to predict hot-rolled steel properties. They reduced feature dimensionality via domain knowledge and trained an Artificial Neural Network (ANN), improving the prediction of tensile metrics. This integration of metallurgical features yielded higher accuracy than purely data-driven models, highlighting the benefit of expert-informed ML architectures. In a similar direction, Adhikary (Adhikary, 2021) developed a data-driven model to estimate the tensile strength of low-alloy steel using composition and temperature variables. Several algorithms were evaluated, including XGBoost, Random Forest, SVM, and ANN. The study showed that tree-based models, particularly XGBoost (R^2:98.63%), can effectively support materials design without extensive physical testing. However, the work focused solely on predicting a single mechanical property and did not explore the integration of ML into broader operational decision-making frameworks. Likewise, Mamun et al. (Mamun et al., 2021) proposed a hybrid creep rupture life prediction framework for high-temperature alloys, combining a variational autoencoder with an XGBoost predictor. The model’s SHAP interpretations aligned with known creep-life formulas, ensuring physical consistency. This approach improved long-term life predictions while offering insight into key influencing factors. Mamun et al.'s study highlighted

XGBoost's ability to handle complex relationships and enhance model reliability, particularly in data-scarce industrial scenarios. Similarly, Choi (Choi, 2019) applied XGBoost within a data-driven framework to predict steel fatigue strength using 25 features. Achieving R^2 = 0.985, the study highlighted the superiority of boosting algorithms over other ML methods. Choi's work also underscored the role of statistical inference in feature evaluation but did not extend to operational decision-support contexts. A similar emphasis on ensemble boosting and interpretability was demonstrated by Feng Yan et al. (Yan, Song, Liu, Chen, & Chen, 2020), showing that heat treatment parameters, along with chromium and carbon content, were key factors influencing fatigue strength. Their integration of ML with explainability tools provided actionable insights for material design, highlighting the value of interpretable ensemble methods in metallurgical applications.

With a focus on defect detection, several studies have applied ML to improve steel quality. Takalo-Mattila et al. (Takalo-Mattila et al., 2022) Introduced an explainable steel quality monitoring system using gradient-boosting trees. Using 89 process features, their model predicts slab surface defect occurrence early in production. The system detected >50% of defects by flagging only ~10% of products as at-risk, enabling targeted quality control. SHAP analysis further linked process parameters to defect formation. Their model significantly improved early detection, though it targeted inspection outcomes rather than production planning. Similarly, Ji et al. (Y. Ji et al., 2024) developed an XGBoost model using 15,000 samples to predict slag entrapment defects in continuous casting. Hyperparameters were optimized via Bayesian, PSO, and GA methods, with Bayesian tuning yielding the highest AUC (0.811) and accuracy (75.6%). SHAP-based feature analysis identified oscillation frequency, mold flux type, casting speed, etc., as dominant factors influencing slag inclusions , thus guiding operators toward defect-mitigating settings. Their analysis enabled real-time defect mitigation but did not address planning-level heat treatment operations. Likewise, Park and Youm (Park & Youm, 2023) applied an XGBoost model to over 5 million historical records and process parameters to predict quality outcomes in die casting, demonstrating how data-driven methods enhance quality control in experience-based manufacturing environments.

Turning to mechanical property prediction, Li et al. (Li, Guiqin, Xihang, Lixin, & Mitrouchev, 2024) compared XGBoost, SVM, and ANN models for predicting steel tensile strength from composition and processing parameters. XGBoost achieved the best generalization ($R^2 \approx 0.97$) and lowest error, outperforming SVM and ANN approaches. This study confirms that gradient-boosted trees can capture complex composition–property relationships more effectively than traditional ML models. Consequently, it reinforces the current study's choice of XGBoost for modeling batch-level furnace loading behavior. In a comparable scope, Wang et al. (Z. H. Wang, Huang, Liu, & Wang, 2023) built an industrial-data-driven XGBoost model to predict strip crown (profile thickness) in hot rolling. By incorporating key process variables and shape control theory, their model attained $R^2 = 0.971$ on test data, exceeding other ML models including Random Forest (RF), Support Vector Machine (SVM), and Multi-Layer Perceptron (MLP). The XGBoost approach proved capable of accurately forecasting the final strip crown, facilitating real-time mill adjustments for shape control. Chen et al. (J. X. Chen et al., 2019) implemented a large-scale (on over 17,000 samples) XGBoost-based system to predict the mechanical properties of steel products in production. XGBoost's efficiency on big data-enabled rapid training on the plant's extensive dataset. The model delivered high-accuracy property predictions across diverse steel grades, demonstrating how big-data ML can enhance throughput and quality control in steel manufacturing. Both studies emphasized prediction accuracy at scale but did not address decision-making tasks such as loading arrangements or furnace cycle planning.

Studies related to furnace temperature and energy modeling further emphasize ML's utility for operational insight. Zhou et al. (Zhou et al., 2021) employed gradient boosting methods (XGBoost and LightGBM) to model the endpoint temperature of molten steel in a vacuum-degassing furnace. Their heterogeneous ensemble improved prediction accuracy over conventional empirical models, using 33,031 records achieving a ±10°C accuracy range, helping operators hit target temperatures more consistently. The result is a decision-support tool that refines secondary refining temperature control via ML. Similarly, Manojlović et al. (Manojlović et al., 2022) analyzed electric arc furnace (EAF) energy efficiency using an XGBoost model with SHAP explainability. By training on EAF process data, they identified

the most influential operational parameters on energy consumption (e.g., oxygen usage, tap weight). The SHAP-enabled model provided insights for engineers, supporting data-driven adjustments to improve EAF electrical efficiency without compromising production. This study focused on thermal or energy metrics, not furnace scheduling or loading decisions. In parallel, Chen et al. (C. Chen et al., 2022) proposed a heterogeneous ensemble learning framework for ladle furnace steel temperature prediction. By stacking multiple base learners (including boosting and neural nets), they achieved more robust accuracy than any single model for end-of-refining temperature forecasts. This ensemble system offers reliable decision support for furnace temperature control, adapting to varying process conditions better than stand-alone models. Their use of ensemble methods, akin to techniques such as XGBoost and Random Forest, underscores the effectiveness of these algorithms in handling complex, nonlinear relationships within metallurgical processes.

In terms of scheduling and real-time operational support, Kim et al. (Kim, Choi, & Ryu, 2022) developed an ML-driven scheduling system for batch heat treatment. They combined a decision-tree learned model (for predicting feasible temperature ranges) with an evolutionary algorithm to optimize furnace loading sequences under spatial and process constraints. In simulations on real factory data, the ML-generated schedules achieved higher throughput and lower energy use than expert plans. This optimization-centric work illustrates the potential for ML to plan heat-treatment operations, whereas the current study focus is on supporting configuration decisions within existing scheduling practices. Complementarily, Zippo et al. (Zippo et al., 2025) deployed a self-updating ML system for predicting final mechanical properties (like yield strength) in a steel plant's production line. Their workflow integrates data preprocessing, model training, and prediction into the plant's quality control software. Comparing various algorithms (regression, ANN, boosting, etc.), the ensemble model achieved high accuracy (R^2 near unity) across multiple steel grades. This industrial case study demonstrates how ML models can be embedded into manufacturing processes to minimize scrap and ensure consistent product quality, aligning with current study decision-support aims. Finally, beyond ML, Jahazi et al. (Nima Bohlooli Arkhazloo et al., 2021) used 3D CFD simulations and experiments to evaluate how furnace loading configurations affect the heat

treatment of large steel forgings. They found suboptimal loading can cause severe thermal non-uniformity (up to 331 K). By optimizing the load pattern, their study reduced temperature non-uniformity by ~32% and cut furnace residence time by 15%. These results highlight that adjusting batch layout can significantly improve heating consistency – a motivation for the current data-driven approach to furnace loading decisions.

Despite recent progress, no existing work has developed or validated a machine learning–based decision-support model for predicting tempering furnace loading cycles using real production data. Specifically, previous studies have not addressed the empirical estimation of batch-level parameters—such as total weight, number of forgings, and occupied furnace length—which are critical to technician planning. While models have targeted property prediction, temperature control, or defect detection, they rarely account for the combinatorial complexity of operational decision-making. Moreover, prior research frequently relies on synthetic or idealized datasets, lacking the irregularity, variability, and noise characteristic of actual industrial operations. In contrast to classical optimization approaches, the current framework aims to replicate feasible, historically successful loading strategies by capturing the logic embedded in expert technician behavior. This research proposes an ML framework trained on actual tempering cycles from three high-capacity electric furnaces, with the objective of learning underlying technician strategies for batch loading. The model is designed to infer how expert planners balance material variety, shape-specific stacking constraints, and batch-level homogeneity. Rather than replacing technician expertise, the system serves as a decision-support tool that reduces planning uncertainty—particularly in the presence of irregular or non-standard forgings. By digitizing historical decision patterns, the proposed model promotes operational consistency, improves the likelihood of quality control acceptance, and may reduce energy waste by avoiding suboptimal grouping. To the best of the authors' knowledge, this is the first study to address furnace cycle planning in industrial heat treatment through an ML lens using real-world, technician-validated production data. The following sections present the methodology, data preparation, model training, evaluation approach, and interpretation of results compared to historical technician records.

5.2 Methodology

5.2.1 Data Collection

The dataset used for model development was acquired from Finkl Steel (Sorel, Quebec), covering operations from three electric tempering furnaces, over a nine-month production period. Every recorded tempering cycle includes technician-defined loading parameters and physical characteristics of individual forged blocks. A total of 1,162 samples were collected, each representing a forging involved in a furnace loading cycle. The dataset is structured into 11 columns: 8 input features (6 numerical, 2 categorical) and 3 output targets. Table 5.1 provides a summary of each variable. The outputs correspond to technician-defined batch-level parameters, while the inputs describe the properties of individual forgings. These batch-level targets are: Total Weight, which refers to the combined mass (kg) of all forgings included in a loading cycle; Forging Count, representing the total number of individual forgings placed in the furnace for a given cycle; and Total Length, denoting the cumulative length (cm) occupied by these forgings inside the furnace chamber.

Input features characterize each forging's physical or process-related attributes. Categorical variables include Shape, defined as either "Cylindrical" or "Cubic", and Material Homogeneity, which indicates whether an individual forging, at the time of planning, is anticipated by technicians to be grouped with forgings of identical ("Same") or different ("Mix") material grades. This anticipatory variable was included to explicitly reflect technicians' operational considerations regarding thermal compatibility and batch homogeneity. Numerical features include process specifications such as Holding Duration (hr) and Temperature (°C), which are pre-set based on steel grade, as well as physical attributes like Weight, Width, Thickness, and Length, all measured per individual block. Additionally, Figure 5.1(a) illustrates typical block loading configurations, Figure 5.1(b) depicts the specific tempering furnaces used, and Figure 5.1(c) provides an overview of the methodology framework.

Table 5.1 Overview of input features and targets in the dataset

Data Type	Names	Description
Numerical Features	Holding Duration (hr), Temperature (°C)	Predefined tempering parameters assigned based on steel grade.
	Weight (kg), Width (cm), Thickness (cm), Length (cm)	Physical attributes of each forging.
Categorical Features	Shape (Cylindrical, Cubic)	Geometry of the forging.
	Material Homogeneity (Mix, Same)	Anticipated grouping condition (same/different material grade).
Targets	Total Weight (kg), Forging Count, Total Length (cm)	Batch-level loading cycle parameters set by technicians.

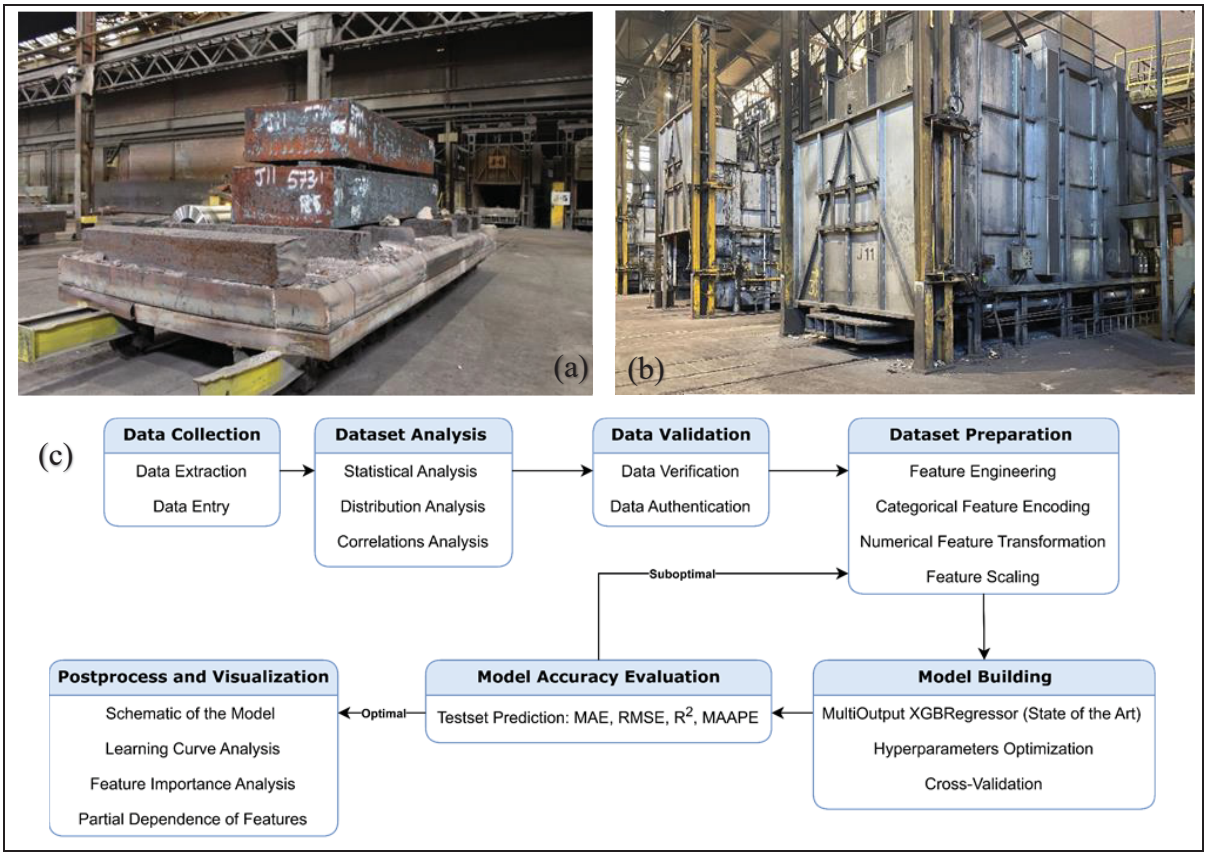

Figure 5.1 (a) Examples of block loading configurations in an electric tempering furnace (b) exterior view of the electric tempering furnaces (c) overall framework of the approach

5.2.2 Dataset Analysis and Validation

A statistical analysis was conducted to evaluate data distribution, variance, and potential outliers across all features. The goal was to ensure that each feature followed expected patterns while preserving the real-world variability inherent in industrial data. Quantitative checks were carried out on the mean, standard deviation, mode, and range of each feature. These were complemented by histogram analysis and Q-Q plots to assess distribution symmetry and identify anomalies (Golmohammadi & Aryanpour, 2023).

Importantly, outliers were not removed arbitrarily. Suspected anomalies were cross-verified using operational records. A data point (sample) was excluded only in cases of confirmed transcription error or sensor malfunction. Otherwise, all samples, including those with high residuals, were retained to preserve the complexity of real industrial processes and to ensure the model would generalize well to irregular or edge-case scenarios.

5.2.3 Mathematical Insights and Model Foundation

The predictive modeling approach is grounded in gradient boosting, utilizing the multi-output XGBRegressor, which constructs ensembles of decision trees to minimize a differentiable loss function. Before selecting XGBoost, alternative machine learning algorithms such as ANN and Linear Regression were tested. These models failed to capture the dataset's non-linear relationships and consistently yielded poor generalization ($R^2 < 0.70$) across all targets, even after advanced data preparation and preprocessing. In contrast, XGBoost demonstrated substantially better performance, as detailed in Section 3.4. This outcome aligns with recent studies (e.g., Li et al., 2024; Wang et al., 2023; Adhikary, 2021; Choi, 2019) (Adhikary, 2021; Choi, 2019; Li et al., 2024; Z. H. Wang et al., 2023), which emphasize XGBoost's robustness when applied to industrial datasets characterized by heterogeneity, noise, and mixed feature types. These combined empirical findings—from both exploratory testing and literature—justify the methodological choice.

The selection of XGBRegressor was further reinforced by its ability to manage high-dimensional feature interactions, integrated regularization to mitigate overfitting, and effective handling of missing or sparse data, making it particularly suited for dynamic production environments (T. Chen & Guestrin, 2016). Given these clear performance advantages and established precedent in industrial applications, extended benchmarking against simpler models was deemed unnecessary, as their limitations were evident within this context.

5.2.4 Data Preparation and Preprocessing

During the data preparation and preprocessing phase, a set of essential techniques was applied to format the dataset for modeling and enhance predictive accuracy and reliability (Y.-x. Liu et al., 2023). Categorical features were processed using One-Hot Encoding (OHE), which converts each category into a binary matrix, ensuring compatibility with machine learning algorithms. This step was particularly important in the present study, where loading decisions depend on categorical variables (e.g., shape and material homogeneity), and preserving their non-ordinal nature was critical to avoid misleading the model (James et al., 2013).

For numerical variables, the Yeo-Johnson transformation was applied to mitigate skewness and kurtosis, a common requirement for many ML algorithms (Kuhn & Johnson, 2013; Yeo, 2000). This technique transforms the data into a distribution that better aligns with model assumptions of linearity and homoscedasticity, particularly benefiting features like Holding Duration, Weight, and Thickness, which initially exhibited non-Gaussian behavior. The efficacy of this transformation is evidenced by the improvements in distribution symmetry and reduction of heavy tails, as detailed in the results section.

Feature scaling was then performed using RobustScaler (Pedregosa et al., 2011), which centers features on the median and scales them based on the interquartile range (IQR). This method effectively mitigates the influence of extreme values. As discussed in Section 3.3, features such as 'Total Weight' and 'Total Length' were characterized by high variability and extreme values. While these extremes were valid, they could distort model training if not appropriately scaled.

5.2.5 Model Building and Hyperparameter Optimization

The XGBRegressor model was configured to predict three targets simultaneously using a multi-output strategy. Key hyperparameters including n_estimators, learning_rate, max_depth, subsample, and colsample_bytree were tuned through an exhaustive grid search with 5-fold cross-validation to identify the optimal configuration (Wei, Ji, Li, & Song, 2023). Grid search systematically explored the parameter ranges listed in Table 5.2, using repeated cross-validation to identify the best-performing configuration (Takalo-Mattila et al., 2022). A 5-fold cross-validation strategy partitioned the dataset into five equal subsets, with each subset serving once as the validation set while the others formed the training set (C. Chen et al., 2022; Cui et al., 2023). This process provided a robust performance estimate across data partitions and ensured strong generalizability of the model, an essential attribute for reliable deployment in real-world industrial scenarios (Hastie et al., 2009).

The parameter n_estimators, which defines the number of decision trees in the ensemble, was optimized to 675. The learning_rate, determining the contribution of each tree, was set at 0.0125 to balance convergence speed with generalization capability. The max_depth of individual trees was limited to 11, preventing overfitting by restricting model complexity. Additionally, the subsample ratio—indicating the fraction of training instances used per tree—and colsample_bytree—defining the proportion of features considered at each split—were tuned to 0.85 and 0.6, respectively. These values introduced controlled randomness into tree construction, promoting robustness and mitigating overfitting.

Table 5.2 Optimal hyperparameters identified through grid search and cross-validation

Hyperparameters	Range	Step	Optimum Value
n_estimators	[100 - 2000]	25	675
learning_rate	[0.0125 - 0.2]	0.0125	0.0125
max_depth	[5 - 15]	1	11
subsample	[0.1 - 1]	0.05	0.85
colsample_bytree	[0.1 - 1]	0.05	0.6

5.2.6 Model Evaluation

During model evaluation, the primary objective was to minimize overfitting and enhance the model's generalizability to unseen data. The XGBoost model was trained using mean squared error (MSE) as the loss function, which assigns greater weight to larger errors (Lai, Demartino, & Xiao, 2024; Lim & Chi, 2019). For hyperparameter tuning, the R^2 score was used as the evaluation metric during cross-validation with the training dataset. This ensured that hyperparameter selection maximized the model's ability to explain variance in the training data. The model's performance on the test dataset was evaluated using multiple performance metrics. Mean Absolute Error (MAE) measured the average magnitude of prediction errors. Root Mean Squared Error (RMSE) quantifies the square root of the average squared differences between predicted and actual values, making it more sensitive to outliers. Finally, the R^2 Score indicated the proportion of variance in the target variables explained by the model. Together, these metrics provided a comprehensive evaluation framework, emphasizing the accuracy and reliability of model predictions on previously unseen data (Asgarkhani, Kazemi, Jakubczyk-Gałczyńska, Mohebi, & Jankowski, 2024; Pan & Montreuil, 2021).

5.2.7 Practical Deployment and Limitations

The proposed model serves as a decision-support system, aiming to replicate the empirical logic followed by experienced technicians. At this time, it is not designed to replace human expertise but to enhance consistency and reduce variability in batch loading decisions, especially under non-standard conditions. Importantly, the model is structured for re-training and continuous integration as new operational data becomes available. However, the model has limitations. The current assumes that historical technician decisions represent optimal or near-optimal practices, which may not always reflect the best achievable efficiency. This introduces the potential for embedded biases that may limit generalizability. Moreover, no direct thermal or mechanical measurements were used in model training. Future extensions should integrate explicit physical constraints or further validate predictions through experimental trials to enhance optimization and model robustness.

5.3 Results and Discussion

5.3.1 Dataset Analysis

The descriptive statistical analysis in Table 5.3 presents the distribution characteristics of numerical features and batch-level targets associated with tempering furnace operations. As detailed in Section 2.1, the dataset includes 1,162 samples reflecting variations in individual forging dimensions, process parameters, and technician-defined loading cycles. The feature 'Weight', representing the mass of each individual forging, shows a mean of 10,172.1 kg with a standard deviation (std.) of 9,207.2 kg, across a range of 30,724.1 kg, highlighting variability in forging sizes handled during routine operations. In contrast, 'Total Weight', which captures the cumulative mass per loading cycle, extends up to 120,289.9 kg, reflecting diverse batch configurations applied by technicians to optimize furnace capacity.

Process-specific parameters such as 'Temperature'—the predefined tempering temperature based on steel grade—exhibit controlled variation, with a mean of 591.9°C and a std. of 41.4°C, consistent with operational standards across multiple material types. Similarly, 'Holding Duration', indicating the planned tempering time per forging, ranges up to 42.0 hours, adjusted according to material and batch-specific requirements. Dimensional features like 'Width', 'Thickness', and 'Length' describe the physical attributes of individual forgings, with ranges of 225.8 cm, 117.9 cm, and 718.8 cm, respectively. These values indicate flexibility in accommodating both compact and large-scale forgings, depending on production demands. The 'Forging Count', representing the number of forgings loaded per cycle, varies from 1 to 15 units, reflecting operational strategies to balance furnace occupancy and heat distribution.

The Q-Q plots in Figure 5.2 illustrate that the majority of numerical features and targets deviate from the theoretical normal distribution, particularly for variables such as 'Weight', 'Total Weight', and 'Total Length', where pronounced curvature indicates skewness. Even features like 'Temperature' and 'Forging Count', subject to standardized process controls, exhibit deviations—highlighting the inherent variability characteristic of industrial production data.

The substantial disparity in value scales observed in Table 5.3—such as between individual forging dimensions and cumulative batch targets—necessitated the application of scaling and transformation techniques, as outlined in Section 2.4, to ensure balanced contributions of all features during model training.

Extreme values present across several features represent valid operational cases, including maximum furnace utilization scenarios or atypical forging specifications selected based on client requirements or production schedules. Retaining these values ensures that the developed predictive model remains applicable not only to standard operations but also to rare, high-variance loading cycles, supporting robust decision-making across diverse production contexts. This statistical overview defines the foundational characteristics of the dataset and supports the rationale for the preprocessing strategies implemented prior to model development.

Table 5.3 Descriptive statistical analysis of the original dataset

Dataset Numerical Features	**Mean**	**Std.**	**Range**
Weight (kg)	10,172.1	9,207.2	30,724.1
Temperature (°C)	591.9	41.4	155.6
Length (cm)	414.4	147.3	718.8
Thickness (cm)	49.4	18.1	117.9
Width (cm)	48.6	62.5	225.8
Holding Duration (hr)	19.6	6.9	42.0
Forging Count	6.1	3.7	14.0
Total Weight (kg)	41,759.4	23,011.8	120,289.9

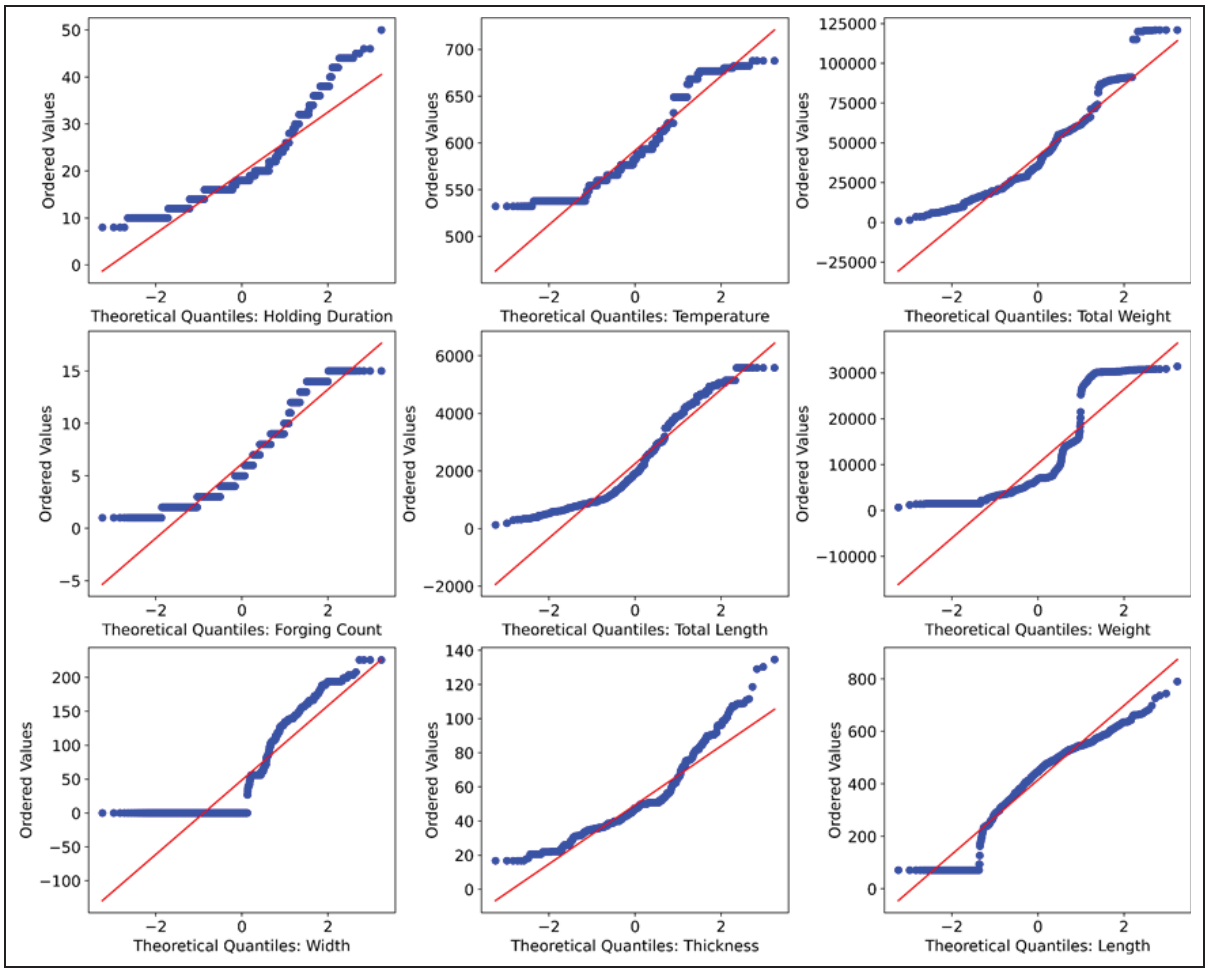

Figure 5.2 Q-Q plot of numerical features and targets in the dataset

5.3.2 Correlation Overview

The Spearman Rank Correlation Coefficient analysis in Figure 5.3 provides insight into monotonic relationships between numerical input features and batch-level targets, reflecting how variations in forging characteristics and process parameters influence technician-defined loading cycles. This non-parametric metric was selected due to its suitability for detecting non-linear associations common in industrial datasets (Q. L. Wang et al., 2024; S. Y. Zhang, Chen, Xu, & Xie, 2024). All observed correlations are statistically significant ($p < 0.05$), confirming that these relationships reflect consistent operational patterns rather than random variation.

The feature 'Weight', representing the mass of individual forgings, shows a strong positive correlation (~0.67) with 'Total Weight', indicating that heavier forgings contribute proportionally to higher cumulative batch weights. This aligns with operational practices where technicians group larger blocks to optimize furnace capacity utilization. Similarly, 'Length' exhibits a positive correlation (~0.44) with 'Total Length', reflecting those longer forgings naturally extend the total occupied length within the furnace. These direct relationships confirm the expected logistical dependencies inherent in batch assembly.

In contrast, features such as 'Width' and 'Thickness' display negative correlations with 'Total Length' (approximately -0.56 and -0.36, respectively). This suggests that increases in cross-sectional dimensions constrain the number of forgings that can be arranged longitudinally, due to spatial limitations and the need to maintain effective heat distribution across the chamber.
The process parameter 'Holding Duration' shows a moderate positive correlation (~0.40) with 'Total Weight', implying that longer tempering times are generally associated with heavier batch loads. This pattern reflects technician adjustments to ensure adequate thermal penetration for larger mass configurations, consistent with empirical operational strategies described in Section 2.1. An observation of note is the weak correlation of 'Temperature' with all output targets, indicating that while temperature is critical for metallurgical outcomes, it plays a limited role in determining loading cycle logistics. This aligns with the predefined nature of temperature settings, which are primarily dictated by steel grade rather than batch composition.

These correlation patterns emphasize the dominance of physical dimensions and process time over thermal parameters in shaping furnace loading strategies. The statistically significant coefficients across multiple features underscore the structured yet non-linear nature of these relationships. The correlation coefficients, supported by consistently low p-values ($p<0.05$), confirm that these relationships are statistically significant and reflective of operational patterns rather than random variation. The mix of positive and negative monotonic trends, alongside varying correlation strengths, illustrates the non-linear nature of interactions within the dataset. This complexity, as discussed in Section 2.3, necessitates a modeling approach capable of capturing such behavior without assuming linearity. Accordingly, XGBoost was

selected due to its proven ability to handle non-linear dependencies and feature interdependencies, where traditional linear models would be insufficient (Adhikary, 2021; Z. H. Wang et al., 2023)

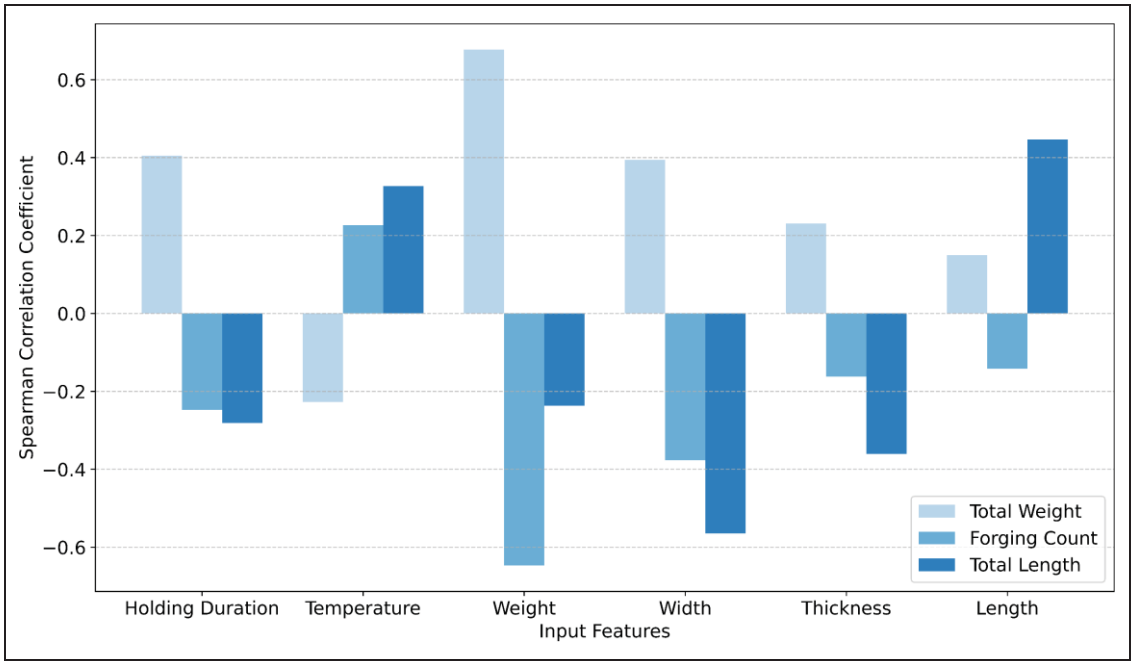

Figure 5.3 Bar chart of Spearman rank correlation coefficients: analyzing the relationship between input features and output variables in a dataset

5.3.3 Dataset Preparation

The initial assessment of the dataset, as illustrated in Figure 5.4 (a) and detailed in Table 5.4, identified pronounced skewness and kurtosis across several numerical features and batch-level targets. Features such as 'Holding Duration' (skewness: 1.46; kurtosis: 2.27), 'Weight' (skewness: 1.29), and 'Thickness' (skewness: 1.25; kurtosis: 1.94) demonstrated clear departures from symmetrical distribution, indicative of heavy tails and potential outliers. These distributional characteristics are typical in industrial datasets, where operational variability and irregular production demands are prevalent.

While tree-based models like XGBoost are inherently robust to non-normal data, excessive skewness, and kurtosis can still introduce instability in feature importance interpretation and model convergence behavior. Addressing these issues was essential to enhance model reliability without discarding valid operational data points. The chosen approach focused on transformation rather than outlier removal to preserve the integrity of edge-case scenarios critical for industrial applicability.

The Yeo-Johnson transformation was applied to adjust for non-normality, given its capability to handle both positive and zero-valued data while reducing skewness and kurtosis. The efficacy of the Yeo-Johnson transformation has been supported by various studies in optimizing data treatment for machine learning applications (K, Krishnan, & Manikandan, 2024; Nwakuya & Nkwocha, 2022; Riani, Atkinson, & Corbellini, 2022), as discussed in Section 2.4. Studies such as those by Kuhn and Johnson (Kuhn & Johnson, 2013) and James et al. (James et al., 2013) further emphasize the importance of addressing skewed distributions to improve model performance and interpretability. As shown in Figure 5.4 (b) and the transformed metrics in Table 5.4, this method significantly reduced skewness across all features—bringing values close to zero—and moderated kurtosis, aligning distributions more symmetrically around their means.

Notably, features such as 'Total Weight', 'Temperature', and 'Holding Duration' exhibited near-symmetrical distributions post-transformation, minimizing the influence of extreme values without eliminating them. This preprocessing step ensured that each feature contributed proportionately during model training, enhancing both robustness and generalizability across diverse operational contexts. The retention of original data variability, including extreme but valid cases, supports the model's ability to perform reliably under standard and atypical loading scenarios. This approach aligns with the practical demands of industrial environments, where rare configurations must be anticipated by predictive systems.

Table 5.4 Skewness and Kurtosis of numerical features and targets before and after transformation

Numerical features and targets	Original dataset		Transformed dataset	
	Skewness	Kurtosis	Skewness	Kurtosis
Holding Duration	1.46	2.27	-0.01	0.28
Temperature	0.70	-0.44	0.00	0.00
Weight	1.29	0.29	0.01	-0.67
Width	0.92	-0.53	0.23	-1.91
Thickness	1.25	1.94	0.00	0.43
Length	-0.87	0.31	-0.31	-0.33
Forging Count	0.76	-0.36	-0.01	-0.87
Total Weight	0.88	0.61	-0.01	-0.22
Total Length	0.62	-0.76	-0.04	-0.96

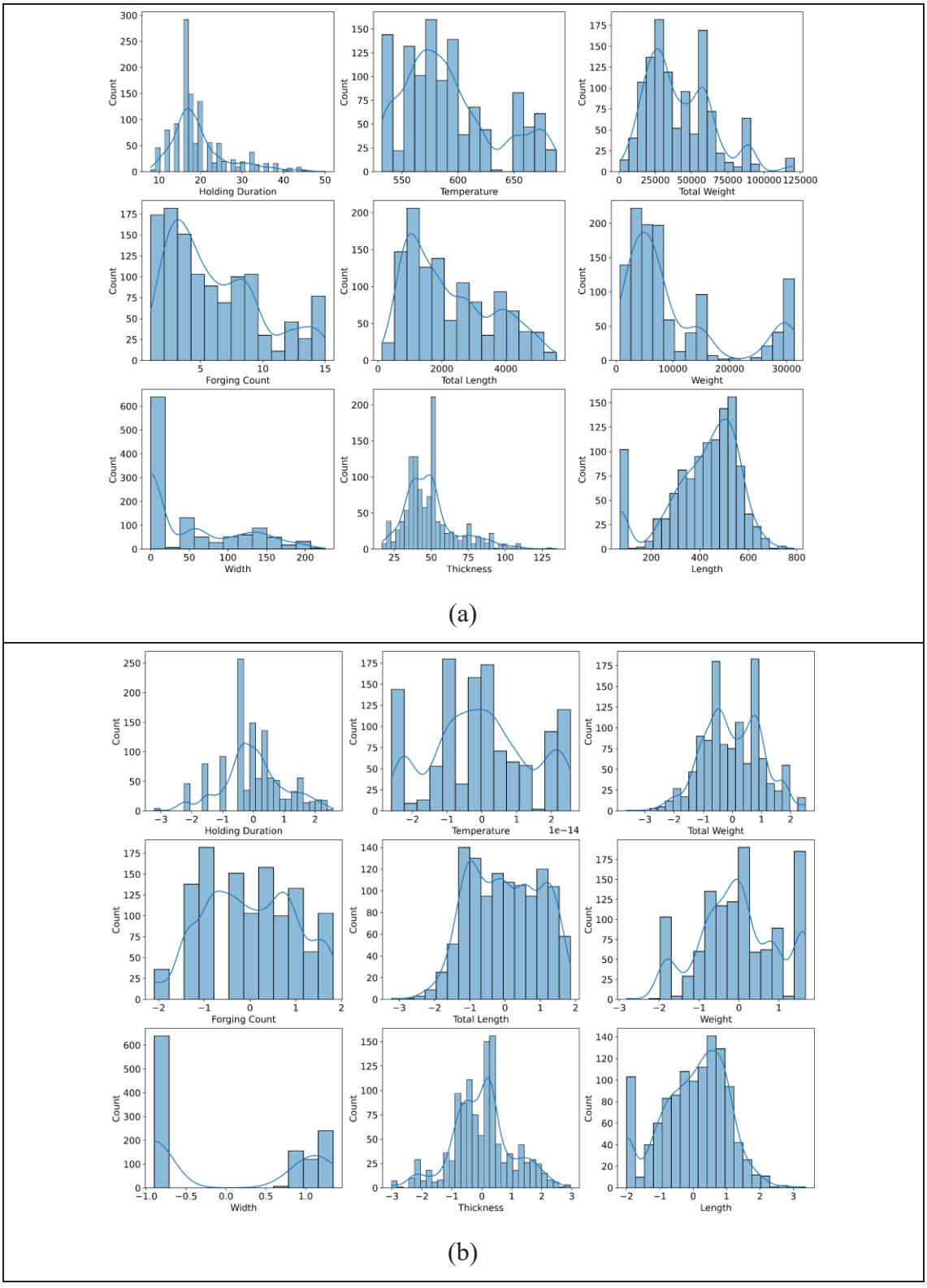

Figure 5.4 Histograms of data distribution: (a) Original data before Yeo-Johnson transformation, (b) after transformation

5.3.4 Model Accuracy Evaluation

The predictive performance of the developed XGBoost model was evaluated using the test dataset, focusing on its ability to generalize across diverse loading scenarios. Figure 5.5 illustrates the relationship between actual and predicted values for the three batch-level targets: 'Total Weight', 'Forging Count', and 'Total Length'. The clustering of points along the diagonal reference line demonstrates the model's effectiveness in capturing underlying patterns within the operational data. As summarized in Table 5.5, the coefficient of determination (R^2) values reached 0.74 for 'Total Weight', 0.88 for 'Forging Count', and 0.87 for 'Total Length', indicating that a substantial proportion of variance in each target is explained by the input features. These results reflect strong predictive alignment, particularly for discrete outputs like 'Forging Count', where the model achieved near-exact estimations across most cases.

The Mean Absolute Error (MAE) values—6,552.1 kg, 0.77 units, and 281.96 cm for 'Total Weight', 'Forging Count', and 'Total Length', respectively—highlight the average deviation between predicted and actual values. These errors are within acceptable operational margins, considering the scale and variability inherent in industrial furnace loading cycles. Complementing this, the Root Mean Squared Error (RMSE) values—10,355.5 kg, 1.23 units, and 453.3 cm—capture the influence of larger discrepancies, which primarily arise in edge cases involving atypical batch configurations or extreme input values, as discussed in Section 3.3. The presence of such cases reinforces the importance of retaining full data variability during preprocessing to ensure model robustness across standard and non-standard conditions. These performance metrics collectively demonstrate that the model provides reliable predictive support for logistical parameters critical to tempering furnace operations. The ability to maintain high accuracy despite non-linear relationships and production noise, as established in Sections 3.2 and 3.3, validates the selection of XGBoost as an appropriate modeling approach. This predictive reliability is essential for industrial deployment, where consistent decision support across variable scenarios can enhance planning efficiency and reduce the likelihood of suboptimal loading configurations.

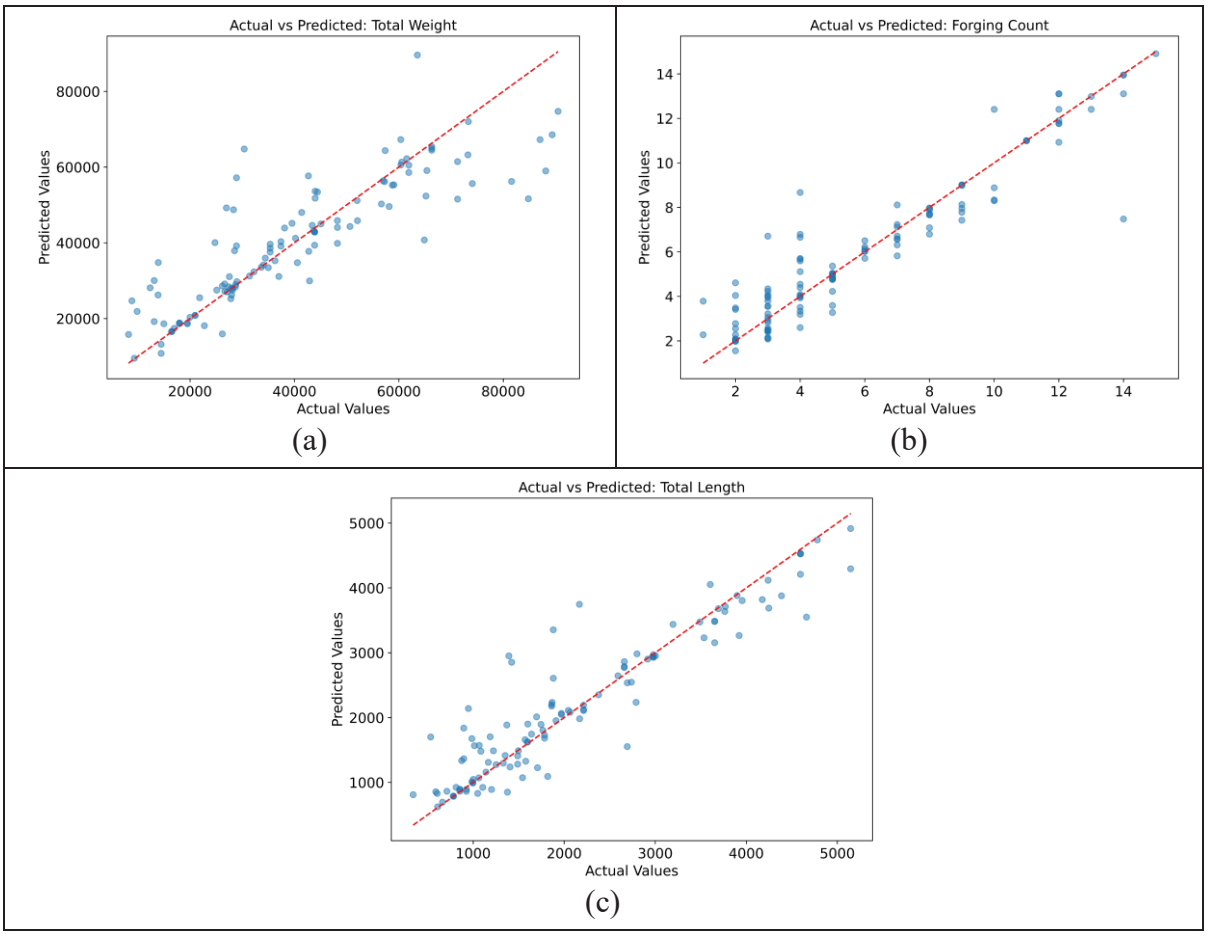

Figure 5.5 Scatter plot of predicted vs. actual test set values for(a)Total Weight (b) Forging Count (c) Total Length by the machine learning model

Table 5.5 Performance metrics for machine learning model predictions on test set

Performance Metrics	**Targets**		
	Total Weight (kg)	**Forging Count**	**Total Length (cm)**
MAE	6552.11	0.77	281.96
RMSE	10355.48	1.23	453.26
R^2 Score	0.74	0.88	0.87

5.3.5 Schematic of the Model

The developed XGBoost ensemble comprises 675 trees per target, reflecting the model's capacity to capture complex, non-linear patterns across batch-level predictions. Figure 5.6 illustrates the first decision tree generated for each target—(a) Total Weight, (b) Forging Count, and (c) Total Length—offering a detailed view into how the model initiates partitioning of the feature space. Despite identical hyperparameters across all targets, notable differences emerge in tree complexity. The first tree for Total Weight consists of 306 nodes, compared to 188 nodes for Forging Count and 268 nodes for Total Length. This variation indicates that predicting Total Weight required more intricate decision rules, aligning with its lower R^2 score (0.74). In contrast, the simpler structure observed for the Forging Count corresponds to higher predictive accuracy ($R^2 = 0.88$), suggesting a more direct relationship between input features and target outcome. Overall, across all 2,025 trees, the ensemble encapsulates approximately 500,000 decision nodes, underscoring the scale of complexity managed by the model.

A closer examination of Figure 5.6(a)–(c) reveals how tree structures visually reflect target-specific complexities. The dense, layered, and relatively symmetrical and evenly branched pattern in Figure 5.6(a) suggests that Total Weight predictions rely on a broad distribution of feature splits, requiring multi-level interactions and conditional dependencies across various dimensions and process parameters. Conversely, Figure 5.6(b) exhibits pronounced asymmetry, with growth skewed predominantly to one side. This indicates that the Forging Count is governed by a few dominant features, where early splits rapidly capture most of the predictive power, leading to shallower and more unbalanced branching. Figure 5.6(c) demonstrates an intermediate structure, where moderate branching depth and balance suggest a mix of linear dependencies and limited feature interactions driving Total Length predictions. These patterns also highlight how depth utilization varies—while the maximum depth is set at 11, many branches, particularly in Figure 5.6(b), terminate early once sufficient predictive accuracy is achieved. It is also noteworthy that subsampling parameters contributed to structural variability across trees, enhancing generalization by diversifying feature splits. As tree complexity increases, interpretability becomes challenging. While smaller trees, such as

that for Forging Count, offer clearer decision pathways, larger trees—like Total Weight—highlight the trade-off between predictive power and transparency. This emphasizes the importance of complementary tools, such as feature importance rankings and partial dependence analysis, discussed in earlier sections, to decode complex models where direct schematic interpretation is limited.

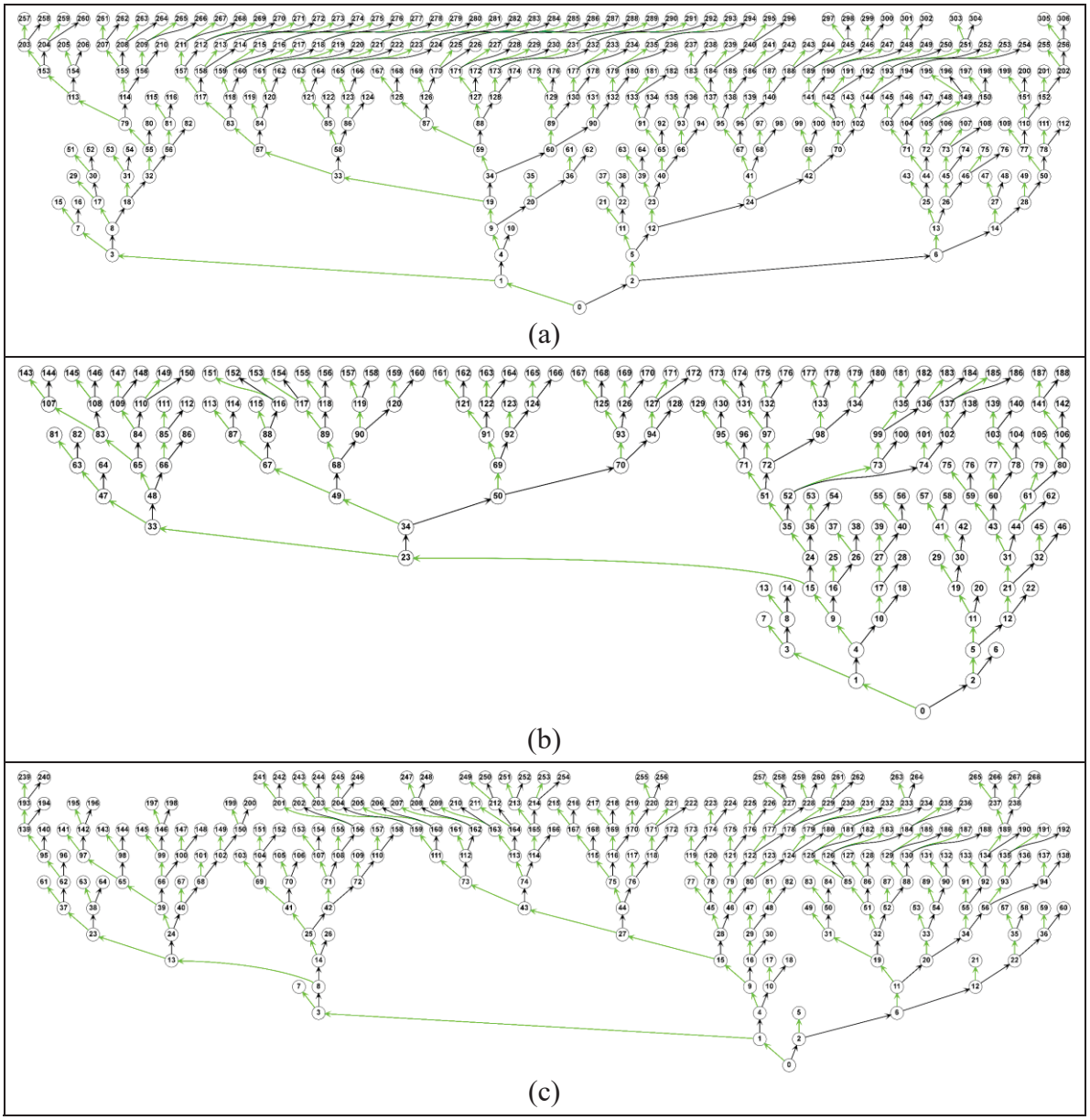

Figure 5.6 Schematic representation of the first decision tree (out of 675) for each target in the XGBoost ensemble: (a) Total Weight, (b) Forging Count, and (c) Total Length

5.3.6 Learning Curve Analysis

The learning curves for each target variable — Total Weight, Forging Count, and Total Length — are presented in Figure 5.7. These curves illustrate the performance of the developed XGBRegressor model as a function of training set size, using a fixed 5-fold cross-validation strategy. For all targets, the training scores remain consistently high (close to 1.0), reflecting a typical overfitting behavior when the model fits tightly to the training data, especially with smaller datasets (James et al., 2013; Kuhn & Johnson, 2013). In contrast, the cross-validation scores show a steady improvement as the number of training examples increases, indicating enhanced generalization capability with more data availability. The green shaded areas represent the standard deviation of cross-validation scores across the folds. As observed, increasing the training set size reduces this variability, particularly noticeable for Forging Count and Total Length, suggesting greater stability and reliability in predictions with larger datasets.

For Total Weight (Figure 5.7a), the cross-validation score improves from approximately 0.51 to 0.74. The reduction in variability up to around 600 samples indicates better consistency; however, a slight increase in variance beyond this point may reflect sensitivity to data complexity. For Forging Count (Figure 5.7b), the model achieves the highest cross-validation score, reaching about 0.82 with minimal variance at larger training sizes, highlighting strong predictive stability for this target. For Total Length (Figure 5.7c), the score rises from 0.46 to approximately 0.78, again showing reduced variability as data increases. These trends align with established machine learning principles, where larger datasets typically lead to improved generalization (Hastie et al., 2009). In this industrial context, the learning curves demonstrate that while the model performs well with current data volumes, marginal gains could still be achieved with additional data, particularly for complex targets like Total Weight.

Notably, when training the final model on the complete dataset (Section 3.4, Table 5.5), the test set R^2 scores for Forging Count and Total Length surpassed the maximum cross-validation scores observed in the learning curves, reflecting these targets' responsiveness to increased

data volume. Conversely, Total Weight remained stable, likely constrained by intrinsic data complexity limiting further performance gains. Overall, the analysis confirms that the developed model transitions from overfitting on smaller datasets to more robust performance as training size increases, providing practical guidance on data sufficiency for predictive modeling in industrial applications.

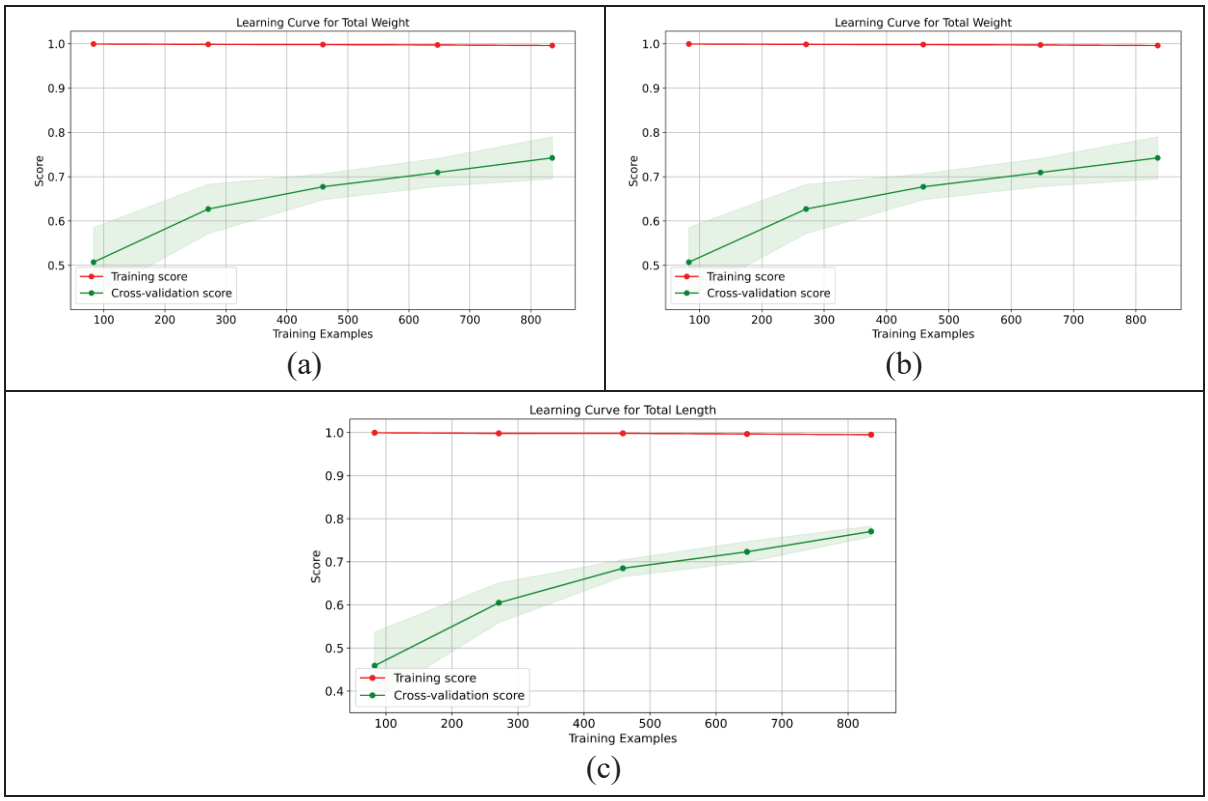

Figure 5.7 Learning curves depicting training and cross-validation scores for (a) Total Weight, (b) Forging Count, and (c) Total Length

5.3.7 Feature Importance Analysis

The feature importance analysis, presented in Figure 5.8, illustrates the relative contribution of each input variable to the XGBoost model's predictions across the three batch-level targets. This analysis is based on the 'gain' metric, which quantifies the improvement in model accuracy

when a feature is used for splitting within the decision trees (Nguyen, Dao, & Shin, 2021; Song, Yan, Ding, Gao, & Lu, 2020).

Categorical variables, particularly 'Shape_Cylinder' and 'Shape_Cubic', consistently show the highest importance across all targets. These features encode the geometric form of forgings, distinguishing between cylindrical and cubic shapes as defined in Section 2.2. The model's reliance on shape reflects operational priorities where technicians must consider how forging geometry impacts spatial arrangement and furnace occupancy during loading cycle planning. Cylindrical forgings, due to their form, often allow for different stacking strategies compared to cubic blocks, directly influencing batch configurations. The feature 'Material Homogeneity_Same', indicating batches composed of identical material grades, emerges as another influential factor, especially for 'Forging Count' and 'Total Length'. This aligns with standard industrial practices where uniform materials facilitate consistent heating protocols, reducing the need for adjustments during tempering cycles (Section 2.1). In contrast, 'Material Homogeneity_Mix'—representing mixed-material batches—shows lower importance, suggesting that homogeneous loads are more predictable in technician-driven configurations.

Among numerical inputs, 'Width'—the lateral dimension of individual forgings—demonstrates a consistent impact across all targets. This reflects its operational relevance, as furnace width constraints directly govern how blocks are positioned. The prominence of 'Width', following categorical factors, underscores its role in spatial optimization, a consideration frequently encountered by technicians during manual loading decisions. Such observations, particularly regarding the influence of 'Width', are not extensively documented in prior literature (N. B. Arkhazloo et al., 2019; Bouissa et al., 2020; Mirzaei et al., 2023), indicating a practical insight revealed through data-driven modeling.

Conversely, process parameters like 'Holding Duration' (planned tempering time) and 'Temperature' (setpoint based on steel grade) exhibit lower importance values (<0.05). As predefined conditions, these variables remain relatively stable within operational ranges and thus have limited influence on batch arrangement predictions. This distinction confirms that

the model primarily interprets logistical configurations based on physical dimensions and categorical attributes rather than fixed process settings.

It is important to recognize that feature importance rankings are influenced by both operational logic and statistical behavior within the dataset. As discussed in Section 3.2, correlations among dimensional features (e.g., 'Width', 'Length', 'Thickness') may distribute importance across related variables. Therefore, while the model captures key factors reflective of technician priorities, these results should be interpreted as indicative of predictive influence rather than direct causation. To further investigate the direct effect of individual features on target predictions—while controlling for interactions—the next section applies Partial Dependence Plots (PDP). This complementary approach addresses limitations inherent in aggregated importance metrics by visualizing marginal effects, offering deeper insights into how specific variables guide model behavior.

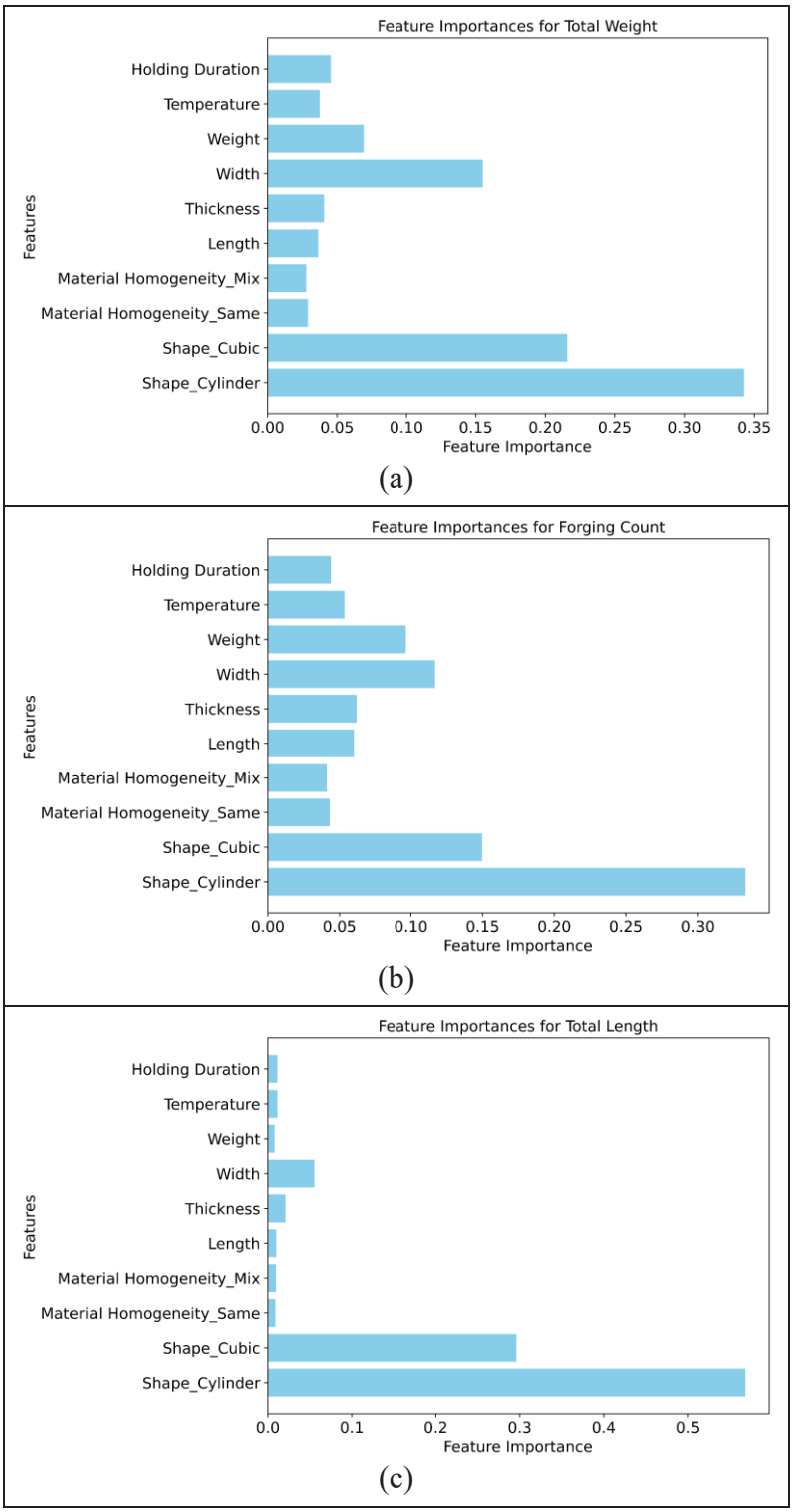

Figure 5.8 Feature importance rankings for (a) Total Weight, (b) Forging Count, and (c) Total Length, illustrating key predictive factors in heat treatment processes

5.3.8 Partial Dependence of Features

The PDPs in Figure 5.9 illustrate how key numerical input features influence the XGBoost model's predictions for the batch-level targets: Total Weight, Forging Count, and Total Length. These plots isolate the marginal effect of each feature by averaging out the impact of all other variables, providing a clearer view of individual feature behavior within complex, non-linear interactions (Y. Ji et al., 2024; Shafighfard, Kazemi, Asgarkhani, & Yoo, 2024; Q. L. Wang et al., 2024). For all targets, PDPs reveal both linear trends and threshold effects, offering insights into how technicians' loading strategies are reflected in the dataset. The horizontal axes display normalized feature values, while the vertical axes represent the average change in predicted outcomes. Small ticks along each axis indicate data concentration zones.

For Total Weight (Figure 5.9a), Weight (mass of individual forgings) shows a clear positive correlation, particularly beyond a normalized value of 0.5, corresponding to approximately 12 tons per forging. While this relationship might appear intuitive, the PDP reveals a non-linear pattern where heavier individual forgings sharply increase total batch weight. This indicates that technicians prioritized loading fewer but heavier blocks—even at the expense of reducing forging count (as shown in Figure 5.1(a))—to optimize furnace occupancy and thermal efficiency. Conversely, lighter forgings did not lead to proportionally higher total weights, due to spatial inefficiencies when accommodating multiple smaller blocks. This behavior, uncovered by the model, highlights operational strategies that are not immediately obvious without such analysis. For Total Length (Figure 5.9c), Length exhibits a strong positive dependence across its entire range, with notable growth beyond a normalized value of 0.6, equivalent to 180 cm. This pattern highlights that batches involving longer individual forgings tend to result in higher total batch lengths. Rather than balancing long forgings with shorter ones to optimize space, the observed loading behavior reflects a tendency to group similarly long forgings, leading to cumulative axial dimensions. This suggests an embedded strategy to maintain uniform heat exposure along the furnace's length—an insight that would not be apparent without data-driven evaluation, as one could assume mixed lengths might better utilize space.

The feature Width demonstrates a distinct threshold effect across all targets (bottom-left subplots). Below a normalized value of 0.8 (approximately 30 cm), partial dependence remains flat, indicating minimal influence. However, beyond this point, Total Weight shows a sharp positive shift, whereas Forging Count and Total Length exhibit negative responses. This suggests that wider blocks trigger adjustments in loading strategies—likely due to spatial constraints—where increased width reduces the number or length of forgings that can be accommodated, affecting overall batch metrics.

For 'Thickness', PDPs across targets show almost modest variations, indicating localized sensitivities but no dominant trend. 'Holding Duration' and 'Temperature' exhibit fluctuating but generally low marginal impacts, consistent with their lower importance observed in Section 3.7, reflecting their role as predefined process parameters rather than logistical drivers. However, PDPs reveal that shorter Holding Durations—those below the first quartile ~15 hours—are associated with reduced batch sizes across all targets. This suggests that technicians occasionally aligned faster tempering cycles with smaller loads, demonstrating operational flexibility to balance production speed with furnace utilization when processing limited quantities.

Flat zones in several PDPs, such as the stable response of Width below 30 cm or Thickness within mid-range values, identify operational ranges where feature variations have limited impact on predictions. These areas suggest that within certain dimensional tolerances, technicians had flexibility without significantly affecting batch-level outcomes.

Overall, these PDP analyses expose nuanced decision patterns embedded in historical loading cycles—revealing that strategies like favoring heavier or longer forgings under specific conditions are neither trivial nor purely geometric outcomes but reflect deliberate operational choices. These insights offer practical guidance for optimizing future furnace loading by identifying critical thresholds where small changes in block dimensions can disproportionately influence batch configurations.

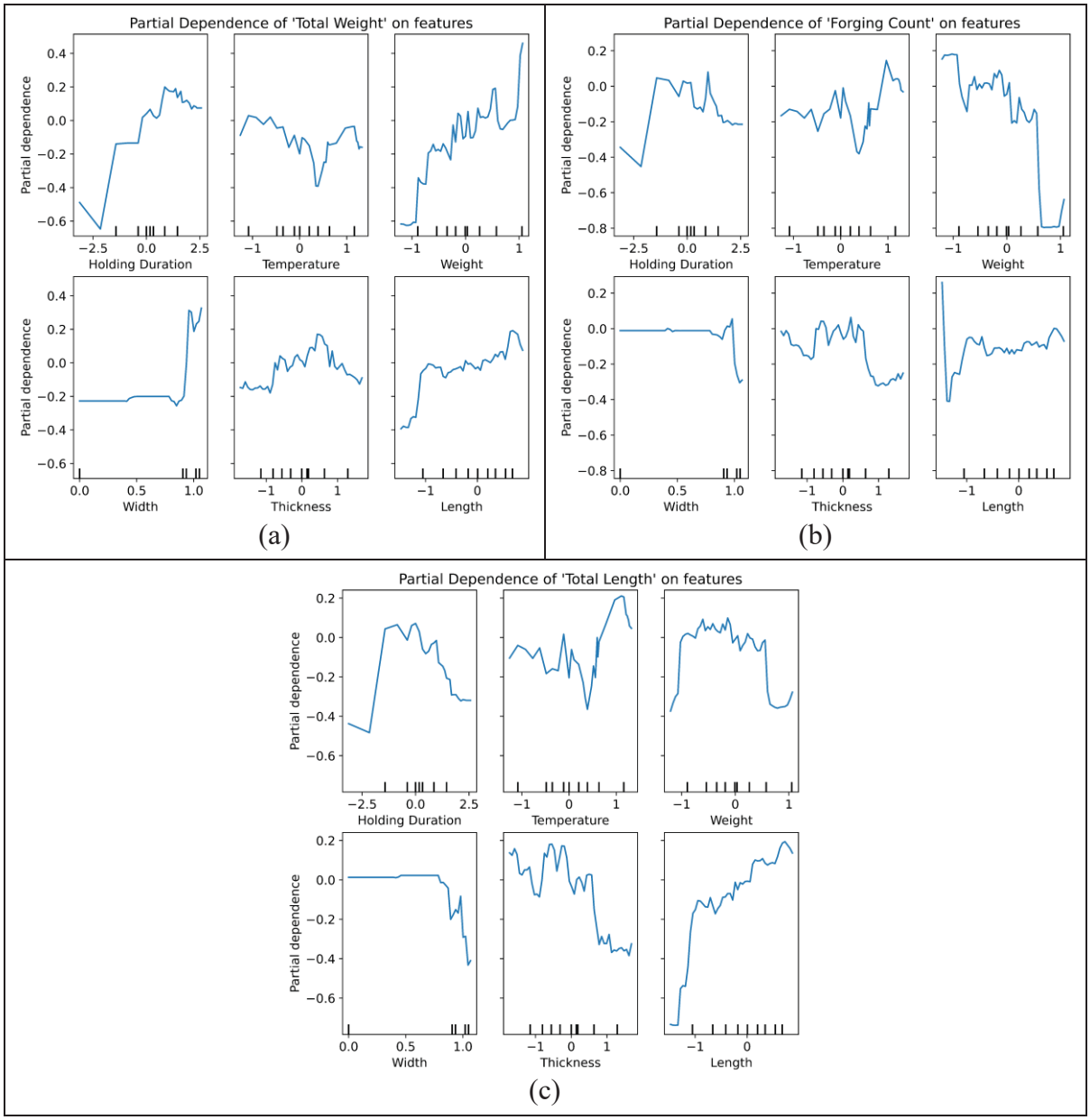

Figure 5.9 Partial dependence plots illustrating the influence of normalized features on the (a) Total Weight, (b) Forging Count, and (c) Total Length

5.4 Conclusions

This study developed a machine learning-based decision-support model using XGBoost to assist in planning loading cycles for large-scale electric tempering furnaces in steel manufacturing. By leveraging real-world production data encompassing physical dimensions, material grouping, and process parameters, the model effectively learned historical technician strategies for assembling batch configurations.

Key findings include:

1. Statistical analysis revealed significant variability and non-normal distributions within operational data—a common challenge in industrial environments—underscoring the need for robust preprocessing techniques such as Yeo-Johnson transformation and scaling to ensure model stability and learning effectiveness.
2. The XGBoost model demonstrated strong predictive performance across three critical batch-level parameters—Total Weight, Forging Count, and Total Length—with R^2 scores of 0.74, 0.88, and 0.87, respectively, validating its capability to generalize across diverse loading scenarios.
3. Feature importance and partial dependence analyses revealed that forging geometry (Shape) and Width were primary factors influencing batch configurations, reflecting technician priorities related to spatial constraints and material homogeneity. Process parameters like Temperature and Holding Duration showed limited impact on logistical decisions, consistent with their predefined nature.
4. The model identified non-linear decision patterns and interpretable thresholds—such as Width beyond ~30 cm and Length exceeding ~180 cm—which can guide planning for new or irregular forgings without relying solely on past experience.

This framework replicates feasible, experience-based loading strategies to enhance consistency and reduce planning uncertainty, particularly in handling new, irregular, or non-standard forgings. By supporting more consistent planning, it also mitigates risks associated with suboptimal configurations, such as QC rejections or increased energy consumption from inefficient cycles or reprocessing.

Future work will explore integrating physical constraints and experimental validation to align batch planning with thermal uniformity objectives. Additionally, deployment pathways include adapting the model for real-time decision support, and enabling dynamic updates as new production data becomes available. This adaptability could support continuous improvement in furnace operations while preserving alignment with established technician practices. The model could also be embedded as a practical software tool within industrial planning workflows, offering accessible, data-driven assistance for daily loading decisions.

CRediT authorship contribution statement

Sajad Mirzaei: Conceptualization, Methodology, Software, Validation, Visualization, Formal analysis, Investigation, Data curation, Writing—original draft preparation, Writing—review and editing. **Jean-Benoit Morin:** Resources, Writing – review & editing. **Mohammad Jahazi:** Supervision, Conceptualization, Resources, Formal analysis, Writing – review & editing, Project administration, Funding acquisition.

Funding

This work was funded by the Mitacs in the framework of [IT27097] Grants.

Acknowledgments

The authors wish to express their gratitude to Finkl Steel, particularly the Research and Development and Heat Treatment departments, for documenting information on the tempering process in electric furnaces over nine months, as well as for providing access to supplementary information. The authors also gratefully acknowledge Professor Russell Steele from the Department of Mathematics and Statistics at McGill University for his valuable assistance.

Declaration of competing interest

The authors declare that they have no known competing financial interests or personal relationships that could have appeared to influence the work reported in this paper.

CONCLUSION

Overall Contribution and Originality

This doctoral research presents the first integrated, experimentally validated framework for optimizing the design and operation of industrial-scale electrical tempering furnaces, combining CFD simulations, evolutionary multi-objective optimization, and data-driven machine learning approaches. The study encompasses three technically interlinked stages—each addressing distinct gaps in existing practice and knowledge:

- Stage I investigated the influence of stacking geometry (spacer and skid design) on thermal uniformity, supported by real-scale experimental validation using five embedded thermocouples across massive blocks up to 29 metric tons.
- Stage II focused on optimizing furnace heating element layout using a surrogate-assisted Genetic Algorithm and Pareto Search, marking the first application of such a strategy on a 112 m^3 electric furnace.
- Stage III introduced a practical ML model trained on 1,162 industrial production logs, enabling fast multi-target predictions to support batch-level loading decisions.

Together, these stages enabled the creation of a digital decision-support framework that not only enhances thermal uniformity and operational scheduling, but also strengthens the mechanistic understanding of transient heat transfer behavior in large-scale forgings.

Summary of Stage-Specific

1. Thermal Effects of Spacer and Skid Configurations
    - A validated 3D CFD model replicated the temperature evolution of stacked blocks with a deviation of ≤6.6% compared to measured thermocouple data.
    - Peak temperature non-uniformities of up to 373 K were observed in baseline configurations. The use of suitable spacers reduced these gradients by an average of 34%, while double-size skids improved uniformity by up to 36%, depending on block geometry.

- These results provide quantified guidelines for selecting spacer and skid configurations—previously determined only by technician experience.

2. Optimizing Heating Element Layout
   - Using GA and PS algorithms with polynomial surrogates, the optimal side-wall coverage was found to range between 10% and 14.2%, in contrast to the traditional 70% coverage.
   - The optimized layouts resulted in:
     - Up to 7.8% reduction in surface temperature non-uniformity.
     - 5.9% lower surface-to-center differentials.
     - Over 66% improvement in center-to-center thermal consistency between blocks.
   - This work delivers a novel quantitative mapping between wall coverage percentages and thermal metrics, grounded in both physics and numerical exploration.

3. Loading Cycle Prediction via Machine Learning
   - A multi-output XGBoost Regressor was developed to predict the Total Weight, Forging Count, and Total Length of batches based on process and geometry features.
   - The model achieved R^2 values between 0.78 and 0.89, showing reliable predictive accuracy, and identified shape type and width as dominant features influencing technician decisions.
   - This represents the first AI-driven tool specifically trained on real production logs for furnace loading recommendations in industrial steel tempering.

Final Conclusion Statement

This thesis presents a new knowledge chain that contributes to better planning, design, and operation of large-scale tempering furnaces from empirically-driven routines into a validated, quantitative methodology. The research introduces:

- Verified heat transfer models tailored and calibrated to real furnace geometries and loadings.

- Optimized design principles for both block stacking and heating element layouts.
- A fast and interpretable ML model to support day-to-day scheduling decisions.

By bridging detailed simulation with practical scheduling tools, this work offers a scientifically grounded and operationally useful framework for improving thermal uniformity, process consistency, and decision-making speed in the industrial steel heat treatment sector.

RECOMMENDATIONS

Recommendations for Industrial Implementation

1. Adoption of Validated CFD Models in Routine Engineering

Industries can incorporate the validated CFD framework into design and troubleshooting tasks for tempering processes. Regular updates of model inputs (e.g., furnace geometry, heat losses, and fan speeds) using operational data are recommended to maintain predictive accuracy.

2. Standardizing Spacer and Skid Selection

The demonstrated impact of spacer height and skid geometry on temperature uniformity supports the development of standard selection guidelines. Plants are encouraged to base configuration choices on simulation-informed rules rather than empirical routines.

3. Optimizing Heating Element Layout

While full redesign may be cost-prohibitive, partial implementation of the optimized heating layout—such as zoning of wall segments or selective rewiring—can improve surface and internal uniformities. For new furnace projects, applying surrogate-assisted multi-objective optimization in the design phase can guide effective coverage allocation from the outset.

4. Integrating Machine Learning in Scheduling

The XGBoost-based model developed here enables rapid forecasting of batch-level parameters and can assist planners during shift-level operations. Embedding this tool within a dashboard or production planning system would allow users to input basic forging details and receive guidance on batch feasibility. Regular retraining with newly logged data ensures that predictions remain accurate over time.

5. Continuous Monitoring and Data Infrastructure

The success of both CFD and ML frameworks depends on high-quality, consistently labeled datasets. Industrial partners are encouraged to standardize data collection protocols for forging

dimensions, load positions, furnace conditions, and microstructural outcomes. Linking these datasets over time enables more advanced analyses and lays the groundwork for predictive digital twin implementations.

Suggestions for Future Research

1. Linking Thermal Fields to Metallurgical Outcomes

The next logical extension is to couple temperature predictions with microstructural evolution modeling. This can be achieved using transformation kinetics or thermophysical simulation tools such as Thermo-Calc and its DICTRA module, enabling the prediction of hardness profiles, residual stresses, or phase distribution, bringing material behavior directly into optimization loops.

2. Real-Time and Adaptive Optimization

The current optimization strategy is offline. Future research could explore real-time or in-process optimization, reacting to disturbances such as load changes or heating anomalies. Integration with SCADA systems and the use of HPC/cloud resources can make dynamic re-optimization feasible in production settings.

3. Advancing Machine Learning Models

While XGBoost performed well, deep learning architectures (e.g., MLPs or GNNs) may improve performance with richer data. Physics-informed learning could further constrain outputs, enhancing reliability and interpretability without sacrificing model flexibility.

4. Adapting Methodology to Other Furnace Types

The approach developed here can be generalized to other heat treatment systems such as gas-fired, induction, or hybrid furnaces. These environments introduce new physics (e.g., gas composition, electromagnetic fields), but the same CFD–optimization–ML framework can be extended with appropriate modeling.

5. Multi-Site Trials and Broader Deployment

To confirm generalizability, pilot-scale trials in other plants—with different furnace sizes, block geometries, or product mixes—are recommended. These can validate transferability, expose practical deployment barriers, and help build the business case for digital integration in steel heat treatment operations.

LIST OF REFERENCES

Adhikary, A. (2021). Predicting Mechanical Properties of Low-Alloy Steels using Machine Learning. *International Journal of Advances in Engineering and Management, 3*(8), 660-670.

Amanlou, Y., & Khoshtaghaza, M. H. (2018). Applications of CFD for Optimization of Cabinet Dryers. In *Computational Fluid Dynamics in Food Processing* (2nd ed., pp. 415-436): CRC Press.

Angelopoulos, P. M., Peppas, A., & Taxiarchou, M. (2024). Modelling the Thermal Treatment and Expansion of Mineral Microspheres (Perlite) in Electric Furnace Through Computational Fluid Dynamics (CFD): Effect of Process Conditions and Feed Characteristics. *Mineral Processing and Extractive Metallurgy Review, 45*(4), 314-331. doi:10.1080/08827508.2022.2161536

ANSYS Inc. (2020). *ANSYS Fluent Mosaic Technology Automatically Combines Disparate Meshes with Polyhedral Elements for Fast, Accurate Flow Resolution.* Retrieved from Southpointe, 2600 Ansys Drive, Canonsburg, PA 15317, USA: http://www.ansys.com

ANSYS Inc. (2023). *ANSYS Fluent Theory Guide* (2023 R2 ed.). Southpointe, 2600 Ansys Drive, Canonsburg, PA 15317, USA: ANSYS, Inc.

Arkhazloo, N. B., Bazdidi-Tehrani, F., Jadidi, M., Morin, J.-B., & Jahazi, M. (2021). Determination of Temperature Distribution during Heat Treatment of Forgings: Simulation and Experiment. *Heat Transfer Engineering, 43*(12), 1041-1064. doi:10.1080/01457632.2021.1932039

Arkhazloo, N. B., Bouissa, Y., Bazdidi-Tehrani, F., Jadidi, M., Morin, J. B., & Jahazi, M. (2019). Experimental and unsteady CFD analyses of the heating process of large size forgings in a gas-fired furnace. *Case Studies in Thermal Engineering, 14*, 100428. doi:10.1016/j.csite.2019.100428

Arocena, V. M., & Danao, L. A. M. (2023). Improving the Modeling of Pressure Pulsation and Cavitation Prediction in a Double-Volute Double-Suction Pump Using Mosaic Meshing Technology. *Processes, 11*(3), 660. doi:10.3390/pr11030660

Arroyo, J., Pérez, L., & Cuervo-Piñera, V. (2023). CFD Modeling and Validation of Blast Furnace Gas/Natural Gas Mixture Combustion in an Experimental Industrial Furnace. *Processes, 11*(2), 332. doi:10.3390/pr11020332

Asgarkhani, N., Kazemi, F., Jakubczyk-Gałczyńska, A., Mohebi, B., & Jankowski, R. (2024). Seismic response and performance prediction of steel buckling-restrained braced frames using machine-learning methods. *Engineering Applications of Artificial Intelligence, 128*, 107388. doi:10.1016/j.engappai.2023.107388

Askeland, D. R., Phulé, P. P., Wright, W. J., & Bhattacharya, D. (2003). *The science and engineering of materials* (1 ed.): Springer Dordrecht.

Automation, I. S. o. (1982). Temperature Measurement Thermocouples. In (Vol. ANSI/ISA MC96.1-1982). Research Triangle Park, North Carolina: ISA.

Baukal Jr, C. E. (2004). *Industrial burners handbook*. Boca Raton, FL: CRC Press.

Bergmann, O., Götten, F., Braun, C., & Janser, F. (2022). Comparison and evaluation of blade element methods against RANS simulations and test data. *CEAS Aeronautical Journal, 13*(2), 535-557. doi:10.1007/s13272-022-00579-1

Bhadeshia, H. K. D. H., & Honeycombe, R. W. K. (2017). *Steels: microstructure and properties* (4 ed.). Oxford, UK: Butterworth-Heinemann.

Bishop, C. M., & Nasrabadi, N. M. (2006). *Pattern recognition and machine learning* (Vol. 4). New York: Springer.

Bohlooli Arkhazloo, N. (2020). *Optimization of furnace residence time and ingots positioning during the heat treatment process of large size forged ingots.* (Doctoral dissertation Doctoral dissertation). École de technologie supérieure, Montreal, Canada.

Bohlooli Arkhazloo, N., Bazdidi-Tehrani, F., Morin, J.-B., & Jahazi, M. (2021). Optimization of furnace residence time and loading pattern during heat treatment of large size forgings. *The International Journal of Advanced Manufacturing Technology, 113*(9-10), 2447-2460. doi:10.1007/s00170-021-06807-y

Bouissa, Y., Bohlooli, N., Shahriari, D., Champliaud, H., Morin, J. B., & Jahazi, M. (2020). FEM modeling and experimental validation of quench-induced distortions of large size steel forgings. *Journal of Manufacturing Processes, 58*, 592-605. doi:10.1016/j.jmapro.2020.08.042

Brooks, C. R. (1996). *Principles of the heat treatment of plain carbon and low alloy steels*. Materials Park, OH: ASM international.

Brownlee, J. (2020). *Data preparation for machine learning: data cleaning, feature selection, and data transforms in Python*. San Jose, CA: Machine Learning Mastery.

Canale, L. C. F., Yao, X., Gu, J., & Totten, G. E. (2008). A historical overview of steel tempering parameters. *International Journal of Microstructure and Materials Properties, 3*(4/5). doi:10.1504/ijmmp.2008.022033

Carlsson, L. (2021). *Applied Machine Learning in Steel Process Engineering: Using supervised machine learning models to predict the electrical energy consumption of electric arc furnaces.* (Doctoral thesis Doctoral Thesis). KTH Royal Institute of Technology, Stockholm, Sweden.

Chan, D. Y. L., Yang, K. H., Lee, J. D., & Hong, G. B. (2010). The case study of furnace use and energy conservation in iron and steel industry. *Energy, 35*(4), 1665-1670. doi:10.1016/j.energy.2009.12.014

Chapman, C. D., Saitou, K., & Jakiela, M. J. (1994). Genetic Algorithms as an Approach to Configuration and Topology Design. *Journal of Mechanical Design, 116*(4), 1005-1012. doi:Doi 10.1115/1.2919480

Charles, M., Deskevich, N., Varkey, V., Voigt, R., & Wollenburg, A. (2004). *Heat Treatment Procedure Qualification for Steel Castings*. Retrieved from University Park, PA:

Chattopadhyay, K., Isac, M., & Guthrie, R. I. L. (2010). Applications of Computational Fluid Dynamics (CFD) in iron- and steelmaking: Part 1. *Ironmaking & Steelmaking, 37*(8), 554-561. doi:10.1179/030192310x12731438631804

Chen, C., Wang, N., Chen, M., & Yan, X. M. (2022). A framework based on heterogeneous ensemble models for liquid steel temperature prediction in LF refining process. *Applied Soft Computing, 131*, 109724. doi:10.1016/j.asoc.2022.109724

Chen, J. X., Zhao, F., Sun, Y. G., Zhang, L., & Yin, Y. L. (2019). Prediction model based on XGBoost for mechanical properties of steel materials. *International Journal of Modelling Identification and Control, 33*(4), 322-330. doi:10.1504/Ijmic.2019.107482

Chen, T., & Guestrin, C. (2016). *Xgboost: A scalable tree boosting system.* Paper presented at the Proceedings of the 22nd ACM SIGKDD international conference on knowledge discovery and data mining.

Chicco, D., Warrens, M. J., & Jurman, G. (2021). The coefficient of determination R-squared is more informative than SMAPE, MAE, MAPE, MSE and RMSE in regression analysis evaluation. *PeerJ Comput Sci, 7*, e623. doi:10.7717/peerj-cs.623

Choi, D. K. (2019). Data-Driven Materials Modeling with XGBoost Algorithm and Statistical Inference Analysis for Prediction of Fatigue Strength of Steels. *International Journal of Precision Engineering and Manufacturing, 20*(1), 129-138. doi:10.1007/s12541-019-00048-6

Colin R. Reeves , J. E. R. (2002). *Genetic algorithms: principles and perspectives: a guide to GA theory* (1 ed. Vol. 20): Springer New York, NY.

Committee, A. H. (1991). *ASM handbook, volume 4: Heat treating* (Vol. 4). Materials Park, OH: ASM international.

Coskun, G., Sarikaya, C., Buyukkaya, E., & Kucuk, H. (2023). Optimization of the Injectors Position for an Electric Arc Furnace by using CFD Simulation. *Journal of Applied Fluid Mechanics, 16*(2), 233-243. doi:10.47176/jafm.16.02.1352

Cresko, J., Thekdi, A., Nimbalkar, S., Thirumaran, K., Hasanbeigi, A., & Chaudhari, S. (2022). *Thermal Process Intensification: Transforming the Way Industry Uses Thermal Process Energy* (1867992). Retrieved from

Cui, C., Cao, G., Li, X., Gao, Z., Liu, J., & Liu, Z. (2023). A strategy combining machine learning and physical metallurgical principles to predict mechanical properties for hot rolled Ti micro-alloyed steels. *Journal of materials processing technology, 311*, 117810. doi:10.1016/j.jmatprotec.2022.117810

Deb, K. (2011). Multi-objective optimisation using evolutionary algorithms: an introduction. In *Multi-objective evolutionary optimisation for product design and manufacturing* (pp. 3-34). London: Springer.

Díaz-Ovalle, C. O., Martínez-Zamora, R., González-Alatorre, G., Rosales-Marines, L., & Lesso-Arroyo, R. (2017). An approach to reduce the pre-heating time in a convection oven via CFD simulation. *Food and bioproducts processing, 102*, 98-106. doi:10.1016/j.fbp.2016.12.009

Digital Research Alliance of Canada. (2025). Technical Documentation. February 11, 2025. Retrieved from https://docs.alliancecan.ca/wiki/Technical_documentation

Dogruoz, M. B., & Shankaran, G. (2017). Computations with the multiple reference frame technique: Flow and temperature fields downstream of an axial fan. *Numerical Heat Transfer Part a-Applications, 71*(5), 488-510. doi:10.1080/10407782.2016.1277930

Dossett, J. L., & Totten, G. E. (2013). *Steel heat treating fundamentals and processes* (Vol. 4A). Materials Park, OH: Asm International.

Engineering, O. (2022, July 8, 2024). Thermocouple types. Retrieved from https://www.omega.ca/en/resources/thermocouple-types

Ferziger, J. H., Perić, M., & Street, R. L. (2019). *Computational methods for fluid dynamics* (4 ed.): Springer.

Filipponi, M., Rossi, F., Presciutti, A., De Ciantis, S., Castellani, B., & Carpinelli, A. (2016). Thermal Analysis of an Industrial Furnace. *Energies, 9*(10), 833. doi:10.3390/en9100833

Finkl Steel Inc. (2021). Sorel Forge. Retrieved from http://www.sorelforge.com/

Fleischer, M. (2003). *The measure of Pareto optima applications to multi-objective metaheuristics*. Paper presented at the Second International Conference on Evolutionary Multi-Criterion Optimization, Portugal.

Frank Kreith, M. S. B., Raj M. Manglik. (2010). *Principles of heat transfer* (7 ed.). United States: Course Technology.

Fu, Z. L., Yu, X. H., Shang, H. L., Wang, Z. Z., & Zhang, Z. Y. (2019). A new modelling method for superalloy heating in resistance furnace using FLUENT. *International Journal of Heat and Mass Transfer, 128*, 679-687. doi:10.1016/j.ijheatmasstransfer.2018.08.105

Galletti, C., Coraggio, G., & Tognotti, L. (2013). Numerical investigation of oxy-natural-gas combustion in a semi-industrial furnace: Validation of CFD sub-models. *Fuel, 109*, 445-460. doi:10.1016/j.fuel.2013.02.061

Gao, M., Reid, C. N., Jahedi, M., & Li, Y. (2000). Estimating equilibration times and heating/cooling rates in heat treatment of workpieces with arbitrary geometry. *Journal of Materials Engineering and Performance, 9*(1), 62-71. doi:10.1361/105994900770346295

Go, Y. J., Bae, J. H., Ryi, J., Choi, J. S., & Lee, C. R. (2022). A Study on the Scale Effect According to the Reynolds Number in Propeller Flow Analysis and a Model Experiment. *Aerospace, 9*(10), 559. doi:10.3390/aerospace9100559

Golmohammadi, M., & Aryanpour, M. (2023). Analysis and evaluation of machine learning applications in materials design and discovery. *Materials Today Communications, 35*, 105494. doi:10.1016/j.mtcomm.2023.105494

Govardhan, J., Rao, G., & Narasaiah, J. (2011). Experimental investigations and CFD study of temperature distribution during oscillating combustion in a crucible furnace. *International Journal of Energy and Environment, 2*(5), 783-796.

Gur, C. H., & Pan, J. (2008). *Handbook of thermal process modeling steels* (1 ed.). Boca Raton: CRC Press.

Hadała, B., Malinowski, Z., & Rywotycki, M. (2017). Energy losses from the furnace chamber walls during heating and heat treatment of heavy forgings. *Energy, 139*, 298-314. doi:10.1016/j.energy.2017.07.121

Halin, F. (2024). Megawatts refusés: Plus de 320 emplois de 80 000 à 120 000$ menacés aux Forges de Sorel. *Le Journal de Montréal*. Retrieved from https://www.journaldemontreal.com/2024/09/17/megawatts-refuses-plus-de-320-emplois-de-80-000-a-120-000-menaces-aux-forges-de-sorel

Harish, J., & Dutta, P. (2005). Heat transfer analysis of pusher type reheat furnace. *Ironmaking & Steelmaking, 32*(2), 151-158. doi:10.1179/174328105x23923

Hastie, T., Tibshirani, R., Friedman, J. H., & Friedman, J. H. (2009). *The elements of statistical learning: data mining, inference, and prediction* (Vol. 2). New York: Springer.

He, L. J., Ishibuchi, H., Trivedi, A., Wang, H. D., Nan, Y., & Srinivasan, D. (2021). A Survey of Normalization Methods in Multiobjective Evolutionary Algorithms. *IEEE*

Transactions on Evolutionary Computation, 25(6), 1028-1048. doi:10.1109/Tevc.2021.3076514

Howell, J. R., Mengüç, M. P., Daun, K., & Siegel, R. (2020). *Thermal radiation heat transfer*: CRC press.

Incropera, F. P., DeWitt, D. P., Bergman, T. L., & Lavine, A. S. (1996). *Fundamentals of heat and mass transfer* (Vol. 6): Wiley New York.

International Energy Agency. (2024). *World Energy Outlook 2024*. Retrieved from Paris, France: https://www.iea.org/reports/world-energy-outlook-2024

Ismail, O. S., Awonusi, A. A., & Akinoso, R. (2021). Isothermal Air Flow Investigation in Industrial Baking Oven of Different Impeller Locations using Computational Fluid Dynamics (CFD) Approach. *Journal of Engineering Science, 17*(2), 73-91.

Jamaluddin, A. S., & Smith, P. J. (1988). Predicting Radiative-Transfer in Rectangular Enclosures Using the Discrete Ordinates Method. *Combustion Science and Technology, 59*(4-6), 321-340. doi:10.1080/00102208808947103

James, G., Witten, D., Hastie, T., & Tibshirani, R. (2013). *An introduction to statistical learning* (Vol. 112): Springer.

Ji, W. C., Li, G. J., Wei, L. Y., & Yi, Z. (2021). Modeling and determination of total heat exchange factor of regenerative reheating furnace based on instrumented slab trials. *Case Studies in Thermal Engineering, 24*, 100838. doi:10.1016/j.csite.2021.100838

Ji, Y., Wang, W. L., Zhou, L. J., Zhong, X. C., & Si, X. Z. (2024). Prediction and Feature Analysis of Entrapped Slag Defect on Casting Slab Based on Optimized XGBoost Model. *Metallurgical and Materials Transactions B-Process Metallurgy and Materials Processing Science, 55*(4), 2026-2036. doi:10.1007/s11663-024-03092-4

K, K., Krishnan, S., & Manikandan, R. (2024). Water quality prediction: a data-driven approach exploiting advanced machine learning algorithms with data augmentation. *Journal of Water and Climate Change, 15*(2), 431-452. doi:10.2166/wcc.2023.403

Kang, J. W., & Rong, Y. M. (2006). Modeling and simulation of load heating in heat treatment furnaces. *Journal of materials processing technology, 174*(1-3), 109-114. doi:10.1016/j.jmatprotec.2005.03.037

Kanthal. (1999). *Kanthal super–Electric Heating Element Handbook*: Sweden.

Kanthal. (2001). Resistance Heating Alloys and Systems for Industrial Furnaces. In K. AB (Ed.). Sweden: Kanthal AB.

Kaymak, Y. (2007). *Simulation of metal quenching processes for the minimization of distortion and stresses*. (Doktoringenieur (Dr.-Ing.) Doctoral dissertation). Otto von Guericke Universität Magdeburg, Magdeburg.

Kim, S., Choi, J., & Ryu, K. R. (2022). Optimization of Heat Treatment Scheduling for Hot Press Forging Using Data-Driven Models. *Intelligent Automation and Soft Computing, 32*(1), 207-220. doi:10.32604/iasc.2022.021752

Kislinger, C., Daurer, G., Schwarz, S., Demuth, M., Gaber, C., & Hochenauer, C. (2025). CFD study of hydrogen combustion effects on the heat-up characteristics of steel samples using a low-swirl burner: A comparative analysis with methane. *Applied Thermal Engineering, 261*, 125105. doi:10.1016/j.applthermaleng.2024.125105

Kluczek, A., & Olszewski, P. (2017). Energy audits in industrial processes. *Journal of cleaner production, 142*, 3437-3453. doi:10.1016/j.jclepro.2016.10.123

Korad, T., Ponboon, M., Chumchery, N., & Pearce, J. T. H. (2013). Overview of Flow Analysis Simulation in Improving Heat Treatment Conditions. *Chiang Mai Journal of Science, 40*(5), 898-908. Retrieved from <Go to ISI>://WOS:000327718600012

Kuhn, M., & Johnson, K. (2013). *Applied predictive modeling* (Vol. 26): Springer.

Lai, D. D., Demartino, C., & Xiao, Y. (2024). Probabilistic machine leaning models for predicting the maximum displacements of concrete-filled steel tubular columns subjected to lateral impact loading. *Engineering Applications of Artificial Intelligence, 135*, 108704. doi:10.1016/j.engappai.2024.108704

Lavadera, M. L., Kamal, M. M., Sharma, S., Donato, L., Galletti, C., Coussement, A., & Parente, A. (2024). A combined experimental, numerical, and data consistency approach for the characterization of temperature distribution in a MILD combustion furnace. *Applied Thermal Engineering, 243*, 122625. doi:10.1016/j.applthermaleng.2024.122625

Li, M., Guiqin, L., Xihang, L., Lixin, L., & Mitrouchev, P. (2024). Prediction of Mechanical Properties of Hot-Rolled Strip Steel Based on XGBoost and Metallurgical Mechanism. *Physics of Metals and Metallography, 125*(13), 1728-1738. doi:10.1134/s0031918x23600653

Lim, S., & Chi, S. (2019). Xgboost application on bridge management systems for proactive damage estimation. *Advanced Engineering Informatics, 41*, 100922. doi:10.1016/j.aei.2019.100922

Liščić, B., & Filetin, T. (1987). Computer-aided determination of the process parameters for hardening and tempering structural steels. *International heat treatment and surface engineering, 3*, 62-66.

Liu, H. (2024). A study on the influence of the spread of Yangming Studies in Japan on the psychology of the Japanese people based on big data analysis. *Applied Mathematics and Nonlinear Sciences, 9*(1).

Liu, Y.-x., Dong, Y.-w., Jiang, Z.-h., Li, Y.-s., Zha, W., Du, Y.-x., & Du, S.-y. (2023). XGBoost-based model for predicting hydrogen content in electroslag remelting. *Journal of Iron and Steel Research International, 30*(5), 887-896.

Liu, Y. J., Li, J. D., Misra, R. D. K., Wang, Z. D., & Wang, G. D. (2016). A numerical analysis of slab heating characteristics in a rolling type reheating furnace with pulse combustion. *Applied Thermal Engineering, 107*, 1304-1312. doi:10.1016/j.applthermaleng.2016.07.074

Macchion, O., Zahrai, S., & Bouwman, J. W. (2006). Heat transfer from typical loads within gas quenching furnace. *Journal of materials processing technology, 172*(3), 356-362. doi:10.1016/j.jmatprotec.2005.10.017

Mamun, O., Wenzlick, M., Sathanur, A., Hawk, J., & Devanathan, R. (2021). Machine learning augmented predictive and generative model for rupture life in ferritic and austenitic steels. *Npj Materials Degradation, 5*(1), 20. doi:10.1038/s41529-021-00166-5

Manojlović, V., Kamberović, Ž., Korać, M., & Dotlić, M. (2022). Machine learning analysis of electric arc furnace process for the evaluation of energy efficiency parameters. *Applied Energy, 307*, 118209. doi:10.1016/j.apenergy.2021.118209

MathWorks. (2021). R2021b [Computer software]. Natick, MA: MathWorks. Retrieved from https://www.mathworks.com/products/matlab.html

Mayr, B., Prieler, R., Demuth, M., Moderer, L., & Hochenauer, C. (2017). CFD analysis of a pusher type reheating furnace and the billet heating characteristic. *Applied Thermal Engineering, 115*, 986-994. doi:10.1016/j.applthermaleng.2017.01.028

Mirzaei, S., Arkhazloo, N. B., Bazdidi-Tehrani, F., Morin, J. B., Loucif, A., & Jahazi, M. (2023). Influence of Spacers and Skid Sizes on Heat Treatment of Large Forgings within an Industrial Electric Furnace. *Energies, 16*(7), 2936. doi:10.3390/en16072936

Mirzaei, S., Arkhazloo, N. B., Morin, J. B., & Jahazi, M. (2024). Influence of heating elements layout on temperature uniformity in a large size heat treatment furnace. *Case Studies in Thermal Engineering, 61*, 105062. doi:10.1016/j.csite.2024.105062

Mullinger, P., & Jenkins, B. (2022). *Industrial and process furnaces: principles, design and operation* (3 ed.): Butterworth-Heinemann.

Nakhaei, M., Lu, B. N., Tian, Y. J., Wang, W., Dam-Johansen, K., & Wu, H. (2020). CFD Modeling of Gas-Solid Cyclone Separators at Ambient and Elevated Temperatures. *Processes, 8*(2), 228. doi:10.3390/pr8020228

Nguyen, H. D., Dao, N. D., & Shin, M. (2021). Prediction of seismic drift responses of planar steel moment frames using artificial neural network and extreme gradient boosting. *Engineering Structures, 242*, 112518. doi:10.1016/j.engstruct.2021.112518

Nwakuya, M. T., & Nkwocha, C. C. (2022). Manly transformation in quantile regression: A comparison of two transformation parameter estimators. *Scientia Africana, 21*(1), 67-76. doi:10.4314/sa.v21i1.6

Ostertagová, E. (2012). Modelling using polynomial regression. *Modelling of Mechanical and Mechatronics Systems, 48*, 500-506. doi:10.1016/j.proeng.2012.09.545

Palacio-Caro, I. D., Alvarado-Torres, P. N., & Cardona-Sepúlveda, L. F. (2020). Numerical Simulation of the Flow and Heat Transfer in an Electric Steel Tempering Furnace. *Energies, 13*(14), 3655. doi:10.3390/en13143655

Paloposki, T., & Liedquist, L. (2005). *Steel emissivity at high temperatures*. Espoo: VTT Technical Research Centre of Finland.

Pan, X., & Montreuil, B. (2021). *Assessing Multi-Purpose Forecasting Accuracy.* Paper presented at the IIE Annual Conference. Proceedings.

Park, S., & Youm, S. (2023). Establish a machine learning based model for optimal casting conditions management of small and medium sized die casting manufacturers. *Scientific Reports, 13*(1), 17163. doi:10.1038/s41598-023-44449-0

Pedregosa, F., Varoquaux, G., Gramfort, A., Michel, V., Thirion, B., Grisel, O., . . . Duchesnay, E. (2011). Scikit-learn: Machine Learning in Python. *Journal of Machine Learning Research, 12*, 2825-2830. Retrieved from <Go to ISI>://WOS:000298103200003

Pei, Y., Yu, A., Qin, J., Yi, R., Yu, X., Liu, S., . . . Hou, X. (2022). Dynamic algorithm for fitness function greatly improves the optimization efficiency of frequency selective surface for better design of radar. *Scientific Reports, 12*(1), 16596. doi:10.1038/s41598-022-20167-x

Pfeifer, H. (2017). Industrial Furnaces - Status and Research Challenges. *Infub - 11th European Conference on Industrial Furnaces and Boilers (Infub-11), 120*, 28-40. doi:10.1016/j.egypro.2017.07.153

Pineau, P.-O. (2025). Decarbonization and Electrification in the Northeast: The Climate Crisis Will Foster a New Québec-United States Relationship in Electricity. In *The Québec-United States Relationship: Political, Security, Economic, Environmental and Cultural Dynamics* (pp. 285-307): Springer.

Piyapaneekoon, A., & Kowitwarangkul, P. (2020). *A CFD study on the energy saving in reheating furnace with oxygen-enriched air conditions.* Paper presented at the AIP Conference Proceedings.

Prieler, R., Mayr, B., Demuth, M., Spoljaric, D., & Hochenauer, C. (2015). Application of the steady flamelet model on a lab-scale and an industrial furnace for different oxygen concentrations. *Energy, 91*, 451-464. doi:10.1016/j.energy.2015.08.070

Qiu, L., Li, Y. L., Feng, Y. H., Chen, Z. G., & Zhang, X. X. (2019). Three-dimensional fluid-solid coupling heat transfer simulation based on the multireference frame for a side-blown aluminum annealing furnace. *Engineering Applications of Computational Fluid Mechanics, 13*(1), 1036-1048. doi:10.1080/19942060.2019.1666427

Rabiee, A., Ahmadian-Elmi, M., Hajmohammadi, M. R., & Mohammadifar, M. (2023). Multi-objective optimization of rectangular microchannel heat sink based on entropy generation and hydro-thermal performance using NSGA-II algorithm. *International Communications in Heat and Mass Transfer, 149*, 107140. doi:10.1016/j.icheatmasstransfer.2023.107140

Rakhit, A. (2000). *Heat Treatment of Gears: A Practical Guide for Engineers*: ASM international.

Riani, M., Atkinson, A. C., & Corbellini, A. (2022). Automatic robust Box–Cox and extended Yeo–Johnson transformations in regression. *Statistical Methods & Applications, 32*(1), 75-102. doi:10.1007/s10260-022-00640-7

S.N. Sivanandam, S. N. D. (2007). *Introduction to Genetic Algorithms* (1 ed.). Germany: Springer Berlin, Heidelberg.

Schmid, L., Gerharz, A., Groll, A., & Pauly, M. (2022). *Machine Learning for Multi-Output Regression: When should a holistic multivariate approach be preferred over separate univariate ones?* (arXiv:2201.05340). Retrieved from

SenteSoftware. JMatPro users guide (Version 6.2.1). Guildford, United Kingdom: Sente Software Ltd. Retrieved from https://www.sentesoftware.co.uk/jmatpro

Shafighfard, T., Kazemi, F., Asgarkhani, N., & Yoo, D.-Y. (2024). Machine-learning methods for estimating compressive strength of high-performance alkali-activated concrete. *Engineering Applications of Artificial Intelligence, 136*, 109053.

Shih, T.-H., Liou, W. W., Shabbir, A., Yang, Z., & Zhu, J. (1995). A new k-ϵ eddy viscosity model for high reynolds number turbulent flows. *Computers & fluids, 24*(3), 227-238. doi:10.1016/0045-7930(94)00032-t

Singh, V. K., Talukdar, P., & Coelho, P. J. (2015). Performance Evaluation of Two Heat Transfer Models of a Walking Beam Type Reheat Furnace. *Heat Transfer Engineering, 36*(1), 91-101. doi:10.1080/01457632.2014.906287

Smolka, J., Nowak, A. J., & Rybarz, D. (2010). Improved 3-D temperature uniformity in a laboratory drying oven based on experimentally validated CFD computations. *Journal of Food Engineering, 97*(3), 373-383. doi:10.1016/j.jfoodeng.2009.10.032

Song, K., Yan, F., Ding, T., Gao, L., & Lu, S. B. (2020). A steel property optimization model based on the XGBoost algorithm and improved PSO. *Computational Materials Science, 174*, 109472. doi:10.1016/j.commatsci.2019.109472

Staggs, J. E. J., & Phylaktou, H. N. (2008). The effects of emissivity on the performance of steel in furnace tests. *Fire Safety Journal, 43*(1), 1-10. doi:10.1016/j.firesaf.2007.05.002

Takalo-Mattila, J., Heiskanen, M., Kyllonen, V., Maatta, L., & Bogdanoff, A. (2022). Explainable Steel Quality Prediction System Based on Gradient Boosting Decision Trees. *IEEE Access, 10*, 68099-68110. doi:10.1109/Access.2022.3185607

Tan, S. A., Yu, K. H., & Abdullah, M. Z. (2022). Heat transfer analysis on wafer annealing process in semiconductor multi-wafer furnace using CFD simulation. *Journal of Mechanical Science and Technology, 36*(6), 3143-3151. doi:10.1007/s12206-022-0545-4

Tang, G. W., Wu, B., Bai, D. Q., Wang, Y. F., Bodnar, R., & Zhou, C. (2018). CFD modeling and validation of a dynamic slab heating process in an industrial walking beam reheating furnace. *Applied Thermal Engineering, 132*, 779-789. doi:10.1016/j.applthermaleng.2018.01.017

Tang, G. W., Wu, B., Bai, D. Q., Wang, Y. F., Bodnar, R., & Zhou, C. Q. (2017). Modeling of the slab heating process in a walking beam reheating furnace for process optimization. *International Journal of Heat and Mass Transfer, 113*, 1142-1151. doi:10.1016/j.ijheatmasstransfer.2017.06.026

Totten, G. E. (2006). *Steel heat treatment: metallurgy and technologies*: CRC press.

U.S. Department of Energy. (2015). *Improving Process Heating System Performance: A Sourcebook for Industry*. Retrieved from Washington, DC, USA: https://www.energy.gov/

U.S. EIA. (2006). Steel Industry Analysis Brief. Retrieved from https://www.eia.gov/consumption/manufacturing/briefs/steel/

Umbarkar, A. J., & Sheth, P. D. (2015). Crossover Operators in Genetic Algorithms: A Review. *ICTACT journal on soft computing, 06*(01), 1083-1092. doi:10.21917/ijsc.2015.0150

Unifrax. (2017). *Product Information Sheet*. Retrieved from USA: https://www.unifrax.com/product/fiberfrax-durablanket-hp-s/

Van Doormaal, J. P., & Raithby, G. D. (2007). Enhancements of the Simple Method for Predicting Incompressible Fluid Flows. *Numerical heat transfer, 7*(2), 147-163. doi:10.1080/01495728408961817

Versteeg, H. K., & Malalasekera, W. (2007). *An introduction to computational fluid dynamics: the finite volume method* (2 ed.). Harlow, England: Pearson education.

Wade, C., & Glynn, K. (2020). *Hands-On Gradient Boosting with XGBoost and scikit-learn: Perform accessible machine learning and extreme gradient boosting with Python*: Packt Publishing Ltd.

Wang, D. J., Zhang, X. R., Zhu, Y. X., & Jiang, Z. Y. (2024). Analysis of billet temperature non-uniformity in a regenerative reheating furnace: Considering periodic combustion switching and misalignment contact of walking beams. *Case Studies in Thermal Engineering, 59*, 104573. doi:10.1016/j.csite.2024.104573

Wang, G. G., & Shan, S. (2006). *Review of Metamodeling Techniques in Support of Engineering Design Optimization*. Paper presented at the Volume 1: 32nd Design Automation Conference, Parts A and B.

Wang, G. H., & Li, Y. X. (2019). Effects of alloying elements and temperature on thermal conductivity of ferrite. *Journal of Applied Physics, 126*(12). doi:10.1063/1.5115441

Wang, Q. K., & Lu, H. F. (2024). A novel stacking ensemble learner for predicting residual strength of corroded pipelines. *Npj Materials Degradation, 8*(1), 87. doi:10.1038/s41529-024-00508-z

Wang, Q. L., Yao, G. W., Kong, G. Y., Wei, L., Yu, X. R., Zeng, J. C., . . . Luo, L. (2024). A data-driven model for predicting fatigue performance of high-strength steel wires based on optimized XGBOOST. *Engineering Failure Analysis, 164*, 108710. doi:10.1016/j.engfailanal.2024.108710

Wang, Z. H., Huang, Y., Liu, Y. M., & Wang, T. (2023). Prediction Model of Strip Crown in Hot Rolling Process Based on Machine Learning and Industrial Data. *Metals, 13*(5), 900. doi:10.3390/met13050900

Wang, Z. J., & Shang, X. F. (2010). Flow and Heat-transfer Simulation Based on CFD and Experimental Study during High-Pressure Gas Quenching. *Applied Mechanics and Mechanical Engineering, Pts 1-3, 29-32*, 1436-1440. doi:10.4028/www.scientific.net/AMM.29-32.1436

Wei, Y. Z., Ji, R. Q., Li, Q. F., & Song, Z. M. (2023). Mechanical Performance Prediction Model of Steel Bridge Deck Pavement System Based on XGBoost. *Applied Sciences-Basel, 13*(21), 12048. doi:10.3390/app132112048

Wilcox, D. (1998). *Turbulence Modeling for CFD* (2 ed.). Canada.

Xu, Z. X., Su, X. L., Xu, Q. Y., & Liu, B. C. (2016). Numerical simulation on vacuum solution heat treatment and gas quenching process of a low rhenium-containing Ni-based single crystal turbine blade. *China Foundry, 13*(6), 402-413. doi:10.1007/s41230-016-6044-4

Yan, F., Song, K., Liu, Y., Chen, S. W., & Chen, J. Y. (2020). Predictions and mechanism analyses of the fatigue strength of steel based on machine learning. *Journal of materials science, 55*(31), 15334-15349. doi:10.1007/s10853-020-05091-7

Yang, Y. X., de Jong, R. A., & Reuter, M. A. (2007). CFD prediction for the performance of a heat treatment furnace. *Progress in Computational Fluid Dynamics, 7*(2-4), 209-218. doi:10.1504/Pcfd.2007.013013

Yeo, I.-K. J., R. A. (2000). A new family of power transformations to improve normality or symmetry. *Biometrika, 87*(4), 954-959. doi:10.1093/biomet/87.4.954

Zhang, S. F., Wen, L. Y., Bai, C. G., Chen, D. F., & Long, Z. J. (2009). Analyses on 3-D gas flow and heat transfer in ladle furnace lid. *Applied mathematical modelling, 33*(6), 2646-2662. doi:10.1016/j.apm.2008.08.003

Zhang, S. Y., Chen, W. G., Xu, J. J., & Xie, T. Y. (2024). Use of interpretable machine learning approaches for quantificationally understanding the performance of steel fiber-reinforced recycled aggregate concrete: From the perspective of compressive strength and splitting tensile strength. *Engineering Applications of Artificial Intelligence, 137*, 109170. doi:10.1016/j.engappai.2024.109170

Zhou, W.-F., Wang, J.-G., Deng, L.-F., Yao, Y., & Liu, J.-L. (2021). *Terminal Temperature Prediction of Molten Steel in VD Furnace based on XGBoost and LightGBM Algorithms*. Paper presented at the 2021 40th Chinese Control Conference (CCC).

Zhuo, Y. T., Hu, Z. J., & Shen, Y. S. (2021). CFD study of hydrogen injection through tuyeres into ironmaking blast furnaces. *Fuel, 302*, 120804. doi:10.1016/j.fuel.2021.120804

Zhuo, Y. T., & Shen, Y. S. (2023). Transient 3D CFD study of pulverised coal combustion and coke combustion in a blast furnace: Effect of blast conditions. *Fuel, 340*, 127468. doi:10.1016/j.fuel.2023.127468

Zippo, V., Robotti, E., Maestri, D., Fossati, P., Valenza, D., Maggi, S., . . . Marengo, E. (2025). Development of a Self-Updating System for the Prediction of Steel Mechanical Properties in a Steel Company by Machine Learning Procedures. *Technologies, 13*(2), 75. doi:10.3390/technologies13020075